Volume 68C
Number 2
April-June 1964

Engineering and Instrumentation

U.S. DEPARTMENT OF COMMERCE

SECTION C

JOURNAL OF RESEARCH
NATIONAL BUREAU OF STANDARDS

Journal of Research

of the

National Bureau of Standards

C. Engineering and Instrumentation

APRIL–JUNE • 1964

VOLUME • 68C

NUMBER • 2

Editor: Martin Greenspan

Associate Editors: G. F. Montgomery, Thomas N. Flynn

Publication dates:
Feb. 15, May 15, Aug. 15, Nov. 15, 1964

JOURNAL OF RESEARCH

The National Bureau of Standards Journal of Research reports research and development in the fields of activity shown at right. Also included from time to time are survey articles on topics closely related to the Bureau's scientific and technical program.

The Journal is published in four separate sections as follows:

A. Physics and Chemistry

Contains papers of interest primarily to scientists working in these fields. Issued six times a year. Annual subscription: domestic, $4.00; foreign, $4.75. Single copy, 70¢.

B. Mathematics and Mathematical Physics

Presents studies and compilations designed mainly for the mathematician and the theoretical physicist. Issued quarterly. Annual subscription: domestic, $2.25; foreign, $2.75. Single copy, 75¢.

C. Engineering and Instrumentation

Reports research and development results of interest chiefly to the engineer and the applied scientist. Issued quarterly. Annual subscription: domestic, $2.25; foreign, $2.75. Single copy, 75¢.

D. Radio Science (formerly Radio Propagation)

Published in cooperation with U.S. National Committee of URSI. Presents papers in radio propagation, communications, and radio science generally. Issued monthly. Annual subscription: domestic, $9.00; foreign, $11.50. Single copy, $1.00.

The National Bureau of Standards is a principal focal point in the Federal Government for assuring maximum application of the physical and engineering sciences to the advancement of technology in industry and commerce. Its responsibilities include development and maintenance of the national standards of measurement, and the provisons of means for making measurements consistent with those standards; determination of physical constants and properties of materials; development of methods for testing materials, mechanisms, and structures, and making such tests as may be necessary, particularly for government agencies; cooperation in the establishment of standard practices for incorporation in codes and specifications; advisory service to government agencies on scientific and technical problems; invention and development of devices to serve special needs of the Government; assistance to industry, business, and consumers in the development and acceptance of commercial standards and simplified trade practice recommendations; administration of programs in cooperation with United States business groups and standards organizations for the development of international standards of practice; and maintenance of a clearinghouse for the collection and dissemination of scientific, technical, and engineering information.

Institute for Basic Standards. Electricity. Metrology. Heat. Radiation Physics. Mechanics. Applied Mathematics. Atomic Physics. Physical Chemistry. Laboratory Astrophysics.* Radio Standards Laboratory: Radio Standards Physics; Radio Standards Engineering.** Office of Standard Reference Data.

Institute for Materials Research. Analytical Chemistry. Polymers. Metallurgy. Inorganic Materials. Reactor Radiations. Cryogenics.** Office of Standard Reference Materials.

Central Radio Propagation Laboratory.** Ionosphere Research and Propagation. Troposphere and Space Telecommunications. Radio Systems. Upper Atmosphere and Space Physics.

Institute for Applied Technology. Textiles and Apparel Technology Center. Building Research. Industrial Equipment. Information Technology. Performance Test Development. Instrumentation. Transport Systems. Office of Technical Services. Office of Weights and Measures. Office of Engineering Standards. Office of Industrial Services.

*NBS Group, Joint Institute for Laboratory Astrophysics at the University of Colorado.
**Located at Boulder, Colo.

U.S. DEPARTMENT OF COMMERCE
Luther H. Hodges, Secretary
NATIONAL BUREAU OF STANDARDS
A. V. Astin, Director

Order all publications from the Superintendent of Documents
U.S. Government Printing Office, Washington, D.C., 20402.

Use of funds for printing this publication approved by the Director of the Bureau of the Budget (June 19, 1961).

JOURNAL OF RESEARCH of the National Bureau of Standards—C. Engineering and Instrumentation
Vol. 68C, No. 2, April–June 1964

Fringe Pattern of an Oscillating Fabry-Perot Interferometer

K. D. Mielenz

(December 17, 1963)

The dependence of the fringe pattern of an oscillating Fabry-Perot interferometer upon the vibration amplitude is discussed experimentally and theoretically. If the fringes of the stationary interferometer are wide, the fringe pattern tends to disappear at certain values of the amplitude. If the stationary fringes are narrow, a splitting of fringes occurs at certain amplitudes. In both cases, the stationary pattern reappears, with reduced contrast, at intermediate amplitudes.

The practicability of using these effects for the measurement of vibration amplitudes is discussed.

1. Introduction

In a recent paper [1],[1] a photoelectric spectrum analyzer was described that consisted of a Fabry-Perot etalon with a piezoelectric ceramic tube incorporated into the spacer. If an a-c voltage of circular frequency ω is applied to the ceramic, the length of the etalon, d, varies with time, t, according to

$$d=d_0+d_1 \cos \omega t. \tag{1}$$

The static length of the etalon, d_0, was 10 cm in one experiment, 8 mm in another. The vibration amplitude, d_1, is of the order of a few wavelengths. It is proportional to the peak voltage applied, V_1; the ratio was, in both cases, $d_1/V_1=1.5$ mμ/v. A 60-cycle a-c voltage was used. For both experiments, the green line of Hg 198 was chosen to illuminate the interferometer.

The visual observation of the Haidinger fringe patterns of these oscillating interferometers reveals a peculiar behavior:

As the vibration amplitude increases, the fringe pattern of the 10-cm etalon almost disappears at certain discrete values of the amplitude and reappears at intermediate values; figure 1.

With the 8-mm etalon, on the other hand, the pattern also reappears at certain amplitudes but, instead of vanishing at intermediate amplitudes, it appears as a double pattern; i.e., with each fringe split into two, figure 2.

The contrast of the pattern in both cases gradually decreases as the amplitude increases.

Fringe disappearance, as in the first case, is well known from oscillating two-beam interferometers. Described by Osterberg more than 30 years ago [2], it is now the basis of an established technique of measuring small vibration amplitudes [3].

As of this writing, the obviously more complex behavior of the oscillating multiple-beam Fabry-Perot interferometer, however, has not yet been explained.

2. Theory

Consider an etalon of length d, and let T and R be the transmission and reflection coefficients of the etalon plates. Its transmission is

$$A(\nu, d, i)=T^2(1+R^2-2R \cos \varphi)^{-1}, \tag{2}$$

with

$$\varphi=\beta\nu, \tag{3}$$

$$\beta=(4\pi/c)d \cos i, \tag{4}$$

c=speed of light,

ν=frequency,

i=angle of observation.

[1] Figures in brackets indicate the literature references at the end of this paper.

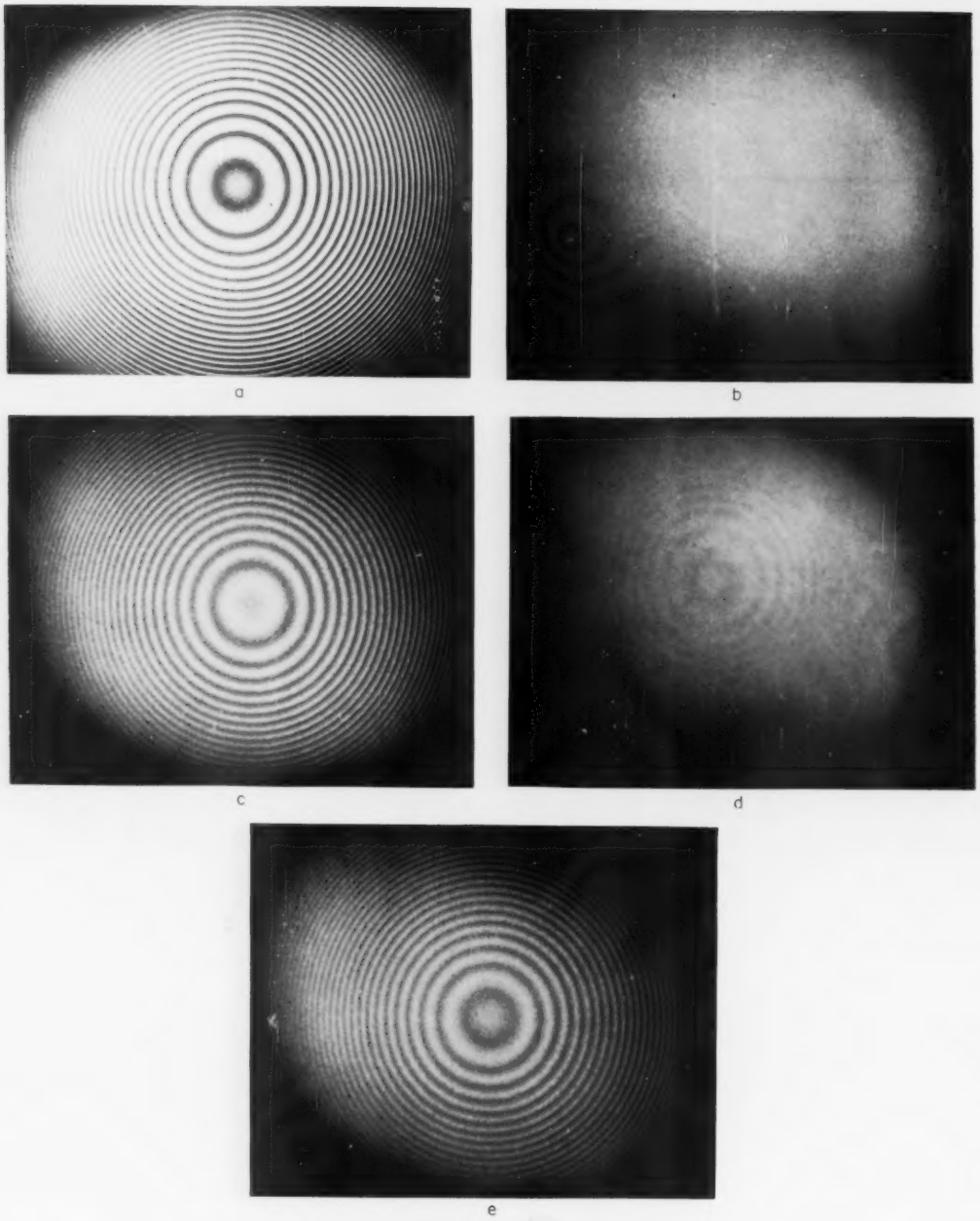

FIGURE 1. *Fringe pattern of oscillating 10-cm etalon, for* $V_1 = 0$, *68, 110, 154, and 201 v.*

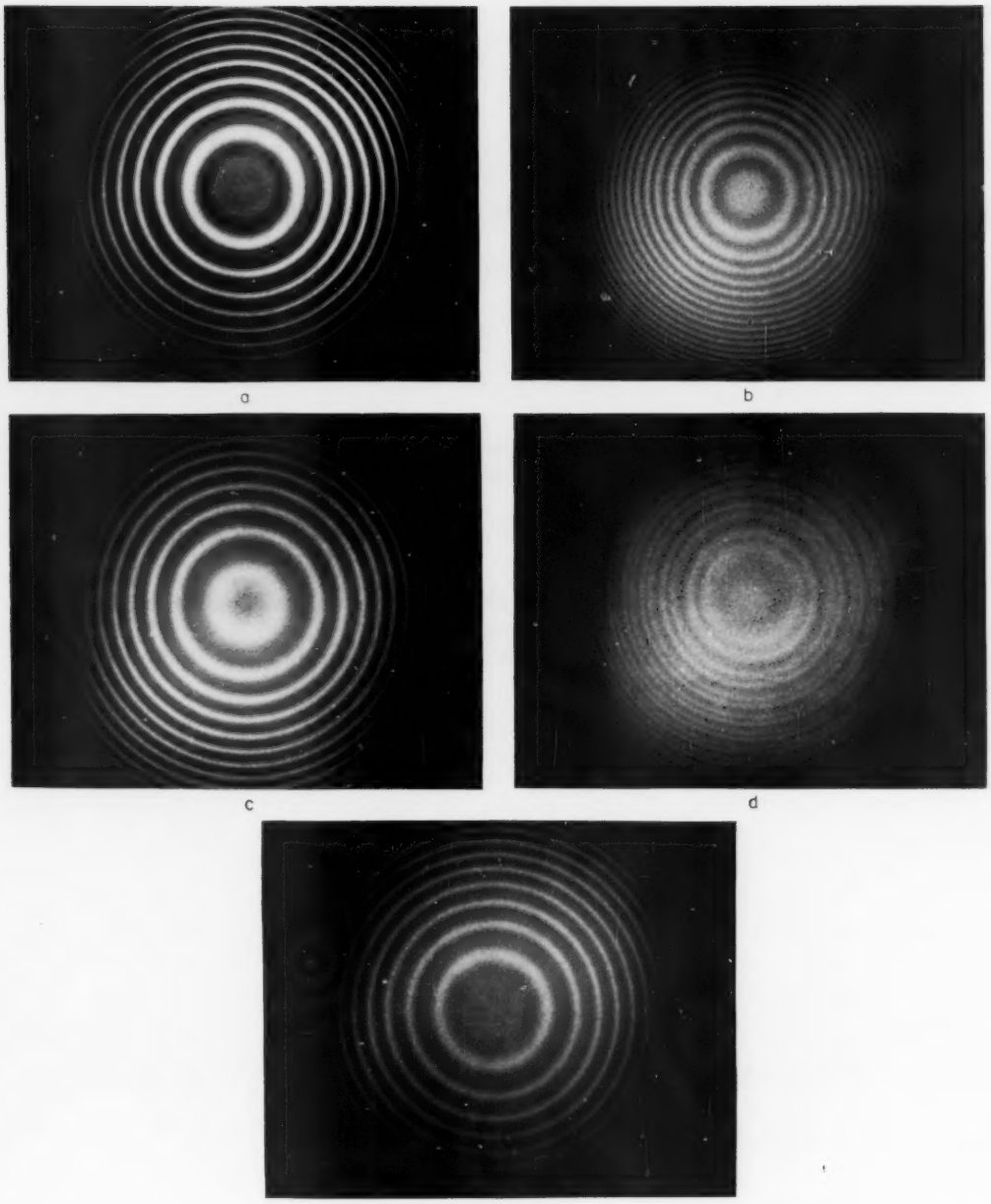

FIGURE 2. *Fringe pattern of oscillating 8-mm etalon, for* $V_1=0$, *46, 96, 148, and 178 v.*

Let

$$D(\nu)=Ce^{-\alpha^2(\nu-\nu_0)^2}=Ce^{-(\alpha/\beta)^2(\varphi-\phi)^2} \tag{5}$$

be the Doppler distribution of the illuminating light, ν_0 being its principal frequency. Here,

$$\begin{aligned} &C,\ \alpha=\text{constants},\\ &\phi=\beta\nu_0. \end{aligned} \tag{6}$$

Monochromatic light, of frequency ν, is then observed in a given direction i with the intensity

$$I_\nu(d,\ i)=D(\nu)A(\nu,\ d,\ i).$$

The total intensity observed in that direction is

$$I(d,\ i)=\int_0^\infty I_\nu(d,\ i)d\nu, \tag{7}$$

which, upon substitution of (1), yields the instantaneous intensity distribution in the fringe pattern of the oscillating etalon. The actually observed time average, then, is

$$<I(d_0, d_1, i)>=(1/2\pi)\int_0^{2\pi} I(d_0+d_1\cos\omega t, i)d(\omega t). \tag{8}$$

It is probably impossible to solve this integral in a closed form. A solution can be obtained, however, by expanding the integrand into a Fourier series as follows.

In the usual derivation of the Airy formula (2), the complex amplitude of the wave transmitted by the etalon is obtained as [4]

$$P=T\sum_j R^j e^{-ij\varphi}.$$

The intensity is

$$\begin{aligned} A=PP^*&=T^2\sum_{j,k}R^jR^ke^{-ij\varphi}e^{ik\varphi}\\ &=T^2\left(\sum_{n=0}^\infty R^{2n}+\sum_{n=1}^\infty(e^{in\varphi}+e^{-in\varphi})\sum_{m=0}^\infty R^{n+2m}\right)\\ &=T^2/(1-R^2)\left(1+2\sum_{n=1}^\infty R^n\cos n\varphi\right). \end{aligned} \tag{9}$$

Thus,

$$I(d,\ i)=CT^2/(1-R^2)\left[\int_0^\infty e^{-(\alpha/\beta)^2(\varphi-\phi)^2}d(\varphi/\beta)+2\sum_{n=1}^\infty R^n\int_0^\infty e^{-(\alpha/\beta)^2(\varphi-\phi)^2}\cos n\varphi\ d(\varphi/\beta)\right].$$

Since $e^{-(\alpha/\beta)^2x^2}$ is essentially zero for $-\infty<x<-\phi$, we have

$$\begin{aligned} \int_0^\infty e^{-(\alpha/\beta)^2(\varphi-\phi)^2}\cos n\varphi\ d\varphi&=\cos n\phi\int_{-\infty}^{+\infty}e^{-(\alpha/\beta)^2x^2}\cos nx\ dx\\ &\quad-\sin n\phi\int_{-\infty}^{+\infty}e^{-(\alpha/\beta)^2x^2}\sin nx\ dx=\cos n\phi(\sqrt{\pi}\beta/\alpha)e^{-(n\beta/2\alpha)^2}-0. \end{aligned}$$

Therefore,

$$I(d,\ i)=K\left(1+2\sum_{n=1}^\infty R^n e^{-(n\beta/2\alpha)^2}\cos n\phi\right), \tag{10}$$

with

$$K=\sqrt{\pi}/\alpha\cdot CT^2/(1-R^2). \tag{11}$$

For the oscillating etalon,

$$\phi=(4\pi\nu_0/c)(d_0+d_1\cos\omega t)\cos i$$
$$=\phi_0+\phi_1\cos\omega t, \tag{12}$$

and

$$\beta/2\alpha=(2\pi/\alpha c)(d_0+d_1\cos\omega t)\cos i. \tag{13}$$

Neglecting the time as well as the angular dependence of the exponential function, we obtain

$$I(d_0, d_1, i)=I(\phi_0, \phi_1)=K\left[1+2\sum_{n=1}^{\infty}R^n e^{-(2n\pi d_0/\alpha c)^2}\cos(n\phi_0+n\phi_1\cos\omega t)\right], \tag{14}$$

where ϕ_0 determines the static pattern, and ϕ_1 describes the vibration amplitude. This is the Fourier expansion of the integrand in (8).

Hence,

$$<I(\phi_0, \phi_1)>=(K/2\pi)\left[\int_0^{2\pi}d(\omega t)+2\sum_{n=1}^{\infty}R^n e^{-(2n\pi d_0/\alpha c)^2}\int_0^{2\pi}\cos(n\phi_0+n\phi_1\cos\omega t)\,d(\omega t)\right].$$

With

$$\int_0^{2\pi}\cos(n\phi_0+n\phi_1\cos\omega t)\,d(\omega t)=\cos n\phi_0\int_0^{2\pi}\cos(n\phi_1\cos\omega t)\,d(\omega t)$$
$$-\sin n\phi_0\int_0^{2\pi}\sin(n\phi_1\cos\omega t)\,d(\omega t)=2\pi\cos n\phi_0 J_0(n\phi_1)+0,$$

where J_0 is the Bessel function of zero order, we finally obtain

$$<I(\phi_0, \phi_1)>=K\left[1+2\sum_{n=1}^{\infty}R^n e^{-(2n\pi d_0/\alpha c)^2}\cos n\phi_0\, J_0(n\phi_1)\right]. \tag{15}$$

This is the desired time-average of the intensity distribution in the fringe pattern of the oscillating etalon.

3. Discussion

3.1. Calculation of $2\pi d_0/\alpha c$

For the experiments described in this paper, the green line of Hg 198 was used. Its half-width is, approximately, $2(\nu-\nu_0)_{1/2}=8\cdot10^8\ \mathrm{sec}^{-1}$. Thus, from (5),

$$e^{-\alpha^2(4\cdot10^8\ \mathrm{sec}^{-1})^2}=\tfrac{1}{2},$$

$$\alpha^2 16\cdot10^{16}\ \mathrm{sec}^{-2}=0.7,$$

$$\alpha=2.1\cdot10^{-9}\ \mathrm{sec},$$

and

$$2\pi d_0/\alpha c=d_0\cdot10^{-1}, \tag{16}$$

with d_0 in cm.

3.2. The Long Etalon: Fringe Disappearance

For the experiment of figure 1, the data of the etalon were $d_0=10$ cm and $R=0.8$. Thus, from (15) and (16),

$$<I(\phi_0, \phi_1)>=K\left[1+2\sum_{n=1}^{\infty}(0.8)^n e^{-n^2}\cos n\phi_0\, J_0(n\phi_1)\right].$$

This series converges very fast. To obtain $<I(\phi_0, \phi_1)>/<I(0, 0)>$ to better than four decimals, it suffices to consider the first two terms of the sum only; $n\leq2$.

A plot of $\langle I \rangle$ versus ϕ_1 is shown in figure 3 for $\phi_0 = 2m\pi$ (bright stationary fringes), $\phi_0 = (2m+1)\pi$ (dark stationary fringes), and $\phi_0 = (2m+\frac{1}{2})\pi$; $m = 0, \pm 1, \pm 2, \ldots$. The first two curves show maxima, or minima, at $\phi_1 = 0, 3.9, 7.1, \ldots$. For intermediate amplitudes, $\phi_1 = 2.4, 5.5, \ldots$, the three curves practically cross each other in one point.

The intensity distribution in the fringe pattern ($\langle I \rangle$ versus ϕ_0) is shown in figure 4 for these significant values of ϕ_0. The pattern practically disappears for $\phi_1 = 2.4$ and 5.5. It reappears as a "negative" (dark fringes instead of bright ones) for $\phi_1 = 3.9$, and as a "positive" (fringes in their original positions) for $\phi_1 = 7.1$. As ϕ_1 increases, the contrast decreases.

The peak voltages V_1 at which these conditions were actually observed are listed in table 1; the corresponding vibration amplitudes d_1 are proportional to these voltages. As must be expected from (12) if the theory is correct, the ratio ϕ_1/V_1 is a constant, here equal to 0.035 v^{-1}.

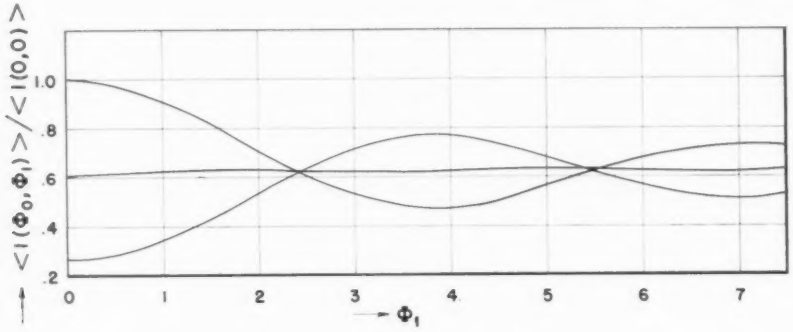

FIGURE 3. $\langle I \rangle$ *versus* ϕ_1 *for* $\phi_0 = 2m\pi$, $(2m+\frac{1}{2})\pi$, *and* $(2m+1)\pi$. 10-cm etalon.

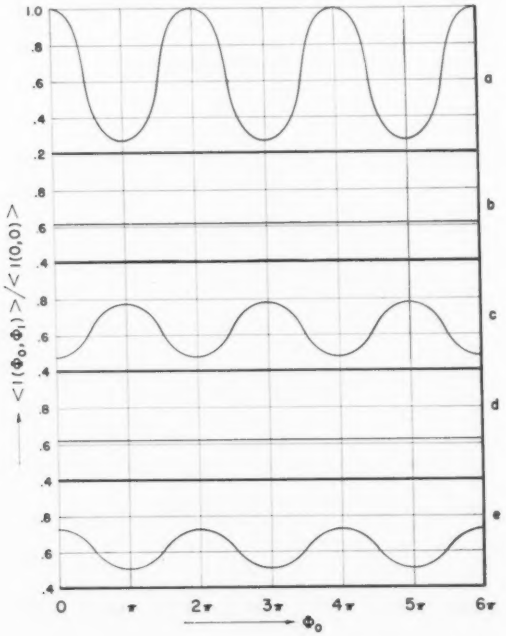

FIGURE 4. *Theoretical intensity distribution in fringe pattern of 10-cm etalon, for* $\phi_1 = 0$, *2.4, 3.9, 5.5, and 7.1.*

TABLE 1. *Significant amplitudes, ϕ_1, and peak voltages, V_1, for 10-cm etalon*

Pattern	ϕ_1	V_1	ϕ_1/V_1
		Volts	*Volt*$^{-1}$
Disappeared	2.4	68	0.035
Negative	3.9	110	.036
Disappeared	5.5	154	.036
Positive	7.1	201	.035

3.3. The Short Etalon: Fringe Splitting

For figure 2, an etalon of 8 mm length and, again, 80 percent reflectivity was used. Therefore, from (15) and (16),

$$<I(\phi_0, \phi_1)>=K\left[1+2\sum_{n=1}^{\infty}(0{\cdot}8)^n e^{-6n^2\cdot 10^{-3}}\cos n\phi_0\, J_0(n\phi_1)\right].$$

The convergence of this expansion is rather poor. It takes 10 terms of the sum; $n\leq 10$, to obtain $<I(\phi_0, \phi_1)>/<I(0, 0)>$ to about two decimals. This accuracy, however, is sufficient for our purpose.

The plot of $<I>$ versus ϕ_1, again for $\phi_0=2m\pi$, $(2m+1)\pi$, and $(2m+\frac{1}{2})\pi$, is shown in figure 5. Quite contrary to the corresponding graph in figure 3, the three curves cross each other in no single point. The fringe pattern can therefore no longer be expected to disappear at certain vibration amplitudes. The curves for $\phi_0=2m\pi$ and $(2m+1)\pi$ are no longer mirror images of each other; they have maxima at $\phi_1=0$, 6.4, . . ., and $\phi_1=3.4$, . . ., respectively. The curve for $\phi_0=(2m+\frac{1}{2})\pi$, practically a straight horizontal line in figure 3, now has pronounced peaks also; at $\phi_1=1.7$, 4.9, ...

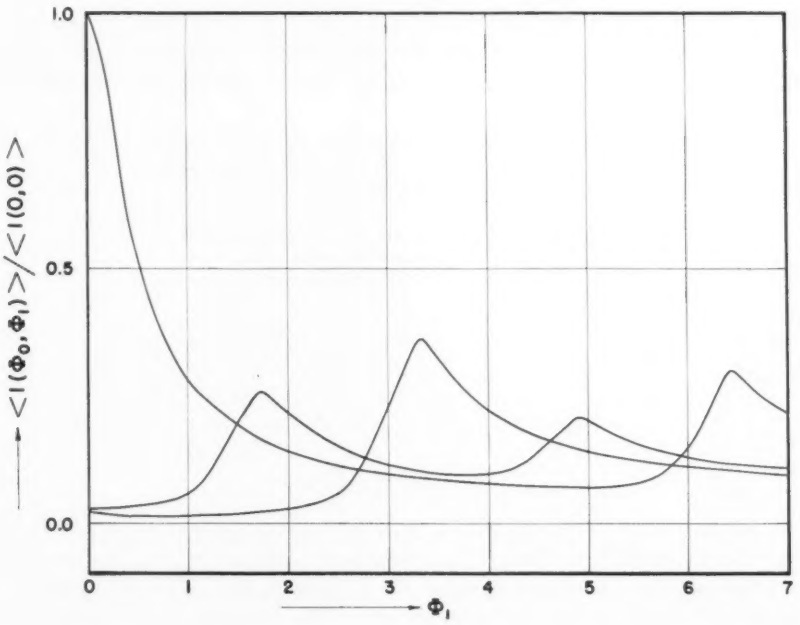

FIGURE 5. $<I>$ *versus* ϕ_1 *for* $\phi_0=2m\pi$, $(2m+\frac{1}{2})\pi$, *and* $(2m+1)\pi$.
8=mm etalon.

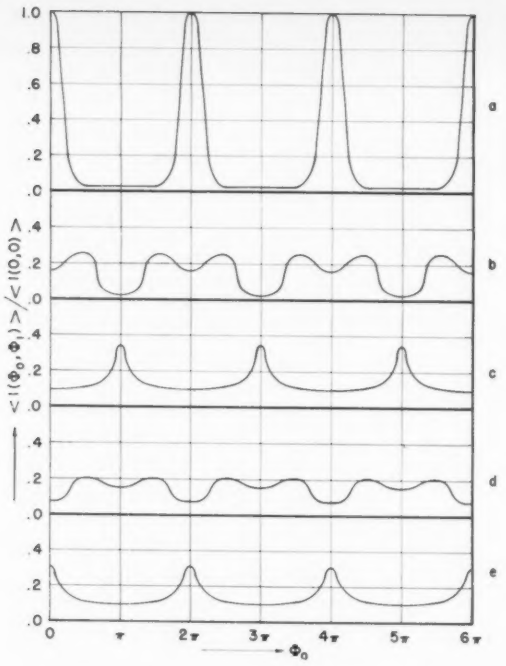

FIGURE 6. *Theoretical intensity distribution in fringe pattern of 8-mm etalon, for $\phi_1=0$, 1.7, 3.4, 4.9, and 6.4.*

Figure 6 shows $\langle I \rangle$ versus ϕ_0, the intensity distribution in the fringe pattern. One sees, as in figure 2, (a), the stationary pattern at $\phi_1=0$, (b), the split "positive" pattern at $\phi_1=1.7$, (c), the "negative" pattern at $\phi_1=3.4$, (d), the split "negative" pattern at $\phi_1=4.9$, and (e), the reappearance of a "positive" pattern at $\phi_1=6.4$. Again, the overall contrast decreases as ϕ_1 increases.

The peak voltages V_1 at which the photographs in figure 2 were taken are compared to these ϕ_1-values in table 2. Again, the agreement between experiment and theory is satisfactory as ϕ_1/V_1 turns out to be the same constant as in table 1.

TABLE 2. *Significant amplitudes, ϕ_1, and peak voltages, V_1, for 8-mm etalon*

Pattern	ϕ_1	V_1	ϕ_1/V_1
		Volts	*Volt*$^{-1}$
Split	1.7	46	0.037
Negative	3.4	96	.035
Split	4.9	148	.033
Positive	6.4	178	.036

4. Conclusions

The fringe pattern of oscillating Fabry-Perot etalons, as shown in figures 1 and 2, are fully explained by the above theory. Fringe disappearance, such as also obtained with an oscillating two-beam interferometer, is observed when the fringes in the stationary pattern are broad. Fringe splitting is found when they are narrow. The vibration amplitudes significant for fringe reappearance, and disappearance or splitting, are different in the two cases.

The behavior of the pattern, thus, depends entirely upon experimental circumstances such as, the length of the etalon, the reflectance of the etalon plates, and the width of the

spectrum line used for illumination. Mathematically, these factors determine the rate of convergence of the series expansion (15) and, thus, the distinction between the two border cases.

For an oscillating two-beam interferometer, no such dependence upon experimental circumstances exists. For the measurement of vibration amplitudes, therefore, an oscillating multiple-beam interferometer appears to be less practicable than a two-beam interferometer.

5. References

[1] K. D. Mielenz, R. B. Stephens, and K. F. Nefflen, J. Res. NBS **68C** (Eng. and Instr.) No. 1, 1–6 (1964).
[2] H. Osterberg, J. Opt. Soc. Am. **22,** 19 (1932).
[3] For instance: V. A. Schmidt, S. Edelman, E. R. Smith, and E. T. Pierce, J. Acoust. Soc. Am. **34,** 455 (1962).
[4] R. W. Ditchburn, Light, p. 138 (Interscience Publishers Inc., New York 1961).

(Paper 68C2–152)

720–591—64——2

JOURNAL OF RESEARCH of the National Bureau of Standards—C. Engineering and Instrumentation
Vol. 68C, No. 2, April–June 1964

Interferometer for Testing Extended Surfaces Such as Surface Plates and Precision Ways

J. B. Saunders and John V. McDermott

(January 21, 1964)

A modification of the previously described "Interferometer for Large Surfaces" is described that permits the use of smaller prisms for a given sensitivity and a more practical arrangement of the optics. This arrangement allows for better structural connection of the elements into a rigid and moveable unit. This is obtained by a 90 degree rotation of the prism relative to the plane of incidence of the light.

Since publishing a description of the interferometer for large surfaces [1] these authors have considered means of facilitating its construction and applications. The modified version permits the use of a smaller prism for attaining the same sensitivity. The elements are more easily combined (mechanically) into a rigid unit.

Figure 1 is a view of the optical elements. Light from a monochromatic source is collimated before entering the plane entrance face of a Kösters prism. The beam is divided by amplitude division at the semireflecting dividing plane. After total internal reflection inside the prism the two component beams emerge parallel and normal to the prism face. One component beam, after emergence from the Kösters prism, is reflected normally from a mirror so that it returns along its path of incidence to the dividing plane. The other component beam is deviated by a plane wedge so that it is incident onto the surface to be tested. A second mirror receives this beam and returns it (after a second reflection from the surface being tested) along its previous path to the beam divider. The two component beams recombine at the beam divider and after a second division a component of each beam is received by the observer.

If the two paths are approximately equalized interference fringes of good contrast are observed.

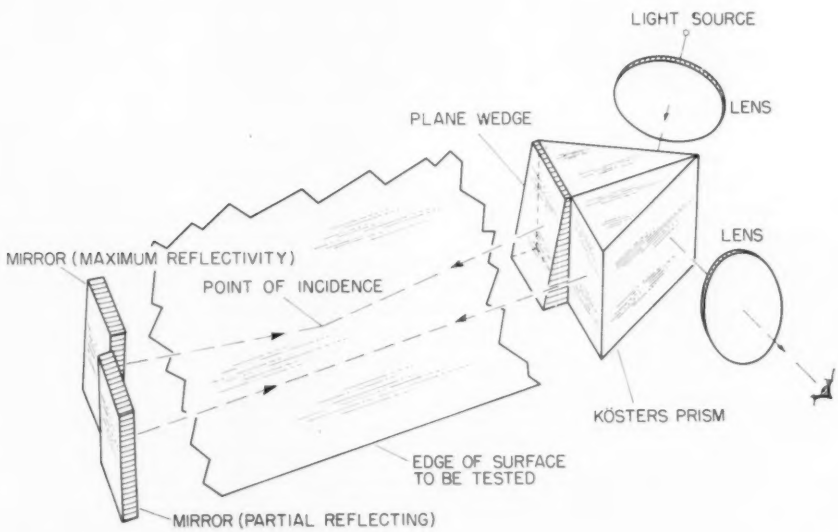

FIGURE 1. *A plan view showing the arrangements of elements for a compact surface plate interferometer.*

[1] An interferometer for testing large surfaces, by James B. Saunders and Franz L. Gross, J. Res. NBS **62** (Apr. 1959) RP2943.

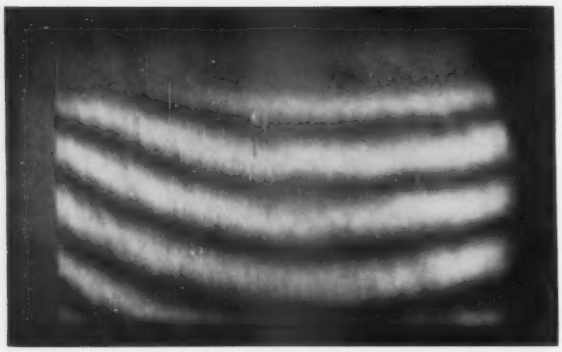

FIGURE 2. *Interference fringes with light reflected from a 24 in. black granite surface plate.*

The width and orientation of the fringes may be altered at will by adjusting either of the two mirrors. Figure 2 show fringes from a 24 in. surface plate of black granite.

Since the reflectivities of all surfaces to be tested are well below unity one mirror must have a higher reflectivity if the two recombined beams are to be approximately equal.

When testing large surfaces of the type indicated, one is usually concerned with measurement of the surface along a line. Consequently, the horizontal width of the aperture (or field of interference) can be relatively small. The height (fig. 1) of the prism determines the length of surface that may be tested with a given sensitivity (angle of incidence). Thus, a prism with a horizontal cross section that is small, relative to its height, can be used. This reduces the difficulty of constructing a prism having a given vertical aperture.

It will be noted that all elements of this interferometer are above the plane of the test surface. The mirrors are placed laterally to each other instead of one vertically above the other, as in the previously described instrument (see footnote 1). These differences allow for simplification of the mechanics of the instruments. The sensitivity may be altered by replacing the plane wedge with another having a different deviation and then readjusting the distance between mirrors and prism.

The sensitivity of this interferometer is the same as that described (see footnote 1). One fringe corresponds to a departure from flatness of $\lambda/(4\cos\alpha)$, where λ is the wavelength and α the angle of incidence.

(Paper 68C2–153)

JOURNAL OF RESEARCH of the National Bureau of Standards—C. Engineering and Instrumentation
Vol. 68C, No. 2, April-June 1964

Ferrimagnetic Resonance in Polycrystalline Ferrite and Garnet Disks at L-Band Frequencies

W. E. Case, R. D. Harrington, and L. B. Schmidt

(January 15, 1964)

An experimental study made on the measurement of the gyromagnetic ratio and line width of four ferrimagnetic materials at L-band using thin disk-shaped samples in a rectangular TE_{102} mode cavity at 1107 Mc/s is described. The study emphasized ferrimagnetic resonant measurements on a one half inch diameter sample of a given material as a function of aspect ratio. Experimental results indicate that for three materials the gyromagnetic ratio could be accurately calculated from Kittel's equation for aspect ratios of 50 or greater. Because of an anomaly, the calculation was impossible for a fourth material, a nickel aluminum ferrite. Generally, very high aspect ratios are required to cause line width measurements to rapidly approach an asymptotic value.

1. Introduction

Considerable effort has recently been directed towards the development of ferrite and garnet devices such as isolators and circulators at the lower microwave frequencies. However, there is a lack of engineering information available on the line width and gyromagnetic ratio of ferrites at these frequencies even though these quantities are basic to the design of microwave devices. One of the simpler methods of measuring line width, ΔH, and the gyromagnetic ratio, γ, at higher microwave frequencies such as X-band has been based on the determination of the absorption of a small spherical sample in a nondegenerate rectangular mode cavity [1, 2].[1] This technique can be extended to L-band frequencies although in many cases it may be necessary to use thin polycrystalline disk-shaped samples rather than spheres in order to avoid magnetic saturation problems [3, 4]. However, in the case of disks, it is necessary to apply demagnetization corrections in calculating γ, as was pointed out by Kittel [5]. Furthermore, at L-band frequencies, it is necessary to use a disk orientation in the cavity which is more susceptible to dielectric effects than is usually the case at higher frequencies where smaller cavities of different modes may be used. It was thus the purpose of this study to determine the effects of sample size and geometry upon the accuracy of L-band ferrimagnetic magnetic resonance measurements. This involved an experimental study of line width and gyromagnetic ratio as a function of aspect ratio (diameter/thickness) of several ferrites.

2. Experimental Techniques

The development of a ferrimagnetic resonance measurement facility at L-band frequencies is subject to two basic requirements. First, the d-c field must be perpendicular to the plane of the disk-shaped sample and the RF field in order to avoid low field losses [4]. Secondly, the cavity must be designed so that it can be placed between the pole caps of a typical electromagnet. This latter requirement becomes somewhat more severe at L-band due to the large size cavity that must be utilized. However, both requirements are readily satisfied by placing the disk-shaped sample at the center of a TE_{102} rectangular transmission cavity (fig. 1), as was pointed out by Sirvetz and Zneimer [3].

The measurement procedure utilized for obtaining data in this study is similar to an attenuation technique which is being issued as an ASTM tentative method of test for Ferrimagnetic Resonance Line Width and Gyromagnetic Ratio of Nonmetallic

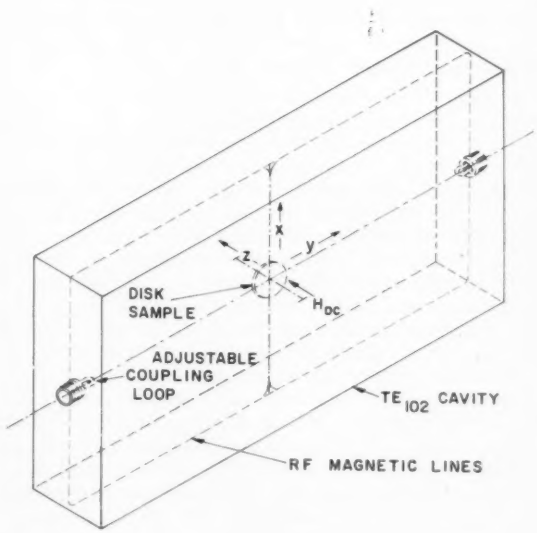

FIGURE 1. *Rectangular transmission cavity using TE_{102} mode at 1107 Mc/s.*

[1] Figures in brackets indicate the literature references at the end of this paper.

Magnetic Materials designated ASTM C524–63T. Our setup varies from the ASTM method in that the input power to the cavity is held constant and measurements are made with a precision attenuator located in the IF detection circuit following the cavity. The frequency is adjusted to give cavity resonance for the empty cavity, and the variable precision IF attenuator is set to A_0 to give a convenient output reference level, as indicated on the output detector. The sample is then inserted, the d-c magnetic field adjusted for maximum absorption in the sample, the frequency adjusted for cavity resonance, and the precision attenuator set to obtain the same output reference signal. The new attenuator reading is defined as A_r, and the d-c field reading is defined as H_r. The attenuator reading corresponding to the half-power points on the ferrimagnetic resonance loss curve of the sample is calculated from the following formula [6]:

$$A_{1/2}=A_0+20 \log 2-20 \log \left(10^{\frac{A_0-A_r}{20}}+1\right).$$

The attenuator is now set at the calculated $A_{1/2}$ value. The d-c magnetic field necessary to return the output power to its previous level on one side of resonance is then read and recorded. The d-c field is then similarly adjusted and recorded for the other side of resonance. The difference between these two d-c field measurements is the line width, ΔH.

The effective gyromagnetic ratio for the case of a sphere is determined from the formula

$$\gamma=\frac{2\pi f_r}{H_r} \tag{1}$$

where f_r is the microwave frequency required for cavity resonance at maximum sample absorption and H_r is the corresponding d-c field. In the case of a disk magnetized perpendicular to its plane, the gyromagnetic ratio is given by

$$\gamma=\frac{2\pi f_r}{H_r-(N_z-N_x)M_z} \tag{2}$$

which is Kittel's equation where the demagnetizing factors N_x and N_y are equal and $N_x+N_y+N_z=4\pi$. M_z is the magnetic moment per unit volume.

As can be seen in figure 1, the sample is oriented with its plane perpendicular to the E-field in the cavity. Even though it is at an electric field node, the diameter of the sample must be restricted in order to avoid errors due to dielectric effects. At higher frequencies where smaller cavities may be used, it is possible to pick a cavity mode in which the plane of a disk may be parallel to the electric field in the cavity. In these cases, dielectric effects are avoided by having a sufficiently thin sample located at an electric field node [7]. The necessity of placing the plane of the disk perpendicular to the E-field in the L-band cavity is not a serious problem due to the longer wavelength involved. This was experimentally verified by comparing H_r and line width data on disks of ½ in. diam with corresponding data on the same disk reduced to ¼ in. diam and ground to the same aspect ratio. Resonant field measurements agreed within 0.3 percent for a given sample for three different materials. The dielectric effect on H_r may thus be considered negligible. For a fourth material, a distinct diameter dependence anomaly was observed, as will be described below. Since the dielectric constant of this material is comparable to that of the other three materials, it is believed that this anomaly is not due to dielectric effects. In the case of line width measurements, the variation between different diameter disks may be as great as 5 percent for all four materials. This small diameter dependence was not considered a serious error since the accuracy of the line width measurements due to sample variations, etc., was also of the order of 5 percent. Furthermore, it will be noted later that much larger errors in line width may arise unless disks having large diameter to thickness ratios are used. It appears that a ½ in. disk offers a good compromise for keeping dielectric effects on line widths low while attaining high aspect ratios.

The samples were supported by a rexolite holder at the center of the cavity. The dielectric constant of the rexolite introduced negligible error in the measurement, as was determined from similar measurements using a polyfoam holder.

Possible errors due to wall effect were checked by measuring the disk at various distances from the broad wall of the cavity. The sample is normally placed at ½ of the distance between the broad walls. Placing the sample ¼ and ⅛ of this distance from one of the walls resulted in only negligible change in the resonant measurements.

Many of the materials designed for use at the low microwave frequencies have relatively low Curie temperatures which may introduce errors in the data due to ambient temperature fluctuations. This situation is more serious in disk samples since the temperature dependent magnetization appears in the gyromagnetic ratio formula as given in eq (2). These effects were essentially avoided by stabilizing the cavity temperature by means of coils carrying constant temperature water.

Having experimentally demonstrated that the above effects do not introduce appreciable errors in the measurements, the majority of the effort was directed towards a study of the dependence of ΔH and γ on the aspect ratio $\left(\frac{\text{diameter}}{\text{thickness}}\right)$ of the disks. Early measurements indicated that more consistent data could be obtained from a given sample that was alternately ground down and measured rather than comparing data from several different samples of the same material. Initially, ultrasonic machining and diamond wheel grinding were used to cut a disk sample to a given diameter and thickness. A small rotary grinder using aluminum oxide optical finishing powder was then used to grind off small increments of thickness allowing many measurements on the same sample with a given diameter. In general there

appeared to be no dependence of the resonance properties on surface finish for three of the materials, as was determined by using powders of different grit size. However, in the material noted above which showed anomalous effects for H_r, a surface finish dependence was noted.

3. Results

The four commercially available materials referred to above and for which the line width, ΔH, and resonant field, H_r, were determined as a function of the aspect ratio of the disks have the following general composition:

Sample A—Yttrium iron garnet
Sample B—Magnesium, manganese, aluminum ferrite
Sample C—Substituted yttrium iron garnet
Sample D—Nickel aluminum ferrite.

All measurements were made at 1107 Mc/s.

3.1. Gyromagnetic Ratio

Figure 2 shows H_r versus aspect ratio for the first three materials above. It can be seen that in at least two cases an asymptotic value of resonant field

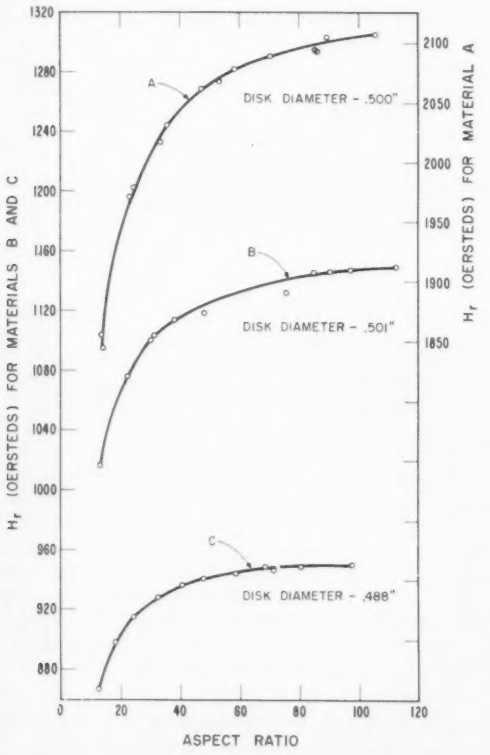

FIGURE 2. *Resonant field, H_r, versus aspect ratio for disk samples of three materials, A, B, and C.*

was not reached even for aspect ratios greater than 100, which in this case corresponds to disks less than 0.005 in. in thickness. This of course indicates that in such measurements it is not, in general, reasonable to assume that one has an infinitely thin disk such that demagnetization corrections are not needed. However, these curves essentially express the dependence of Kittel's relation as given in (2) on demagnetizing factors which are a function of the aspect ratio. The relationship between the demagnetizing factors of ellipsoidal samples and their aspect ratios has been given by Stoner [8]. Thus $(N_z - N_x)$ for a given disk may be readily obtained if we assume that the demagnetizing factors of an ellipsoid and disk of the same aspect ratio are identical. The value of magnetization, M_z, may be determined from an independent measurement using a magnetometer. Thus, knowing M_z and the value of $N_z - N_x$ as well as H_r as given on the curve for a given aspect ratio, one can calculate the gyromagnetic ratio from eq (2). This should be a constant, independent of aspect ratio. When this was done for the data shown in figure 2, it was found that the variation in γ as a function of aspect ratio for ratios of 50 or higher was less than 1 percent for each of the three samples. This was considered as satisfactory agreement between Kittel's equation and the observed data.

The validity of the assumption of equivalent demagnetizing factors for disks of the same aspect ratio was further substantiated by grinding ellipsoids from several disks keeping the aspect ratio approximately constant. A negligible effect on the measured value of H_r was observed. This assumption thus appears to be valid at least for polycrystalline materials for measurements of this type. It has been noted in the literature that this situation may not necessarily be true for other types of measurements such as the study of magnetostatic modes in single crystal disks [9].

The above discussion implies that Kittel's equation is quite applicable for predicting the gyromagnetic ratio of most samples. However, similar measurements taken on Material D, which is a nickel aluminum ferrite, showed an anomalous behavior as can be seen in figure 3. This material varies from the previous ones described in that H_r decreases for the higher aspect ratios and the data is strongly diameter dependent. Recent work indicates that H_r is also dependent upon surface finish. The cause of this behavior is not yet understood. However, it is apparent that Kittel's equation as given in (2) is not applicable for describing this material. It thus appears that care should be taken in applying Kittel's equation to an unknown sample without first determining that the material is not following an unusual behavior. This implies that it may be necessary to measure samples of several different aspect ratios when gyromagnetic ratio data is desired.

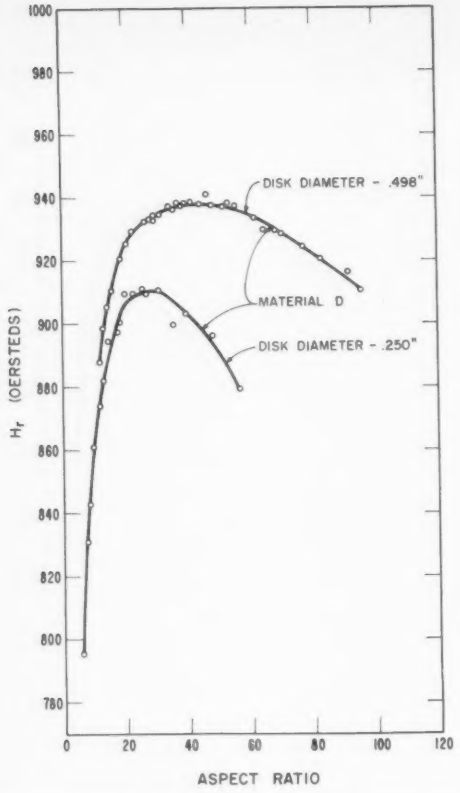

FIGURE 3. *Resonant field, H_r, versus aspect ratio for disk sample of material D.*

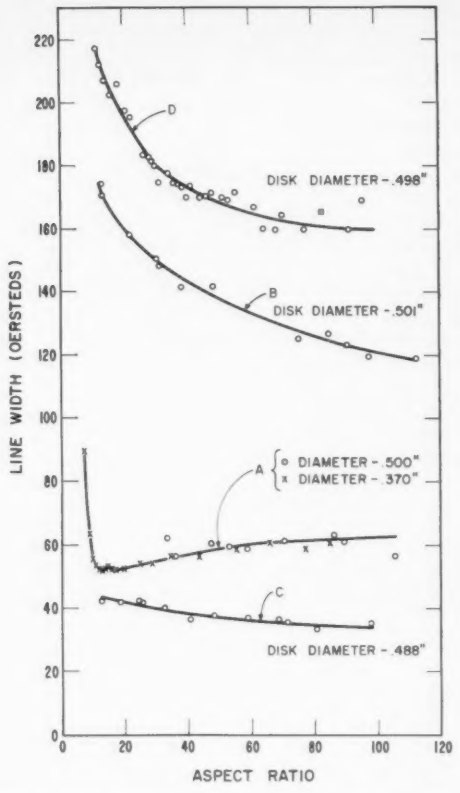

FIGURE 4. *Line width versus aspect ratio for disk samples of materials A, B, C, and D.*

3.2. Line Width

Figure 4 shows the line width of materials A through D as a function of the aspect ratio of the disk-shaped samples. Here again, it is seen that it is difficult to obtain disks sufficiently thin in order to obtain an asymptotic value of line width. It may thus be necessary to obtain data at several different values of aspect ratio and extrapolate the results to the higher aspect ratios in order to obtain meaningful information on line width. It is readily apparent that samples B, C, and D are displaying similar phenomena in that they show a relatively slow decrease in line width as the aspect ratio increases. This decrease in line width with increasing aspect ratio is probably due to inhomogeneous field effects as well as incomplete saturation of the individual crystallites. The inhomogeneous field effect might be expected to result in magnetostatic modes arising from field inhomogeneities due to spacial variations in the demagnetizing field resulting from deviation of the disks from true ellipsoids such as described by Geschwind and Clogston [10]. The problem of incomplete saturation might be expected to cause a line broadening if the relatively low internal d-c fields in the disk required for resonance at L-band become of the same order of magnitude as the anisotropy fields such as discussed by Suhl et al. [11]. The greatest variation in line width with aspect ratio in the data given in figure 4 appears on the low field side of the resonance curves. This effect might be expected for both line broadening mechanisms described above. As such, it does not appear possible at the present time to separate the effects due to saturation from the various possible inhomogeneous field effects that may be present in this data. One further point of interest in regard to this data is that sample D does not display an anomalous behavior in line width even though there was a strong dependence of resonant field on diameter and surface finish.

Sample A, which is yttrium iron garnet, shows a somewhat different dependence of line width with aspect ratio. For this case, the line width appears to be relatively constant for the higher aspect ratios. As can be seen, it is possible that there is actually a slight increase in line width as the aspect ratio

increases in this material. This apparent increase in line width for the higher aspect ratios is not entirely understood although here again, the increase is largely due to changes in the low field side of the resonance curve. It is also of interest to note that the resonance curves for this material were in general more symmetrical than for the previous materials B, C, and D. This is in agreement with data obtained on single crystal disks of YIG by Smith and Watanabe [12]. The ½ in. diam samples of this material proved to be too lossy for measurements at the lower aspect ratios. However, data taken on a smaller ⅜ in. diam sample of yttrium iron garnet indicated that there is a very large increase in line width at aspect ratios of the order of ten or less. This is presumably due to the fact that these samples are becoming magnetically unsaturated at the lower aspect ratios. It should also be noted that variations in data on different samples of the same diameter cut from the same block were noted for this material. This apparent inhomogeneity in such materials considerably effects the precision of measurements such as described above when different samples must be used.

A final remark concerning the comparison of line width measurements between ellipsoids and disks of the same aspect ratio for the above four materials may be of interest. It has previously been mentioned that a negligible variation in resonant field was noted when a disk was ground to an ellipsoid of the same aspect ratio. However, for the case of samples B, C, and D, the ellipsoid had a smaller line width than the disk of the same aspect ratio. For sample A, the ellipsoid had a greater line width than the corresponding disk. This suggests that magnetostatic mode phenomena affects the line width but not the resonant field in these polycrystalline materials.

4. Conclusions

1. The use of a TE_{102} rectangular cavity is quite applicable for measuring the effective line width and gyromagnetic ratio of disk-shaped samples at L-band frequencies.

2. In many cases, it may be necessary to obtain line width and gyromagnetic ratio as a function of aspect ratio and extrapolate the data to obtain the asymptotic values for these quantities. However, for many materials, the gyromagnetic ratio of a finite disk may be calculated from Kittel's equation if one uses the appropriate demagnetizing factors and has a value of M available.

3. In at least one case such as nickel aluminum ferrite, it is not possible to fit Kittel's equation in its usual form to the curves giving resonant field as a function of aspect ratio. Such an anomaly appears to be associated with both a diameter and surface finish dependence of H_r as a function of the aspect ratio. Considerable care should thus be given to the interpretation of data of this type on such materials at L-band frequencies.

5. References

[1] Artman, J. O., and P. E. Tannenwald, Measurement of susceptibility tensor in ferrites, J. Appl. Phys. **26,** No. 9, 1124–1132 (1955).

[2] Soohoo, R. F., Theory and application of ferrites, pp. 92–99 (Prentice-Hall, Inc., Englewood Cliffs, New Jersey, 1960).

[3] Sirvetz, M. H., and J. E. Zneimer, Microwave properties of polycrystalline rare earth garnets, J. Appl. Phys. **29,** 431 (1958).

[4] Lax, B., and K. J. Button, Microwave ferrites and ferrimagnetics, pp. 484–485 (McGraw-Hill Company, Inc., New York, N.Y., 1962).

[5] Kittel, C., On the theory of ferromagnetic resonance absorption, Phys. Rev. **73,** 155–161 (1948).

[6] Preston, C. C., and W. E., Case, Tables to facilitate the determination of the ferrimagnetic resonance line width of non-metallic magnetic materials, NBS Tech. Note No. 173 (Apr. 1963).

[7] Von Aulock, W., and J. H. Rowen, Measurement of dielectric and magnetic properties of ferromagnetic materials at microwave frequencies, Bell System Tech. J. **XXXVI,** No. 2, 427 (1947).

[8] Stoner, E. C., The demagnetizing factors for ellipsoids, Phil. Mag. (7) **36,** 803–821 (1945).

[9] Dillon, J. F., Magnetostatic modes in disks and rods, J. Appl. Phys. **31,** No. 9, 1605–1614 (Sept. 1960).

[10] Geschwind, S., and A. M. Clogston, Narrowing effect of dipole forces on inhomogeneously broadened lines, Phys. Rev. **108,** No. 1, 49–53 (Oct. 1957).

[11] Suhl, H., L. G. Van Uitert, and J. L. Davis, Ferromagnetic resonance in magnesium-manganese aluminum ferrite between 160 and 1900 Mc, J. Appl. Phys. **26,** No. 9, 1180 (Sept. 1955).

[12] Smith, A. W., and A. Watanabe, Ferrimagnetic resonance in a single-crystal disk of yttrium iron garnet, J. Appl. Phys., Supplement to Volume **32,** No. 3, 155S (1961).

(Paper 68C2–154)

JOURNAL OF RESEARCH of the National Bureau of Standards—C. Engineering and Instrumentation
Vol. 68C, No. 2, April–June 1964

Changes in the Influence of Atmospheric Humidity During Fatigue of an Aluminum Alloy

John A. Bennett

(December 12, 1963)

The fatigue strength of 6061–T6 aluminum alloy specimens was found to be about 14 percent higher in a dry atmosphere than in a moist one. A series of experiments in which the humidity was changed after various numbers of cycles indicated that there was an initial period during which the presence of water vapor had no effect on the total fatigue life. After this initial period, cracks developed and propagated much more rapidly in a moist atmosphere than in a dry one. The change in sensitivity to the environment is believed to result from rupture of the oxide film when the plastic strain becomes locally concentrated.

I. Introduction

In recent years there has been a revival of interest in the effects of environment on fatigue properties of metals. This interest has stemmed from several factors including (1) the need for accurate fatigue data for aircraft design purposes, so that the effect of mild corrosive agents such as water vapor can no longer be ignored; (2) the increased emphasis on mechanical tests in high vacuum resulting from the requirements of the space program; (3) the realization that the study of surface reactions can provide significant information regarding the mechanism of fatigue.

Results from a number of investigations have emphasized the importance of variations in humidity on the fatigue properties of aluminum alloys. Liu and Corten [1]* found that there was an inverse relation between the fatigue lives of aluminum alloy wires and the moisture content of the air during the tests. Although they made no effort to control the humidity, the variation in the laboratory over a period of months was sufficient to cause a difference of more than two to one in the mean fatigue life of specimens tested at a given stress amplitude. Coating their specimens with petroleum jelly reduced the variation, but did not result in as long a life as that of the specimens tested in dry air. Broom and Nicholson [2] used equipment in which a variety of atmospheres, including a high vacuum (2×10^{-6} torr), could be maintained around the specimen. They summarized the results of their tests on aluminum alloys by the conclusion that "the only constituent of normal air that significantly affects the fatigue life of age-hardened aluminum alloys is water vapour."

The results of the latter investigation provided some information on the relative influence of humidity on crack initiation and crack propagation, although there are certain inconsistencies. A few experiments in which the environment was changed during the fatigue test indicated that the total life was influenced only by the conditions during the latter part of the life, i.e., during crack propagation. However, the authors state that these results, taken in conjunction with the results of metallographic examination, "confirm that both crack initiation and growth are affected by the presence of water vapour."

The observation of gas evolution at the surface of specimens during fatigue testing appears to offer a new tool for studying the effects of environment, particularly on aluminum alloys. As reported by Holshouser and Bennett [3], this evolution can be seen readily, with specimens of the proper configuration, if a piece of transparent pressure-sensitive tape is applied to the surface of the test section. The gas, which is produced only during the latter part of the test, forms bubbles in the adhesive and lifts the tape from the surface. It was also observed that the tape had a marked effect on the fatigue life, presumably because it restricted the access of water vapor to the surface. In a few tests the specimens were stressed without tape for approximately half of their expected life, then the tape was applied; the total life in these tests was not significantly different from that obtained when the tape had been applied before stressing.

This result and the observations by Broome and Nicholson both suggested that there was a change in the nature of the reaction between the metal and its environment during the course of the fatigue process. In order to verify the occurrence of this change and to determine at what point it occurred, it appeared desirable to conduct a series of tests in which the environment was changed at different stages of the test. As the gas evolution phenomenon also indicated a change in the nature of surface reactions, there also appeared to be a need for experiments to determine if there was a relationship between the two changes.

* Figures in brackets indicate the literature references at the end of this paper.

2. Materials and Testing Technique

The design of the test specimen was dictated to a large extent by the need for a configuration on which the evolution of gas could be observed. This requires that the fatigue cracks initiate in a surface to which pressure-sensitive tape can be firmly applied, and that the gas be unable to escape from under it. Many of the experiments reported in reference [3] were conducted with specimens of rectangular cross section which were stressed in torsion. These met the above requirement, but because of the extensive cracking that preceded fracture, it was difficult to define failure in a satisfactory manner. Also the probability of crack initiation is the same on two faces, one of which is difficult to inspect. For these reasons it was considered preferable to use specimens stressed in bending. The tape requirement can be met with a bend specimen if the cross section is thicker in the middle than it is at the edges so that the cracks do not start at the corners of the section. The design finally selected is shown in figure 1a.

Specimens were cut from a 120° sector of tubing, and the reduced section was formed by a 2-in. radius cut tangent to the inside surface of the tubing. They were stressed in cantilever bending, and it was found that all of the cracks started in the top surface if a mean tensile stress equal to ⅓ of the stress amplitude was present in this surface. Tape could readily be applied to cover the test area, as it was singly curved with a radius of ¾ in.

The specimens were made from commercial 6061–T6 aluminum alloy tubing. The selection of this alloy was based on the results of a previous investigation [4] in which the fatigue properties of 6061–T6 specimens were found to show less dispersion than either 2024–T4 or 7075–T6. The aging behavior of the material was determined with samples from each piece of tubing used for specimen blanks. The aging temperature used was 320 °F (160 °C). Maximum hardness was attained in about 30 hr and no significant drop occurred in an additional 60 hr. Consequently, the specimen blanks were solution treated at 970 °F (520 °C) for 30 min, quenched in water, and aged 48 hr at 320 °F (160 °C). This resulted in an average hardness of about 96 Rockwell F.

The specimens were machined and polished after heat treatment. Coarse circumferential polishing was carried out before the tubes were sectioned. After the specimens were machined they were polished longitudinally, the final operation being hand polishing with No. 600 paper. In order to have the abrasive conform to the curvature of the specimen adhesive-backed paper was mounted in a tube having an inside diameter of 1⅝ in. For the sake of uniformity, all specimens were given a brief final polish and inspection on the same day that they were to be tested. They were then measured as described below and finally they were washed in two successive baths of clean benzene. On removal from the second bath they were immediately inserted in the testing machine.

The minimum section of this specimen is a segment of a circle, so it was necessary to know the radius of curvature and thickness in order to calculate the minimum section modulus. Both of these dimensions were measured on each specimen, as it was found that the variations in radius were too large to be ignored.

The fatigue testing machine used for these experiments was of the constant load-amplitude type, the load being applied by an eccentric weight rotated 1800 rpm by a synchronous motor. The alternating load was applied to the right end of the specimen as shown in figure 1b; any variation in the distance from the pivot pin to the minimum section of the specimen would, of course, cause a variation in the bending moment at that section. Consequently, in machining the specimens the holes at this end were used to position it for the transverse cut. In mounting the specimen in the machine, close-fitting screws

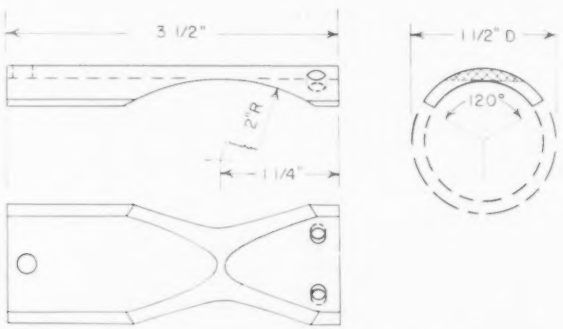

FIGURE 1a. *Significant dimensions of the specimens used for reversed bending fatigue tests.*

The wall thickness of the tubing was ⅛ in. In the view at the right, the minimum section is cross-hatched.

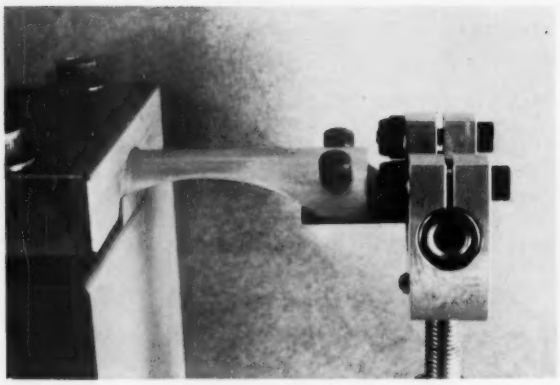

FIGURE 1b. *Photograph showing a specimen mounted in the testing machine.*

The alternating load is applied through the connecting rod and pivot assembly at the right. Full size.

were used in these holes, so that the moment arm was the same for all specimens. In all tests the mean load (directed so that the upper surface of the specimen was in tension) was one-third of the alternating load.

The entire testing machine was enclosed in a cabinet for humidity control. A motion picture camera was mounted above the specimen for taking time lapse exposures during tests of taped specimens, and a telescope passing through the top of the cabinet permitted viewing the test area at about 20× magnification. The humidity control was not automatic, so the actual values of relative humidity for the tests listed as "moist environment" varied from 85 to 95 percent while those for the "dry environment" ranged from less than 5 percent to 9 percent. These measurements were made with a commercial electrical hygrometer.

The experiments described in part 4 involved the application of transparent pressure-sensitive tape to the surface of the specimen. The tape used for these experiments was the ordinary cellophane-base type; one brand was used for all of the principal investigation, but supplementary tests indicated that a number of other brands, and even other types of tape, would make the gas evolution visible in much the same way.

A few preliminary tests were conducted with taped specimens in a low-humidity environment; no bubbling whatever was observed under these conditions. Consequently all of the "taped" tests described in part 4 were run in a moist atmosphere.

An adjustable contactor was used to stop the machine shortly before complete fracture of the specimen. Each of the contacts was a piece of platinum wire; one of these was mechanically and electrically connected to the connecting rod between the eccentric weight and the pivot pin. The other was on an insulated mount whose position relative to the moving contact could be adjusted by a screw from outside the cabinet. A dial indicator permitted reading the separation of the contacts to the nearest 0.0005 in. After a test was started the contactor was raised until it just touched the grounded wire at the bottom of the connecting rod stroke, as indicated by the action of an electronic relay. The contactor was then backed off the desired distance and the relay set to turn off the machine. It had been hoped that this device could be used to indicate the development of a small crack by setting the gap to a small value. However, the length of crack which resulted in cutoff was quite variable and consequently the technique was not useful in this investigation. The contactor did provide a reproducible method of stopping the test just short of fracture; it was set to a gap of 0.030 in., which resulted in a crack through about two-thirds of the section at cutoff. This preserved the original configuration of the specimen so it could be inspected to see if there were any surface features of significance. Also by completing the fracture manually after the specimen had been removed from the machine, the undamaged fracture surface was available for examination. This criterion of failure resulted in values of fatigue life only slightly smaller than would have been obtained at complete fracture.

It was found that considerable care was required in starting the machine to avoid excessive load. A variable autotransformer was used to increase the voltage on the motor very slowly until it pulled into synchronism. If this was not done the motor apparently overshot the synchronous speed, resulting in a few cycles of excessive deflection.

Although a total of three environments were used in this investigation (dry, moist, and taped), the environment was not changed more than once in any one test. Thus a total of nine types of test were conducted, as follows:

(1) Dry environment throughout
(2) Moist, then dry
(3) Dry, then moist
(4) Moist environment throughout
(5) Dry, then taped
(6) Moist, then taped
(7) Taped, then dry
(8) Taped, then moist
(9) Taped throughout.

The greatest emphasis was placed on tests which did not involve the use of tape (types one through four), and these will be discussed in the next section.

2.1. Symbols

S_A—Stress amplitude.
N_1—Number of cycles run in the first environment (in tests in which the environment was changed).
N_F—Number of cycles to failure.
N_R—In the assumed relations such as those in figure 5, the number of cycles to the break in the curve.
N_c—The estimated number of cycles to form a crack 0.1 mm long.
N_X—For two-environment tests, the life to be expected on the basis of a linear interpolation.
N_p—N_F minus N_c

3. Results with Bare Specimens

Conventional S–N curves for specimens tested in both dry and moist environments are shown in figure 2. The points represent logarithmic means of the individual fatigue lives in all cases, the number of replicate tests being indicated on the graph. At 26.5 and 38 ksi** the range of plus and minus one standard deviation is also shown. The average life of specimens tested in the dry environment was from two to three times that in high humidity. This difference corresponds to a difference in stress amplitude of approximately 14 percent throughout the range investigated. Although these environments were artificially produced, they were only slightly more divergent than conditions to be expected in a non-airconditioned laboratory during the course of a year. These results emphasize the possibility that humidity variations may have contributed to the scatter of results in many reported studies of fatigue.

Tests in which the environment was changed during the test were conducted at stress amplitudes of 26.5 and 38 ksi. The machine was stopped during the change, as this required as much as two hours in going from moist to dry atmospheres. The results of these tests are plotted in figures 3 and 4. Graph "A" in each figure shows results for specimens that were run for N_1 cycles in dry atmosphere, then run to failure in a moist environment. The abscissas are the cycle ratios represented by N_1, that is the ratio of the number of cycles run in dry atmosphere to the mean life in that environment. The "B" graphs show similar results for specimens stressed first in a moist environment; the abscissas in these

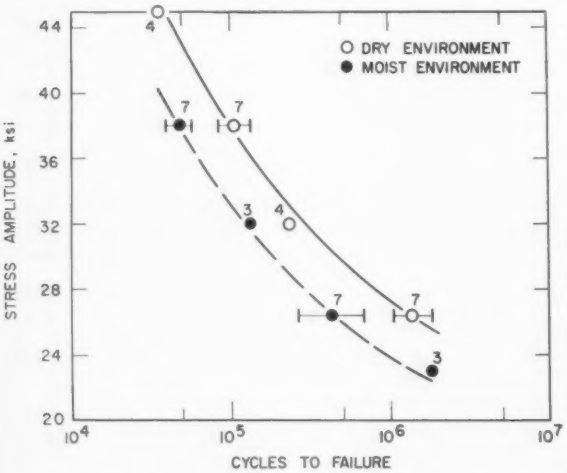

FIGURE 2. *S–N curves for bare specimens in high- and low-humidity environments.*

In all tests the mean tensile stress on the test surface was ½ of the stress amplitude. Numbers adjacent to points indicate the number of replicate tests; horizontal bars show the range of ± one standard deviation.

** Thousands of pounds per square inch.

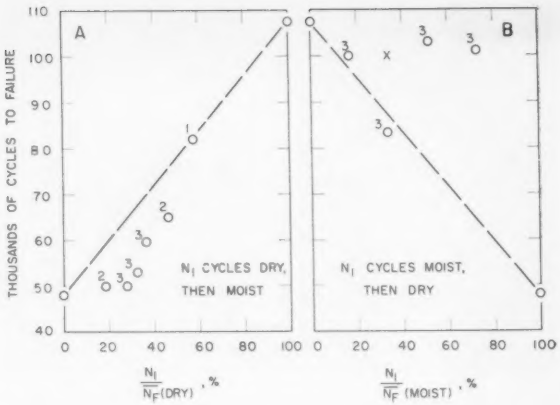

FIGURE 3. *Results of two-environment tests at $S_A = 26.5$ ksi.*

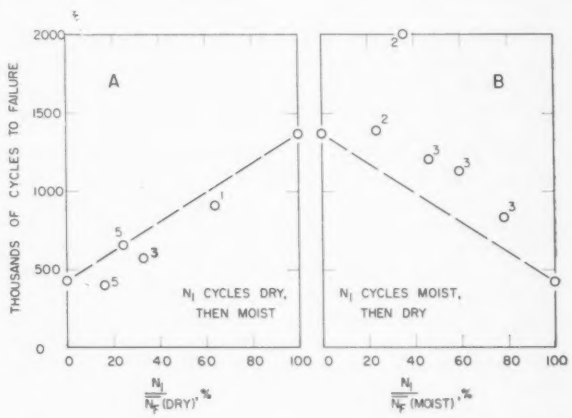

FIGURE 4. *Results of two-environment tests at $S_A = 38$ ksi.*

graphs represent cycle ratios based on the mean life in a high-humidity atmosphere. The end points for the two graphs in each figure are the same, as they are the number of cycles to failure for specimens tested in a single environment.

As in all fatigue testing, the dispersion of the results is troublesome in attempting to determine the true nature of the behavior indicated by the data. In most cases the logarithmic mean values shown in figures 3 and 4 are thought to give reasonably good indications of the true central value; however, the point at 33 percent in graph "B" of figure 4 is probably unduly influenced by one very low result. The mean value of the other two results in this group is shown by the cross, and this appears much more consistent with the rest of the data.

It is apparent from figures 3 and 4 that the fatigue life is not a linear function of the cycle ratio in the first environment; with the exception of the point discussed above, all of the points in the "A" graphs are below the straight line connecting the mean

single-environment values, and all of the points in the "B" graphs are above this line. The divergence is particularly large in tests run first in the moist environment; at a stress amplitude of 38 ksi specimens stressed for more than 70 percent of their expected life in this environment had a mean life only a few percent less than that of specimens tested throughout in a dry atmosphere. Likewise at 26.5 ksi the initial stressing in moist environment seemed to have little effect on the total life; actually the specimen that ran the longest of all those tested at this stress amplitude was one that had been stressed in moist atmosphere for 30 percent of its expected life.

Even though the dispersion of the data was not thought to be excessive, it was large enough to make it difficult to fit trend lines directly. Instead it was considered more informative to make the simplest possible assumptions regarding the behavior of the specimens, then determine if the observed data are consistent with this hypothetical behavior. As the data are clearly not consistent with the linear relation in figures 3 and 4, it might be assumed that the relation is actually two straight lines, the first one horizontal. This would mean that the total life is not influenced by the environment during the early part of the test. Such hypothetical relationships for the tests at 38 ksi are shown in figure 5. If the humidity has no effect during the early part of the test, then the break in the curves must come at the same number of cycles for both environments. This number, indicated by N_R on figure 5, was determined by trying different values until the best fit for both sets of data was found.

The data were compared with the hypothetical relations by plotting the deviations from the linear dependence of N_F on N_1. The life to be expected

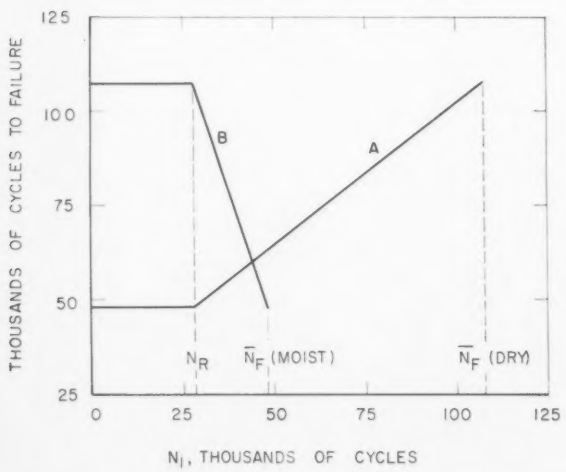

FIGURE 5. *Assumed relationship between* N_1 *and* N_F, *for two-environmental tests at* $S_A = 38$ *ksi.*

Curve A, dry environment first; curve B, moist environment first.

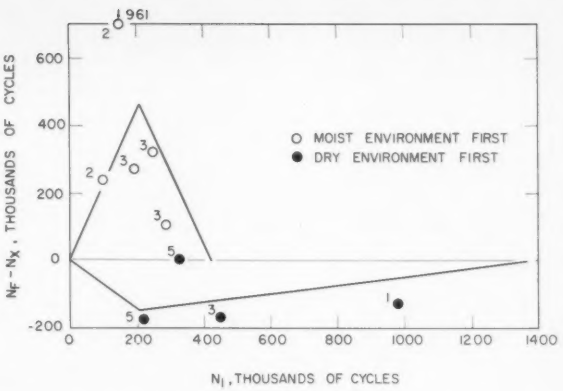

FIGURE 6. *Difference between observed fatigue life and that expected on the basis of a linear dependence on* N_1, *tests at* $S_A = 26.5$ *ksi.*

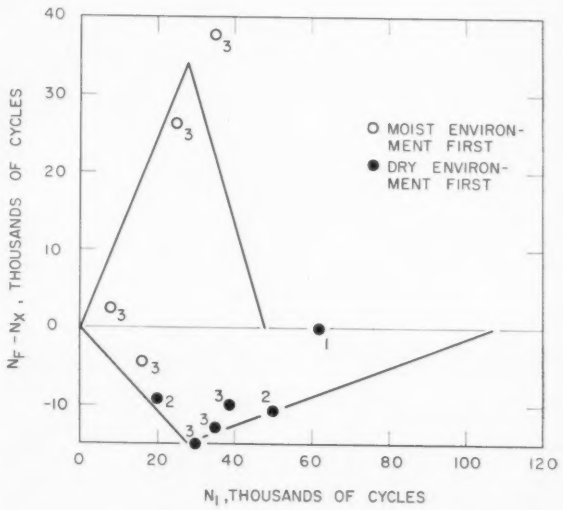

FIGURE 7. *Data similar to figure 6, for tests at* $S_A = 38$ *ksi.*

on the basis of the straight lines in figures 3 and 4 is designated N_x; figures 6 and 7 show the differences between the observed mean N_F and N_x for the same values of N_1. The solid lines on these figures represent the values to be expected on the basis of the assumptions of figure 5, i.e., that the total life is influenced by the environment only after N_R. Although many of the points are far from these lines, the deviations are both positive and negative, and the sums of the deviations in each figure are much less than the deviations from a linear relation. Thus the assumptions shown in figure 5 appear to be consistent with the results; in view of the dispersion of the data it is probably not worthwhile to see if a more complicated hypothesis would provide a better fit. Results of the tests with bare specimens are summarized in table 1.

TABLE 1. *Results of tests with bare specimens*

Stress amplitude	N_R	Atmosphere	N_F
26.5 ksi	210×10^3	Dry	$1{,}369\times10^3$
		Moist	423
38	28	Dry	107.4
		Moist	48.1

4. Results with Taped Specimens

Figure 8 shows enlargements of a few of the time-lapse exposures taken of a taped specimen. Prior to the application of the tape this specimen had been subjected to 900×10^3 cycles at a stress amplitude of 26.5 ksi in a dry environment, but the development of bubbles under the tape is typical of all the specimens photographed. No change is observed during the early part of the test, but once the first bubble appears the gas continues to be evolved until the end of the test. In the test of figure 8 the first bubble appeared at 1217×10^3 cycles and failure occurred at 1455×10^3 cycles.

In the torsion experiments reported in reference [3] it was found that gas evolution started before definite fatigue cracks could be detected either by surface examination or by metallographic examination of the cross section of the specimen. In the current experiments, however, when tests of taped specimens were stopped as soon as gas evolution was observed, it was always possible to see small cracks under the bubbles. If the tests were monitored carefully, the cracks were only a few tenths of a millimeter in length and could be observed only on a metallographic microscope. The first appearance of a bubble on the motion picture film provided a convenient and sensitive means of separating the fatigue life into two stages. It was estimated that the crack length at this point in a test was about 0.1 mm. Consequently, in tests of taped specimens, N_c was taken as the number of cycles at which gas evolution was first observed on the films. In order to obtain values of N_c for the other two environmental conditions (bare specimens), a series of two-environment tests was conducted in which tape was applied or removed.

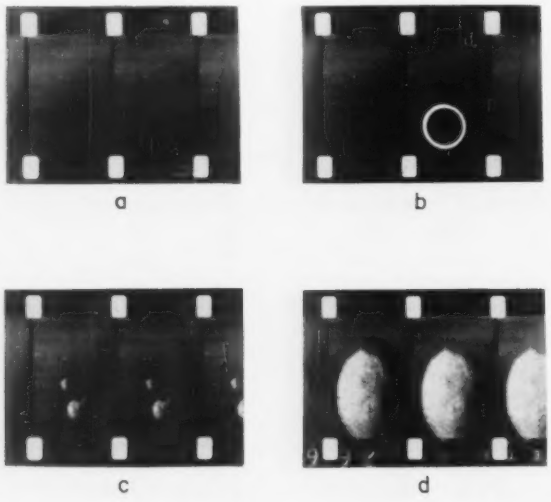

FIGURE 8. *Time lapse exposures taken during test of a taped specimen at $S_A = 26.5$ ksi.*

These pictures show the surface (magnification 1.5×) at the following numbers of cycles:

(a)—1200×10^3 (b)—1280×10^3
(c)—1350 (d)—1455

N_c was determined to be 1217×10^3 cycles, N_F was 1455×10^3.

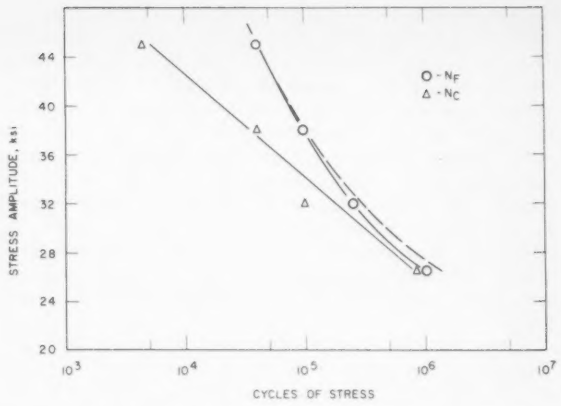

FIGURE 9. *S–N curves for specimens tested with tape on the surface in moist atmosphere.*

The dashed line is the curve from figure 2 for bare specimens in low humidity.

Figure 9 shows the S–N curves for specimens covered with pressure-sensitive tape throughout the test. The open circles represent the logarithmic mean life to failure from tests of three or four specimens at each stress level. The triangular points are median values of N_c, as defined above. The dashed line is taken from figure 2 and represents the data for bare specimens tested in a dry environment. The results with taped specimens differed significantly from this curve only at the low stress end.

Four types of test were conducted in order to estimate the values of N_c for bare specimens; these are listed as types 5 through 8 in part 2 above. In types 5 and 6, the bare specimens were stressed for N_1 cycles, then were taped for the remainder of the test. If N_1 was more than N_c, gas evolution was observed immediately on restarting the testing machine. If N_1 was less than N_c, the time lapse pictures could be used to determine the actual value of N_c for the specimen. A sequential procedure was used for these tests in an effort to assign values of N_1 close to N_c.

The tests of types 7 and 8 (initially taped) were monitored as well as being photographed, and the test was stopped as soon as definite bubbles were seen. The specimen was removed from the machine for cleaning, then replaced and run to failure in either a dry or moist atmosphere.

The purpose of all types of tests involving the use of tape was to provide estimates of N_c for bare specimens to be compared with the values of N_R. The tests with initially bare specimens bracketed N_c, but because of the dispersion of the value from specimen to specimen this was a very inefficient type of determination. The results of tests in which the specimens were initially taped gave values of $N_F - N_c$ (designated N_p) for bare specimens. The difference between these values and the appropriate mean life ($\overline{N}_F$) listed in table 1 gave the second estimate of N_c for each condition. Both of these determinations involve some approximations that cannot be rigorously justified, so the values given in table 2 must be considered as only semi-quantitative.

TABLE 2. *Results from two-environment tests using tape*

Stress amplitude	Atmosphere	N_c[1]	N_p	N_c[2]
26.5 ksi	Dry	1,100×10³	310×10³	1,060×10³
26.5	Moist	200	120	300
38	Dry	37	85	22
38	Moist	20	25	23

[1] From tests with initially bare specimens.
[2] $N_c = \overline{N}_F - N_p$.

In attempting to arrive at a "best value" of N_c from the above data, it is not suitable to average the values in columns 3 and 5 of table 2. For example, the number 22 in column 5 is the difference of two much larger numbers, so that its uncertainty is greater than that of the other result for the same conditions. Consideration of such factors leads to the estimates listed in table 3, of the most probable values of N_c. Data from table 1 and from figure 9 are included for comparison.

TABLE 3. *Summary of test results*

Stress amplitude	N_R	Atmosphere	N_c	N_F
26.5 ksi	210×10³	Dry	1,100×10³	1,369×10³
		Moist	250	423
		Taped	850	1,033
38	28	Dry	35	107.4
		Moist	22	48.1
		Taped	40	97.3

Although N_R and N_c are given to two significant figures, it must be remembered that they are based on data that show a large dispersion. It is difficult to conceive of a mechanism that would result in a value of N_R larger than N_c, as shown for one condition, and this is probably not actually the case. On the other hand it is believed that the magnitudes are approximately correct and that, for example, the difference between N_R and N_c in the first line of the table is certainly significant. Thus the data indicate that N_R represents a discontinuity in the fatigue process which is distinct from the discontinuity represented by the development of the first crack.

These results emphasize the magnitude of the influence that water vapor has on the fatigue behavior of this alloy, since the entire effect takes place between N_R and N_F. At 26.5 ksi this portion of the life is five times as long in a dry atmosphere as it is in a moist one, and the ratio is four to one at $S_A = 38$ ksi. Another interesting point brought out by these results is that at a stress amplitude of 38 ksi, the life in low-humidity air of a specimen containing a visible fatigue crack is greater than the total life of a specimen in a moist environment.

5. Discussion

The evolution of gas makes it clear that a chemical reaction is taking place during crack propagation in this aluminum alloy. It was deduced in reference [3] that the gas is hydrogen resulting from a reaction between water and the fresh metal surface exposed during severe local deformation or crack propagation. This conclusion is substantiated by the observation that no gas evolution is observed when the test is conducted in a low-humidity atmosphere.

Other observations made during this investigation provide some further clarification of the conditions under which the gas evolution can be observed by the development of bubbles under transparent pressure-sensitive tape. As mentioned earlier, the bubbles on these bend specimens were always associated with visible cracks whereas in the earlier work on torsion specimens of 5052–H34 alloy gas evolution was observed before cracks could be detected. This suggests that the development of bubbles depends on the rate of gas production; if this rate is low the hydrogen can diffuse out through the tape before the pressure builds up enough to form a bubble. It would be expected that the rate would be affected by the area of fresh metal being exposed and by the supply of moisture available at the metal surface. Apparently the oxide film was ruptured over a greater area before crack formation in the torsion tests of the cold-worked alloy than in the bend tests of the precipitation-hardened material. Likewise, when the supply of water is reduced by running the test in low humidity, the rate of reaction may not be sufficient to result in bubble formation. Thus the point at which the first bubble is observed probably does not represent a discontinuity in the fatigue process but must be interpreted as the point at which the rate of gas evolution reaches a critical value.

On the other hand, the results from two-environment tests of bare specimens indicate that there is a period during the early part of the fatigue process when the humidity of the environment has no effect. As there is a marked effect after this initial period, there appears to be a definite point where the nature of the surface is changed so that a reaction with the environment can take place. The data of table 3 indicate that this point is significantly earlier in the fatigue life than the start of a detectable crack, at least for specimens run in a dry environment. At both stress levels the values of N_R and N_c for the moist environment are nearly equal, while for the dry tests there is a large difference in the two values at 26.5 ksi, and the difference at 38 ksi is probably

significant. These results suggest that the greatest effect of the reaction with water may occur between N_R and N_c; in moist environment a crack forms very soon after N_R whereas this process takes much longer under low-humidity conditions.

The data of figure 9 show that the tape limits the access of water to the surface of the metal to such an extent that the fatigue behavior is nearly the same as that of bare specimens in a dry environment. The evolution of gas under the tape shows that some moisture is reaching the surface, so the results of figure 9 indicate that the damaging effect of moisture depends on a fairly high rate of reaction. This is also shown by the fact that the S–N curve for taped specimens coincides with that for dry specimens at the high-stress end, but is significantly lower at the lower stress amplitudes where more time is available for water to diffuse through the tape.

The results of this investigation appear to be consistent with the view that the humidity starts to affect the fatigue behavior when the deformation becomes localized, thus breaking the oxide film. During the early part of the fatigue life the deformation is apparently sufficiently uniform so that the film remains intact and no reaction with the environment occurs. Once the film is ruptured, cracks develop rapidly if moisture is available, much more slowly if the supply is limited. The reason for this effect is not clear, but it apparently involves the oxidation of the aluminum with the liberation of hydrogen. One possibility that has been suggested [5] is that if the fresh surface formed during slip in one direction is oxidized, reverse slip cannot occur on the same plane, so the damage from repeated slip is cumulative. If the freshly formed surface is not oxidized, the slip can be reversed on the same plane, thus canceling much of the effect of the forward slip.

6. Miscellaneous Observations

A number of observations that were not related to the primary purpose of the investigation are considered to be of some general interest.

6.1. Amount of Shear Plane Cracking

The fracture surfaces of all specimens were examined after testing. As expected, the initial plane of the cracks appeared to make an angle of approximately 45° with the stress direction, but at a later stage the fracture surface was generally perpendicular to this direction. All of the fractures were irregular, but there seemed to be a definite influence of stress amplitude and environment on the amount of shear plane cracking. As shown in figure 10, the specimens tested at high stress amplitudes and in dry atmospheres were apt to have a large area of shear plane fracture, while in those tested at low stress or high humidity the shear areas were found only close to the origin. (The section shown in figure 10b did not pass close enough to the origin to intersect any such areas.) These

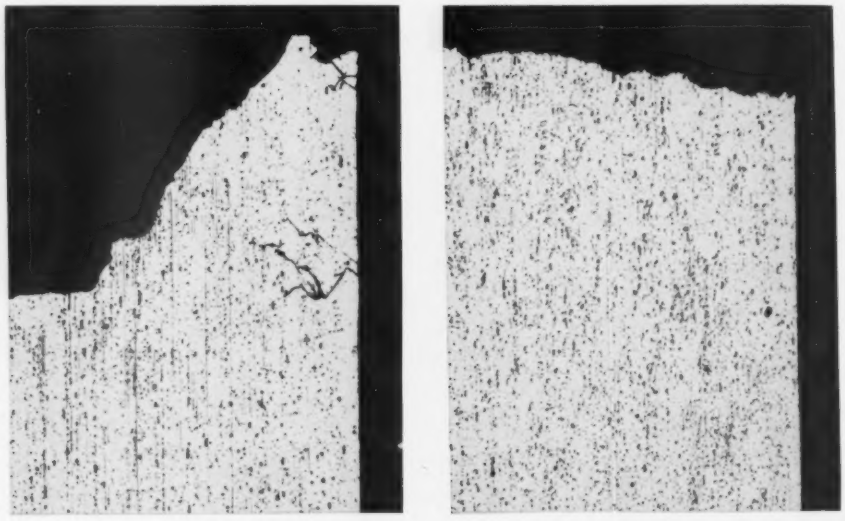

FIGURE 10. *Cross sections of fractured specimens intersecting the fracture (top) and the upper surface (right).* × 50.

a. S_A=45 ksi, tape on surface throughout test.
b. S_A=22 ksi, moist environment.

results are contrary to those reported by Forsyth, Stubbington, and Clark [6]; undoubtedly there are other factors, such as mean load, that have an influence.

6.2. Color on Fracture Surface

With many of the specimens, it was observed that certain areas of the fracture surface produce bright colors when obliquely illuminated with a concentrated light source. By mounting the fracture surfaces in the fractographic specimen mount described in reference [7], the colored areas could be observed at 50 to 150 × on a metallograph. The colors appeared brightest when the specimen was illuminated directly (rather than through the vertical illuminator) with an angle of about 45° between the incident light and the axis of the microscope. The individual areas showing color were not more than a few tenths of a millimeter in extent, but in some parts of the fracture a considerable proportion of the total area was made up of these colored spots. In all cases the greatest amount of color was observed in the portion of the fracture where the crack had propagated rapidly. No color was observed on the static portion of the fracture nor on specimens that had been broken in low humidity at relatively low stress levels (conditions resulting in slow crack propagation).

The colors appeared to be spectrum colors rather than subtractive colors such as those observed due to interference films. Changing the angle between the surface and the direction of viewing resulted in a change in the observed color. When the color-producing areas were examined at higher magnification with vertical illumination, they were always found to contain well-defined striations on the surface. This suggested that the observed colors may be due to diffraction from these striated areas.

Replicas were made of a fracture surface that showed colored areas, and the electron micrographs from these replicas (fig. 11) made it evident that the striations are sufficiently well defined to act as a diffraction grating. The striation spacings measured on several micrographs ranged from 0.1 to 1.3μ. As spacings in this range are consistent with low-order diffraction of visible light, this is probably the correct explanation for the observed color.

There is considerable current interest in the topography of fatigue fracture surfaces, as evidenced, for example, by the excellent investigations of Forsyth and others at the Royal Aircraft Establishment [8]. It appears that the diffraction grating effect might provide a method of measuring striation spacings that could be used for areas that are not accessible for direct observation at high magnifications.

6.3. Usefulness of the Gas Evolution Phenomenon in Fatigue Investigations

The time lapse motion pictures of taped specimens that were taken during this investigation have suggested a number of ways in which the phenomenon of gas evolution might be of use in fatigue studies. The bubble formation under the tape provides an extremely convenient and sensitive crack detection device. As such it has the great advantage that it is easily photographed; this permits both accurate location of the crack and accurate determination of the number of cycles at which the first bubble formed. It appears that these capabilities should be of value, for example, in statistical studies where it is desirable to know the actual stress at the point

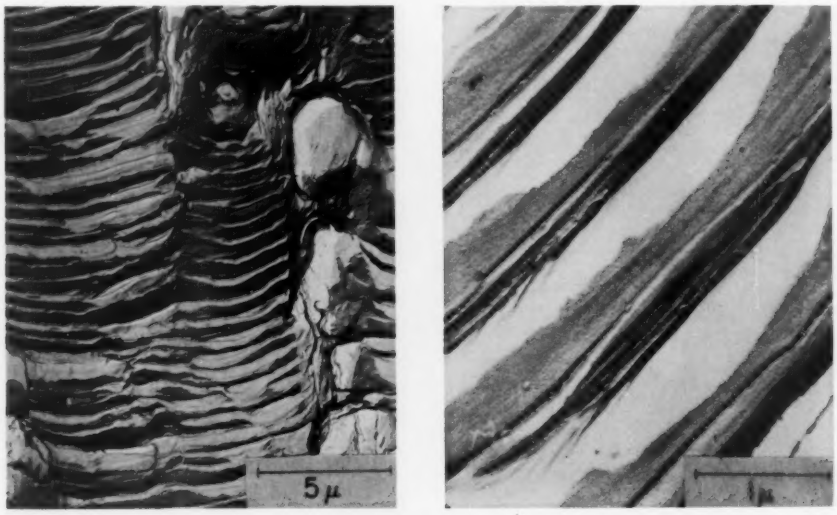

FIGURE 11. *Typical electron micrographs of a fractured surface on which colored areas were observed.*

of crack initiation, or in the many cases when it is helpful to separate the fatigue life into periods of crack initiation and crack propagation.

7. Conclusions

Results of reversed bending fatigue tests on specimens of 6061–T6 aluminum alloy appear to justify the following conclusions:

1. The fatigue life in an environment of about 5 percent relative humidity was two to three times as long as that in high humidity. This difference corresponds to a difference in stress amplitude of about 14 percent throughout the range investigated.

2. The effect of humidity on the number of cycles to failure was much more pronounced during the latter part of the test than during the initial portion.

3. The data are consistent with the view that there was an initial period during which the humidity had no effect on the fatigue behavior of this alloy.

4. The portion of the test during which the humidity had no effect was significantly shorter than the number of cycles required to form a detectable crack in a low humidity environment. In a moist atmosphere cracks apparently developed very soon after this initial period.

5. At a stress amplitude of 38 ksi, the mean life of specimens containing a small fatigue crack, tested in a dry environment, was greater than the total life of specimens tested in a moist atmosphere.

6. Gas evolution under pressure-sensitive tape was observed only after visible fatigue cracks were present.

7. The development of bubbles under transparent tape provided a convenient and sensitive method of detecting small cracks.

8. No gas evolution was observed when the test was conducted in a low-humidity environment.

9. The extent of shear plane cracking increased with increasing stress amplitude and with decreasing humidity.

10. The results seem to be consistent with the view that during the early part of the fatigue process the deformation is fairly uniform, so that the local strain is nowhere sufficient to break the oxide film. As stressing proceeds, the deformation becomes localized, breaking the film so that the fresh metal surface is exposed to the environment.

11. The striations on some of the fracture surfaces were sufficiently pronounced to produce bright colors by diffraction.

There does not appear to be any reason to believe that the results of this investigation are unique to the alloy investigated; it is probable that they are typical of age-hardened aluminum alloys in general.

8. References

[1] H. W. Liu and H. T. Corten, Fatigue damage under varying stress amplitudes, NASA TN D–647, Nov. 1960.

[2] T. Broom and A. Nicholson, Atmospheric corrosion-fatigue of age-hardened aluminum alloys, J. Inst. Metals **89**, 183, 1961.

[3] W. L. Holshouser and J. A. Bennett, Gas evolution from metal surfaces during fatigue stressing, Proc. ASTM **62**, 683, 1962.

[4] J. A. Bennett and J. G. Weinberg, Fatigue notch sensitivity of some aluminum alloys, J. Res. NBS **52**, 235, 1954, RP2495.

[5] N. J. Wadsworth, Effect of environment on metal fatigue, Internal Stresses and Fatigue in Metals, p. 382, Elsevier Publ. Co., 1959.

[6] P. J. E. Forsyth, C. A. Stubbington, and D. Clark, Cleavage facets observed on fatigue-fracture surfaces in an aluminum alloy, J. Inst. Metals **90**, 238, Feb. 1962.

[7] D. B. Ballard and J. A. Bennett, A magnetic specimen mount for fractography, Metal Progr. **74**, 114, Nov. 1954.

[8] P. J. E. Forsyth and C. A. Stubbington, Some observations on the initiation and growth of fatigue cracks in an Aluminum-7.5 zinc-2.5 magnesium alloy, Royal Aircraft Establishment Tech. Note No. Met-Phys 344, July 1962.

(Paper 68C2–155)

JOURNAL OF RESEARCH of the National Bureau of Standards—C. Engineering and Instrumentation
Vol. 68C, No. 2, April-June 1964

The Theory of a Stable High-Speed Externally Pressurized Gas-Lubricated Bearing

H. Sixsmith and W. A. Wilson

(January 15, 1964)

Externally pressurized gas-lubricated bearings have been used successfully to support the shaft of a miniature, high-speed expansion turbine. The bearings incorporate stabilizing cavities to suppress whirl at high speeds. The theory of the bearing design is presented in detail.

1. Introduction

In the field of gas liquefaction and low temperature refrigeration, small high-speed expansion turbines are often employed as the source of refrigeration. In the smaller sizes of machines however, the life and speed of conventional bearings are limited, and consequently a lower limit is set to the practical size of such machines. This limitation may be alleviated by the use of gas-lubricated bearings to support the shaft. The bearings may be lubricated with process gas, thus eliminating the risk of contamination with oil. Since there is no solid friction, there should be no wear and consequently the life of the bearings should be of indefinite duration.

In the operation of a gas-lubricated bearing, the surface of the shaft must never touch the surface of the bearing, since at the high-surface speeds usually employed, such contact may result in seizure and the consequent destruction of the bearing, Under normal operating conditions the shaft should be supported by forces due to pressure in the gas film between the shaft and the bearing and these forces must be such that the shaft is maintained in a position of stable equilibrium.

In certain types of gas-lubricated bearings, a form of instability known as whirl is sometimes observed, particularly at high speeds of operation. If the speed of the shaft is increased above a critical value, the center of the shaft orbits about the center of the bearing at a speed approximately one-half the speed of the shaft—commonly known as half-speed whirl.

Whirl may be stable or unstable: Stable whirl is characterized by the center of the shaft moving in a closed orbit about its former position of equilibrium. This is illustrated in figure 1. Unstable whirl (fig. 2) is characterized by the center of the shaft moving along a spiral orbit of increasing amplitude. The extent of the increase in amplitude is, of course, limited to the extent of the radial clearance between the shaft and the bearing.

The bearing described below has been specially designed to ensure stability even at the highest speeds of operation with helium gas as the pressurizing medium. The theory of this bearing was presented at the First International Symposium on Gas Lubricated Bearings [Sixsmith, 1959b]. In the present paper, the theory has been extended and applied to the design of the bearings of a helium-expansion turbine [Birmingham, Sixsmith, Wilson, 1962]. The

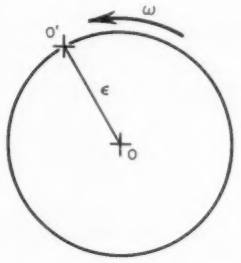

FIGURE 1. *Whirl: constant amplitude.*

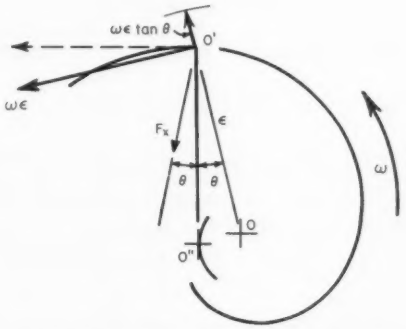

FIGURE 2. *Whirl: increasing amplitude.*

theoretical approach used in this particular design and construction is outlined in the following detailed analysis.

2. Shaft Whirl

In the diagram shown in figure 2, it is assumed that the shaft is vertical so that the only forces acting on the shaft are those due to pressure in the surrounding gas. At a given instant of time, the centers of the bearing and the shaft are situated at O and O'. The radial displacement $O\,O'$ is represented by ϵ. The shaft is moving to the left along a spiral orbit. The resultant of all the forces due to gas pressure is represented by the force vector $\mathbf{F_X}$. The instant center of the orbit of O' is situated at O''. The line $O'\,O''$ bisects the angle between $\mathbf{F_X}$ and the radius $O'\,O$.

It will be assumed that, over a restricted range, the force $\mathbf{F_X}$ varies directly as the radius $O\,O'$, and, hence, behaves like a spring. The force $\mathbf{F_X}$ may be resolved into three components.

$$\mathbf{F_X} \cos^2 \theta = Y(O\,O')$$

which pulls the shaft toward the bearing center,

$$\mathbf{F_X} \sin \theta$$

which accelerates the shaft center along the orbit, and a component

$$\mathbf{F_X} \cos \theta \sin \theta$$

which provides the energy required to stretch the "spring".

The angular velocity ω of O' about O is given by the equation

$$m\omega^2(O\,O') = Y(O\,O') = Y\epsilon$$

or

$$\omega = \sqrt{\frac{Y}{m}}$$

where m is the effective mass of the shaft in the plane of the bearing.

The linear velocity $\omega(O''\,O')$ of the center of the shaft may be resolved into a tangential component

$$\omega(O''\,O') \cos \theta = \omega\epsilon$$

and a radial component

$$\omega(O''\,O') \sin \theta = \omega\epsilon \tan \theta.$$

Thus the line of centers may be regarded as rotating about the center O with an angular velocity ω, while the radial distance ϵ expands as it rotates. The rate of expansion is given by the equation

$$\epsilon = \epsilon_0 e^{\omega t \tan \theta}$$

where ϵ_0 is the value of the eccentricity when $t=0$. Thus if the direction of the resultant force lies ahead of the line of centers (θ positive), the diagram expands exponentially with time; conversely if the direction of the resultant force lies behind the line of centers (θ negative) as shown in figure 3, the diagram shrinks in toward the origin and the bearing should be stable, even though the force $\mathbf{F_X}$ may be quite small.

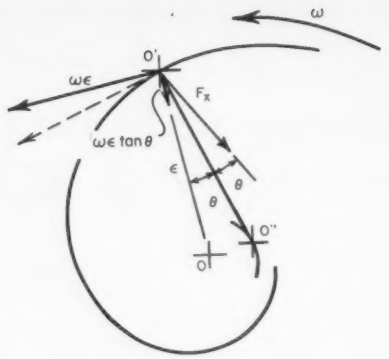

FIGURE 3. *Whirl: decreasing amplitude.*

In practice, the forces due to the film of gas may be far from linear, and at a certain speed of the shaft, if the eccentricity is increased from zero, the sign of the angle θ may change from positive to negative at some critical value of the eccentricity. Under these conditions the diagram should expand asymptotically toward the critical value of the eccentricity and whirling of stable amplitude should occur. This is often observed in practice.

3. Fluent Film Lubrication

The action of a simple sleeve bearing is illustrated in figure 4. A shaft of radius r is surrounded by a sleeve of radius $r+\delta$, the interspace being filled with

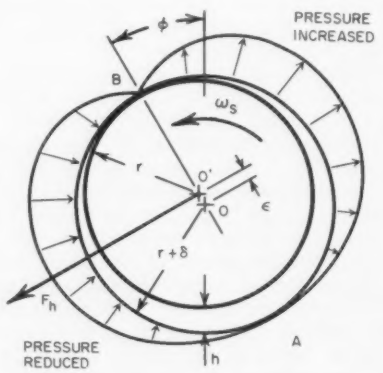

FIGURE 4. *Hydrodynamic pressure distribution.*

a continuous film of lubricant. The center of the shaft O' is displaced from the center O of the sleeve by a small distance ϵ. If the shaft rotates counterclockwise, the film of lubricant is carried into a converging channel on the upper right-hand side of the diagram, and out of a diverging channel on the lower left-hand side of the diagram. Thus the pressure is increased on the upper right-hand side and reduced on the lower left-hand side. The resultant force due to the pressure distribution is at right angles to the eccentricity. This is true, however, only for very small values of the eccentricity where compressibility effects can be neglected; at larger values of the eccentricity, compressibility effects introduce an asymmetry and a component of force directed toward the center of the bearing is generated.

Suppose the eccentric displacement of the shaft from the center of the bearing is maintained at a fixed value by means of a short link free to rotate about O. The forces exerted by the film of gas on the shaft will cause the shaft to whirl about the center O. The whirling velocity ω will be the velocity at which the gas film is carried into the convergent channel, i.e., $\frac{\omega_s}{2}$ where ω_s is the angular velocity of rotation of the shaft.

Thus

$$\omega=\frac{\omega_s}{2}. \tag{1}$$

This phenomenon which is known as "half-speed whirl" is often encountered in the bearings of high-speed spindles, particularly under conditions of light loading.

If the shaft is of mass m, then there will be a centrifugal force $m\omega^2\epsilon$ due to the whirling which acts in the direction of the eccentricity. The pressure in the film of lubricant can only exert forces at right angles to this direction, and if half-speed whirl is occurring, this pressure is zero; consequently, if the short link is removed, the shaft will move outward along a spiral orbit until it comes into contact with the sleeve. As it moves out, however, compressibility and other effects cause the pressure distribution to become asymmetrical. Under these conditions, the new pressure distribution provides a force which can be resolved into a tangential component and an inwardly directed radial component. In practical bearings, small deviations from perfection, such as variations in the film thickness, may introduce such a radial component even when the shaft is at the center of the bearing. At moderate speeds this radial component may be sufficient to balance the centrifugal force due to whirl.

As the speed is increased, however, the radial component of the force due to the film increases as the first power of the speed, while the centrifugal force due to whirl increases as the square of the speed. Thus it is evident that at some critical speed the centrifugal force should become equal to the radial restoring force, and at this speed the shaft should become unstable. This phenomenon is often observed in practice.

In a perfectly constructed bearing, however, it is evident that a whirl of small amplitude should commence even at a very low shaft speed. This prediction has been verified experimentally by Boeker and Sternlicht [1956].

The tangential force F_H which is generated in a bearing of radius r, of radial clearance δ and of length L, is given by the equation

$$F_H=\frac{12\pi\mu r^3 L\epsilon}{\delta^3}\frac{2}{(2+n^2)(1-n^2)^{1/2}}\left(\frac{\omega_s}{2}-\omega\right)f\left(\frac{L}{r},n\right) \tag{2}$$

where

μ is the viscosity of the gas in lb-sec/in.^{2}
ϵ is the eccentricity in inches
n is the eccentricity ratio
ω_s is the rotational velocity
ω is the angular velocity of whirl and
$f\left(\frac{L}{r},n\right)$ is the end leakage factor which depends on $\frac{L}{r}$ and n.

The first, second, and fourth terms on the right-hand side of eq (2) are taken from a paper by Ford, Harris, and Pantall [1957]. The third term, according to Barwell [1956], is introduced in order to account for the effects of whirl. Equation (2) holds only where compressibility effects can be neglected so that the pressure distribution is symmetrical about the line of centers.

The value of the end leakage factor has been determined experimentally by Ford, Harris, and Pantall [1957]. According to the curves in figure 18 of their paper, the value of the end leakage factor in bearings whose length is less than twice the diameter is approximately

$$f\left(\frac{L}{r}\right)\approx\frac{1}{6.0}\frac{L}{r}, \tag{3}$$

and for small values of n, the leakage factor is independent of the eccentricity ratio.

Thus, at small values of the eccentricity ratio, the tangential force in a sleeve bearing whose length is less than twice the diameter is given approximately by the equation

$$F_H=E_H\epsilon\approx\frac{2\pi\mu r^2L^2\epsilon}{\delta^3}\left(\frac{\omega_s}{2}-\omega\right) \tag{4}$$

where E_H is the tangential "spring" modulus.

Equation (4) may be written

$$F_H=E_H\epsilon\approx\frac{\pi\mu r^2L^2\omega_s\epsilon}{\delta^3}\left(1-\frac{2\omega}{\omega_s}\right) \tag{5}$$

The force F_H can be either positive or negative depending on the value of ω. In fact, $F_H=0$ when

ω is exactly equal to $\frac{\omega_s}{2}$. There is no pressure acting on the shaft due to the gas film under this condition. The force F_H acts at right angles to the displacement ϵ, and when $\omega < \frac{\omega_s}{2}$, then F_H acts in the direction of shaft rotation and whirl is accelerated; conversely, when $\omega > \frac{\omega_s}{2}$, then F_H acts in the opposite direction to shaft rotation and whirl is retarded.

An appreciation of the magnitude of the tangential force in a simple sleeve bearing at an eccentricity ϵ may be obtained from the following example.

Example 1

Radius of shaft	0.437 in.
Radial clearance	1.50×10^{-3} in.
Length of bearing	0.281 in.
Viscosity of gas	2.97×10^{-9} lb-sec/in.^{2}
Angular velocity of shaft	1.88×10^4 radians/s
Angular velocity of whirl	Zero

$$E_H=\frac{3.14\times2.97\times10^{-9}\times(0.437)^2\times(0.281)^2\times1.88\times10^4}{(1.5\times10^{-3})^3} \tag{6}$$

$$E_H=784 \text{ lb/in.} \tag{7}$$

Thus at an eccentricity of 0.000393 in. (0.001 cm) the tangential force is approximately 0.308 lb weight.

It is evident that in order to insure stability at finite speeds of the shaft, the bearing must be designed so that a radial restoring (centering) force F_R is generated. If this force is proportional to the eccentricity, it behaves like a spring, and it may be expressed as

$$Y\epsilon=F_R \tag{8}$$

where Y is the modulus of the "spring" and ϵ is the eccentricity. An appreciation of the radial spring modulus required in one of the bearings of the miniature turbine may be obtained from the following example.

Example 2

The effective mass of the shaft in the plane of the most heavily loaded bearing is 0.775 lb, and the designed rotational speed is 3,000 rps. The corresponding half-speed whirl velocity is 1,500 rps=9430 radians/s. Inserting these values in the equation $Y\epsilon=m\omega^2\epsilon$ we get

$$Y=0.775\times9430^2/32.3\times12 \tag{9}$$

$$=178{,}200 \text{ lb/in.} \tag{10}$$

At an eccentricity of 0.00039 in., the centrifugal force would be approximately 69.5 lb weight.

4. External Pressurization

The necessary restoring force may be generated by means of external pressurization. The sleeve is provided with a number of equally spaced injector holes, as shown in figure 5. Compressed gas is supplied to the injector holes and flows radially outward in the clearance space between the shaft and the sleeve. The shaft is found to float centrally in the sleeve, a well-known effect.

The reason for this effect becomes evident from an examination of a plane circular bearing as shown in the insert of figure 6. In this figure the relationship between the mean pressure between the plates and the plate separation is shown for various supply pressures. The graphs in figure 6 show the variation of pressure with the separation of the plates for plates of $\frac{3}{8}$ in. diameter. In order to find the corresponding variation of pressure for plates of any diameter, the scaling relationship $h^2 \sim D$ is used in conjunction with a constant orifice to pad diameter ratio. Accordingly, the graphs shown in figure 7 are drawn for pads $\frac{3}{8}$ in. diameter and a plate separation of 0.00165 in., which corresponds to a plate separation of 0.0015 in. with plates $\frac{5}{16}$ in. diameter.

As shown in figure 5, the pads in this bearing are not circular but have a rectangular configuration, as shown. It will be assumed that each pad is equivalent to a circular pad $\frac{5}{16}$ in. diameter. The mean pressure in the clearance space between a pair of diametrically opposed pads [Sixsmith, Wilson, Birmingham, 1961] is shown in figure 7. Curves a and b show the variation of mean pressure with clearance on the right-hand and left-hand sides of the shaft. Curve c shows the variation of differential pressure with the eccentric displacement of the shaft. Over

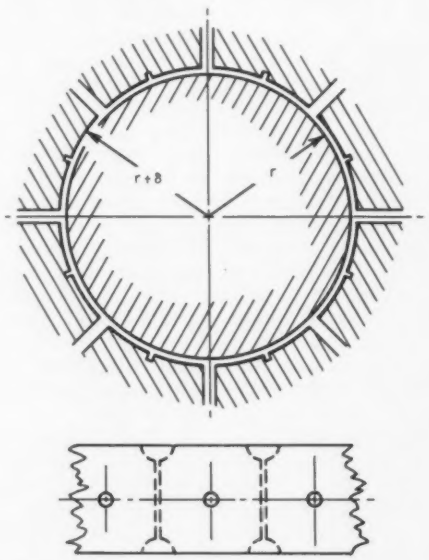

FIGURE 5. *Conventional gas-bearing arrangement.*

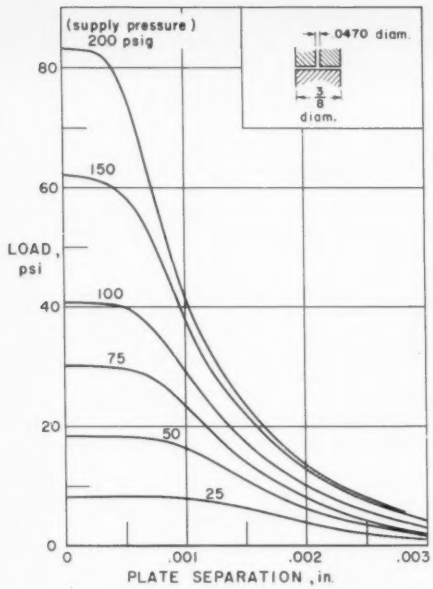

FIGURE 6. *Load versus plate separation curve.*

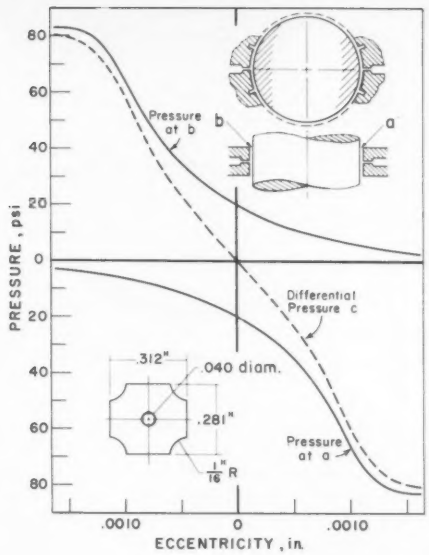

FIGURE 7. *Mean pressure on gas-bearing pads.*

a restricted range the differential pressure (curve c) may be assumed to be linear, thus the corresponding restoring force is also linear, and is directly proportional to the displacement.

If the direction of the radial displacement makes an angle γ with a diameter through the center of a pair of diametrically opposed pads, the component of the deflection with respect to the pads is $\epsilon \cos \gamma$. Similarly, the component of the force generated by the pair of diametrically opposed pads in the direction of the displacement is also proportional to $\cos \gamma$. Thus the total restoring force along any radius is given by

$$Y\epsilon = \frac{1}{2}\frac{\partial P}{\partial \epsilon} A_1 \epsilon \sum [\cos^2 \gamma]_{2\pi}^{0}$$

or

$$Y\epsilon = \frac{N}{4} A_1 \frac{\partial P}{\partial \epsilon} \epsilon \qquad (11)$$

where Y is the "spring" modulus of the gas film, N is the number of pads, A_1 is the area of a pad, and $\frac{1}{2}\frac{\partial P}{\partial \epsilon}$ is the differential pressure due to a single pad as shown in figure 7.

Example 3.

In the present bearing there are eight pads, and for this particular number of pads,

$$\sum [\cos^2 \gamma]_{2\pi}^{0} = 4 \qquad (12)$$

and (11) becomes

$$Y\epsilon = 2A_1 \frac{\partial P}{\partial \epsilon} \epsilon. \qquad (13)$$

The effective area A_1 of a pad is 0.076 in.^{2}, and the slope of curve c at 200 psig supply pressure is 44,000 lb/in.^{2}/ in. Putting these values in (13) we obtain the value of Y. Thus

$$Y = 2 \times 0.076 \times 44{,}000$$
$$= 6{,}700 \text{ lb/in.} \qquad (14)$$

At an eccentric displacement of 0.00039 in., the radial restoring force is 2.61 lb. This is less than the corresponding centrifugal force (example 2) by a factor of 27. Thus it is evident that the radial restoring force, although quite large, is insufficient to prevent the shaft from spiralling outward until it touches the bearing. It is then necessary to devise a method whereby the centrifugal force can be reduced to a value below the available radial restoring force in order to obtain a stable bearing. This can be accomplished by reducing the shaft whirl speed. The method used to reduce whirl speed is presented in sec. 6.

5. Analysis of Turbine Rotor Instabilty

In an early design of a turbine [Sixsmith, 1959a] in which the turbine was mounted on a flexible shaft, it was discovered that a hydrodynamic exciting-force can be generated by the turbine rotor. At a certain critical pressure of the gas supply, a whirling of the shaft would commence. The shaft could be made to whirl even when it was prevented from rotating. In order to suppress the whirl it was necessary to provide damping in the form of oil-filled dash-pots.

720-591—64——3

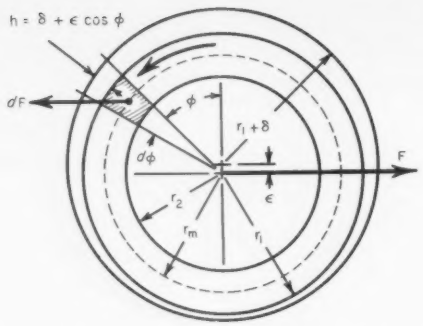

FIGURE 8. *Force distribution on turbine rotor.*

An explanation of this phenomenon is as follows. The effect appears to be due to forces which are generated by the variation of blade-tip leakage with rotor eccentricity. Consider the turbine rotor shown in figure 8. If the rotor is displaced downwards as shown, the tip leakage is reduced around the lower half of the rotor and correspondingly increased around the upper half. Around the lower half of the rotor the tip leakage is less, hence an increased thrust is developed on the blades. This force is to the right for counterclockwise rotation. Around the top half, tip leakage increases and the thrust on the blades is reduced. This can also be regarded as an added component of force to the right. Consequently there is a net force to the right acting on the rotor as a whole. This force is at right angles to the displacement, and therefore, it is in the same direction as the hydrodynamic force which is generated in a simple sleeve bearing.

An estimate of its magnitude may be made if we assume that the loss of torque due to tip leakage is directly proportional to the tip clearance, i.e.,

$$dT=\frac{Td\phi}{2\pi}\left[1-\frac{2\pi r_1 h v_1}{\pi v_2(r_1^2-r_2^2)}\right] \tag{15}$$

where

dT=element of torque acting on the blades between ϕ and $\phi+d\phi$
T=total torque acting on the rotor—in. lb
r_1=tip radius—inches
r_2=root radius—inches
h=mean tip clearance between ϕ and $\pi+d\phi$—inches
v_1=axial component of velocity of gas through the tip clearance in./s
v_2=axial component of velocity of gas through the annulus—in./s between r_1 and r_2.

If the rotor is deflected downwards a distance ϵ the tip clearance h at a point which makes an angle ϕ with the direction of the displacement is given by

$$h=\delta+\epsilon\cos\phi. \tag{16}$$

The horizontal force dF to the right which acts on the small segment of blading lying between ϕ and $\phi+d\phi$ is given by

$$dF=\frac{dT}{r_m}\cos\phi$$

where r_m=mean radius of rotor blades. Thus

$$dF=\frac{Td\phi}{2\pi r_m}\left[1-\frac{2\pi r_1 h v_1}{\pi(r_1^2-r_2^2)v_2}\right]\cos\phi.$$

Substituting $(\delta+\epsilon\cos\phi)$ for h we have

$$dF=\frac{Td\phi}{2\pi r_m}\left[1-\frac{2r_1v_1}{(r_1^2-r_2^2)v_2}(\delta+\epsilon\cos\phi)\right]\cos\phi.$$

On integrating between O and 2π, all terms will vanish except the one containing $\cos^2\phi$, thus we have

$$F=\frac{T\epsilon}{2\pi r_m}\times\frac{2r_1v_1}{(r_1^2-r_2^2)v_2}\left(\frac{1}{2}\sin\phi\cos\phi+\frac{1}{2}\phi\right)_0^{2\pi}$$

$$=\frac{T\epsilon r_1v_1}{\pi r_m(r_1^2-r_2^2)v_2}\left(\frac{1}{2}\phi+\frac{1}{4}\sin 2\phi\right)_0^{2\pi}$$

$$=\frac{T\epsilon r_1v_1}{r_m(r_1^2-r_2^2)v_2}$$

which may be written as

$$F=kT\epsilon \tag{17}$$

where

$$k=\frac{r_1v_1}{r_m(r_1^2-r_2^2)v_2}.$$

Thus it appears that the whirl-inducing force is proportional to the product of the torque and the eccentricity, but is independent of tip clearance as long as the assumption that the blade passage efficiency is inversely proportional to tip clearance is valid. Since for a given eccentricity it is proportional to the torque, it is capable of inducing a whirl even when the shaft is prevented from rotating.

In the miniature turbine the value of the torque at 3000 rps and 3 kw of power is 1.406 lb-in. The values of r_1, r_m, and r_2 are 0.436, 0.397, and 0.36 in. Since the blade outlet angle is 30°, the value of $\frac{v_1}{v_2}$ is 2, approximately. Putting these values in (17) we have

$$F=\frac{1.406\times0.436\times2\times\epsilon}{0.397(0.436^2-0.360^2)}$$

or

$$F=51.15\epsilon \text{ lb}. \tag{18}$$

Thus at an eccentricity of 0.00039 in. the tangential force is 0.02 lb weight.

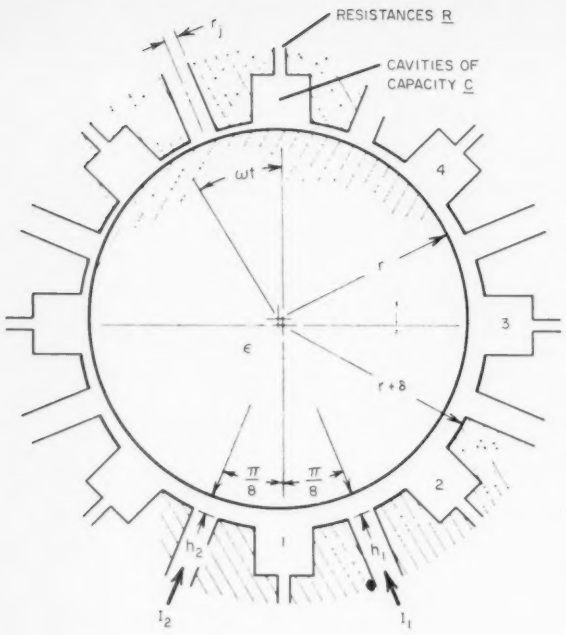

FIGURE 9. *Gas bearing with stabilizing cavities.*

6. The Analysis of a Method of Stabilizing a Gas-Lubricated Bearing

In order to ensure stability, it is necessary to reduce the angular velocity of whirl until the centrifugal force becomes less than the radial restoring force. A reduction in the angular velocity of whirl may be effected if the bearing is designed to generate a force which acts in the opposite direction to the hydrodynamic exciting forces due to the bearing and the turbine rotor.

A bearing designed to produce this stabilizing force is shown in figure 9. In addition to the injector holes, as shown in figure 5, the shaft is surrounded by a number of pneumatic phase shift networks which are spaced midway between the injector holes. Each network consists of a cavity which acts as a pneumatic capacitor and a leak orifice which acts as a pneumatic resistor. A stream of gas flows into each cavity from the adjacent injector holes, and escapes from the cavity via the leak orifice. The pressure in the cavity is determined by the flow rate and the resistance of the orifice. In the event of a whirling of the shaft, the flow of gas into each cavity is modulated, the modulation being in phase with the eccentricity vector. As a consequence of the modulated inflow, the pressure in the cavity is likewise modulated, but by virtue of the finite volume of the cavity, the phase of the pressure is lagging with respect to the phase of the current and the eccentricity. The force on the area of shaft facing the cavity, being in phase with the pressure, is likewise lagging with respect to the current and eccentricity vectors. This force can be resolved into components whose directions are radial and tangential with respect to the eccentricity vector. The tangential component acts in the opposite direction to the hydrodynamic force due to the bearing and the turbine rotor. By suitable design of the bearing, the tangential component of force can be made to exceed the exciting forces so that the net tangential force is opposed to the tangential motion of whirl, and consequently, the whirling motion should be damped out.

The radial component acts in the opposite direction to the centering force due to the injector holes, and therefore it reduces the load carrying capacity of the bearing. This is inherent in the design and cannot be avoided.

As shown in figure 9, a shaft of radius r is surrounded by a sleeve of internal radius $r+\delta$. Gas from eight injector holes each of radius r_j, equally displaced around the circumference of the sleeve, flows into eight cavities each of capacity C. The majority of the gas escapes from each cavity through a leak orifice of resistance R. The remainder escapes at the ends of the bearing, but it will be assumed that this portion is negligible. Each cavity and leak

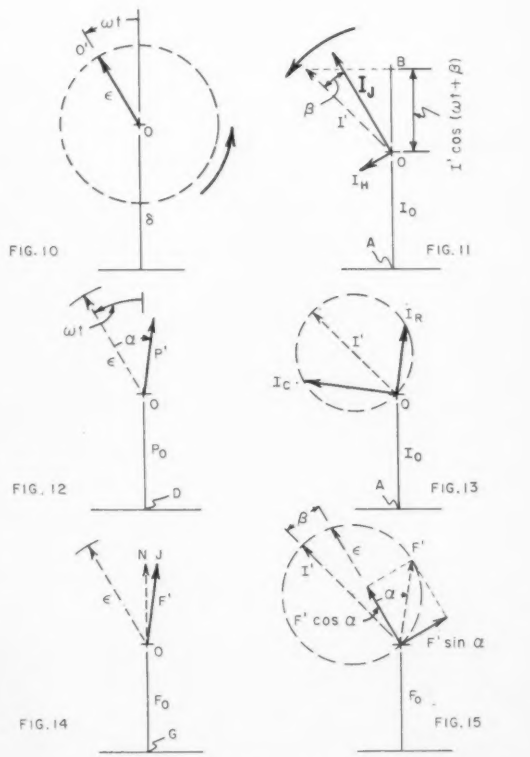

FIGURES 10–15 (inc.) *Vector diagrams illustrating the action of a stabilizing cavity.*

behaves like an electrical resistance-capacity network: the capacity of a cavity being defined by the equation

$$C\frac{\partial P}{\partial t}=V\frac{\partial \rho}{\partial t}=V\frac{\rho}{P}\frac{\partial P}{\partial t}=I_c \text{ lb/s} \tag{19}$$

and the resistance of a leak by

$$\frac{P}{R}=I_L \text{ lb/s} \tag{20}$$

where V is the volume of the cavity, ρ is the density of the gas in the cavity, P is the pressure in the cavity, I_c is the current of gas accumulating in the cavity, and I_L is the current flowing through the leak: t is time.

A cavity receives its gas supply from both of the adjacent injector holes. Suppose now that the shaft is whirling with an eccentricity ϵ and a counterclockwise angular velocity ω. The motion of the center of the shaft may be represented by a complex vector ϵ rotating counterclockwise with the same angular velocity (fig. 10).

Referring again to figure 9, it will be seen that the current of gas I entering cavity 1 will be given by

$$\begin{aligned} I&=1/2I_1+1/2I_2\\ &=\pi r_j v\rho_1(h_1+h_2) \end{aligned} \tag{21}$$

where v is the velocity of the gas at the edges of the injector holes and ρ_1 is its density. The values of the clearance at the injector holes adjacent to cavity 1 are given by

$$h_1=\delta+\epsilon\cos\left(\omega t-\frac{\pi}{N}\right)$$

and

$$h_2=\delta+\epsilon\cos\left(\omega t+\frac{\pi}{N}\right)$$

where N is the number of cavities.

The time t is assumed to be zero when ϵ is pointing vertically downward through the center of cavity 1.

Equation (21) may now be written

$$\begin{aligned} I&=\pi r_j v\rho_1\left\{\delta+\epsilon\cos\left(\omega t-\frac{\pi}{N}\right)+\delta+\epsilon\cos\left(\omega t+\frac{\pi}{N}\right)\right\}\\ &=\pi r_j v\rho_1\left\{2\delta+2\epsilon\cos\omega t\cos\frac{\pi}{N}\right\}. \end{aligned} \tag{22}$$

The current flowing into cavity 1 thus consists of a steady component I_0 which is given by

$$I_0=2\pi r_j v\rho_1\delta \tag{23}$$

and an alternating component I_j which rotates in phase with the eccentricity vector ϵ and whose instantaneous value is given by

$$I_j\cos\omega t=2\pi r_j v\rho_1\epsilon\cos\omega t\cos\frac{\pi}{N}. \tag{24}$$

In the above analysis, the effects of shaft rotation and whirl have been neglected. These effects influence the flow rate into the cavity. Referring to figure 9, it is seen that the clearance between the shaft and the bearing on the right-hand side of the cavity is greater than the clearance on the left-hand side. As a consequence of the rotation of the shaft, more gas is carried out of the cavity on the right-hand side than is carried in on the left-hand side. Thus there is a net flow of gas out of the cavity. An estimate of the value of this component of current may be made if it is assumed that the principle of superposition may be applied; i.e., that the velocity of the gas at any point in the film is the vector sum of the radial velocity from the injector holes and the tangential velocity due to hydrodynamic action.

The instantaneous value of the hydrodynamic component of current I_a is given by

$$\begin{aligned} I_a\sin\omega t&=\frac{\omega_s}{2}L_c r\rho_2(h_2-h_1)\\ &=\frac{\omega_s}{2}L_c r\rho_2\left\{\left[\delta+\epsilon\cos\left(\omega t+\frac{\pi}{N}\right)\right]\right.\\ &\quad\left.-\left[\delta+\epsilon\cos\left(\omega t-\frac{\pi}{N}\right)\right]\right\}\\ &=-\omega_s L_c r\rho_2\epsilon\sin\omega t\sin\frac{\pi}{N} \end{aligned} \tag{25}$$

where I_a is the alternating flow of current, ω_s is the angular speed of the shaft, r is the radius of the shaft, L_c is the effective length of the cavity, and ρ_2 is the density of the gas in the clearance space.

Referring again to figure 9, it is seen that as a consequence of the whirling motion, the shaft is approaching the cavity and therefore the volume of the cavity is decreasing. This may be regarded as a current I_W flowing into the cavity, the volume of the cavity being regarded as constant. The instantaneous value of the current is given by the equation

$$I_W\sin\omega t=2\omega L_c r\rho_2\epsilon\sin\omega t\sin\frac{\pi}{N} \tag{26}$$

where I_W is the alternating flow of current and ω is the angular velocity of whirl.

Thus the resultant current I_H due to the effects of shaft rotation and whirl is given by the equation

$$I_H\sin\omega t=-L_c r\rho_2\epsilon\omega_s\left(1-\frac{2\omega}{\omega_s}\right)\sin\omega t\sin\frac{\pi}{N} \tag{27}$$

This current may be represented by the vector $\mathbf{I_H}$ (fig. 11) which rotates 90° ahead of the eccentricity vector ϵ.

The resultant current flowing into the cavity is represented by the vector $\mathbf{I}'$. It is seen that

$$\mathbf{I}'=I_j \sec \beta. \tag{28}$$

The direct current I_0 flowing into the cavity may be represented by vertical line OA, figure 11, and the instantaneous value of the alternating current by the vertical line OB. This is the projection on a diameter through cavity 1 of the alternating current $\mathbf{I}'$ which rotates ahead of the eccentricity vector ϵ with a phase angle β.

The value of β is given by

$$\tan \beta=\frac{I_H}{I_J}=\frac{L_c r \rho_2 \omega_s}{2\pi r_j v \rho_1}\left(1-\frac{2\omega}{\omega_s}\right)\tan \frac{\pi}{N}. \tag{29}$$

The steady current I_0 flowing through the resistance R generates a pressure given by

$$P_0=\mathbf{I}_0 R. \tag{30}$$

This is represented by the vertical line OD, figure 12.

The alternating current generates an alternating pressure component

$$P'=I'Z=I_j Z \sec \beta=\frac{I_j R \sec \beta}{\sqrt{1+\omega^2 C^2 R^2}}=\frac{I_j R \sec \beta}{\sqrt{1+\tan^2 (\alpha+\beta)}} \tag{31}$$

where Z is the impedance of the resistance-capacity network. With respect to the alternating component of current, the capacity and resistance are effectively in parallel and, consequently, the phase of the pressure lags behind that of the current and the eccentricity. The phase angle α is given by

$$\tan (\alpha+\beta)=\omega RC. \tag{32}$$

The currents due to the alternating pressure P' are represented vectorially in figure 13. The vector $\mathbf{I_R}$ represents the alternating current flowing in the resistance R, and the vector $\mathbf{I_C}$ represents the alternating current flowing in the capacity. The values of $\mathbf{I_R}$ and $\mathbf{I_C}$ are given by the equations

$$\mathbf{I_R}=\frac{P'}{R} \tag{33}$$

and

$$\mathbf{I_c}=P'\omega C=P'\omega V\frac{\rho}{P}. \tag{34}$$

The resultant of these two currents must be equal to and in phase with the alternating current I' flowing into the cavity.

The pressures P_0 and P' acting on the effective[1] area A_2 of the shaft, which forms one wall of the cavity, generate forces

$$F_0=A_2 P_0 \tag{35}$$

and

$$F'=A_2 P'. \tag{36}$$

These forces may be represented by the vertical vector **OG** (fig. 14) and the alternating vector **OJ,** respectively. The alternating vector $\mathbf{F}'$ may be resolved into a component $\mathbf{F}'$ cos α which is in phase with the eccentricity and a component $\mathbf{F}'$ sin α which is lagging 90° behind the eccentricity (fig. 15).

These forces are generated by a single cavity and act along the radius from the center of the shaft through the center of that cavity. With a symmetrical array of cavities, the resultant of the steady forces F_0 will be zero; this, however, is not true of the alternating components.

The resultant force on the shaft at any instant is found by adding vectorially the instantaneous values of the forces due to each of the cavities.

The instantaneous value of the force due to cavity 1 is

$$\mathbf{F}' \cos (\omega t-\alpha). \tag{37}$$

This is the projection of the alternating vector $\mathbf{F}'$ along a diameter through the center of the cavity. At a given instant it is represented in magnitude and direction by the vertical line ON as shown in figure 14.

The polar diagram of the force due to each of the eight cavities is shown in figure 16. At an instant of time t, the vectors numbered 1 to 8 represent the forces due to the corresponding cavities.

The polar diagram represents a field of force rotating with the angular velocity of whirl. This is illustrated in figure 17, which shows the values of the eight forces due to the cavities when t has increased to $t+\Delta t$. These forces can be combined into a resultant which by symmetry will lie along **OJ**. The magnitude of this force may be written as F_s

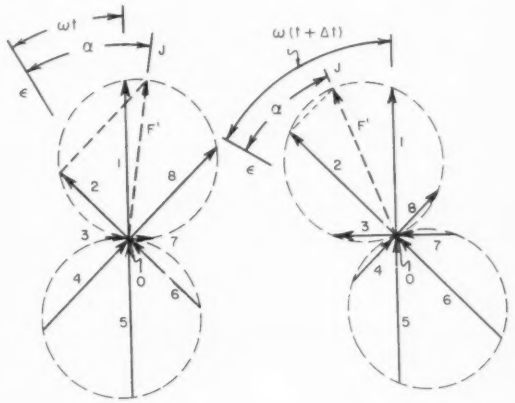

FIG. 16 FIG. 17

FIGURES 16 and 17. *Polar diagrams of force generated by stabilizing cavities.*

[1] Experimental testing has shown A/2 to be a conservative estimate for the value of A_2 as illustrated in figure 20.

and is given by

$$F_S=\frac{N}{2}\mathbf{F}'. \tag{38}$$

Substituting from (36), (31), (29), and (24) this becomes

$$F_S=N\pi A_2 r_j v\rho_1 Z\epsilon \cos\frac{\pi}{N}\sec\beta \tag{39}$$

or

$$F_S=GZ\epsilon \tag{40}$$

where

$$G=N\pi A_2 r_j v\rho_1 \cos\frac{\pi}{N}\sec\beta. \tag{41}$$

G is a constant which depends on the design of the bearing and the speed of the shaft. The alternating vector $\mathbf{GZ}\epsilon$ may be resolved into components $GZ\epsilon$ cos α in phase with the eccentricity vector or $\mathbf{GZ}\epsilon$ sin α lagging 90° behind the eccentricity vector. The component of force $GZ\epsilon$ cos α due to the stabilizing cavities is in the same direction as the centrifugal force due to whirl and in the opposite direction to the centering force due to the injector holes defined in (11). Consequently, the centering force is reduced to $Y\epsilon-GZ\epsilon$ cos α. Whirl can set in at an angular velocity given by

$$m\omega^2\epsilon=Y\epsilon-GZ\epsilon\cos\alpha; \tag{42}$$

i.e.,

$$\omega=\left(\frac{Y-GZ\cos\alpha}{m}\right)^{1/2}. \tag{43}$$

These forces are represented as vectors in figure 18.

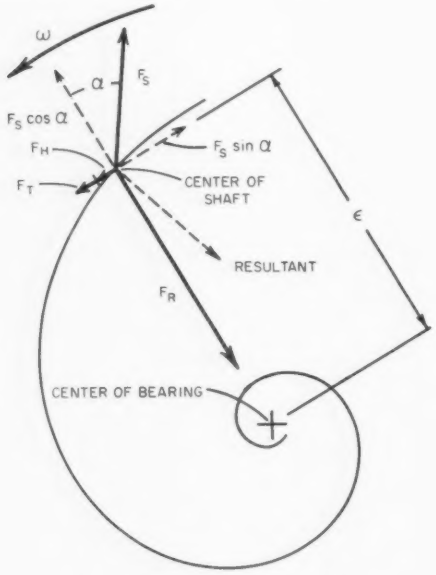

FIGURE 18. *Illustration of forces on shaft.*

The component $GZ\epsilon$ sin α provides a force at right angles to the eccentricity vector and acts in the opposite direction to the forces due to hydrodynamic action or excitation in the bearing and the turbine rotor F (17). This is the damping force which is required to provide stability. Provided it is greater than the sum of the bearing and turbine rotor excitations, the direction of the resultant of all the forces lies behind the line of centers, and any whirl, such as might be excited by an external shock, is attenuated until its amplitude becomes zero.

An estimate of the magnitude of the hydrodynamic force due to the bearing may be made as follows. The bearing is regarded as a simple sleeve bearing in which the shaft rotates with an angular velocity ω_s and a whirl velocity ω. The value of the whirl velocity ω is given by (43). The hydrodynamic force which is generated at an eccentricity ϵ can be calculated with the aid of (5). The force thus calculated may be expressed in the form

$$E_H\epsilon=F_H \tag{44}$$

for small values of the eccentricity ratio ϵ/δ. E_H is a constant whose value depends on the design of the bearing. In the above calculation no account is taken of the disturbance in the flow pattern due to the various holes and slots in the surface of the bearing. These have the effect of reducing the pressures due to hydrodynamic action and therefore the calculated value of the hydrodynamic force $E_H\epsilon$ is an overestimate. Thus it errs on the safe side. The force $E_H\epsilon$ is represented vectorially in figure 18.

The rotor excitation kT is given by (17). This applies however to the force in plane of the rotor; hence, the value must be multiplied by some factor k_1, depending on the overhang, in order to give the force in the plane of the bearing. This force may thus be expressed in the form

$$F_T=k'T\epsilon \tag{45}$$

where

$$k'=k_1k. \tag{46}$$

This force is shown vectorially in figure 18. The term $k'T$ can be regarded as the rotor excitation reduced to the plane of the bearing. Referring to figure 19, it is seen that the excitation due to the rotor is greater in the inner bearing than it is in the outer bearing. For the inner bearing the value of k_1 is given by

$$k_1=\left(\frac{L_5}{L_2+L_4}\right). \tag{47}$$

The stabilizing force $GZ\epsilon$ sin α which is generated by the bearing must be greater than the sum of the two excitations outlined above if the shaft is to be stable.

The condition required for dynamic stability is thus given by

$$GZ\epsilon\sin\alpha>k'T\epsilon+E_H\epsilon. \tag{48}$$

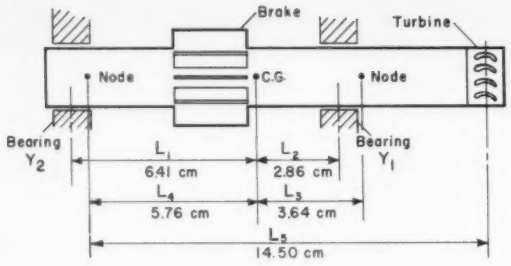

FIGURE 19. *Shaft resonant system.*

Provided this condition is satisfied, the magnitude of ϵ will progressively decrease to zero and the vector diagram in figure 18 will shrink into the origin. On the other hand, if the sum of the excitation is greater than the damping term, the vector diagram will progressively expand until ϵ becomes equal to the radial clearance—at which point the bearing may be destroyed.

In the above analysis the conditions which determine the dynamic stability of the bearing have been outlined. However, the bearing must also possess static stability, i.e., it must be capable of supporting a radial load, such as the weight of the shaft if it were horizontally supported. In this case, ω becomes zero and if ω_s is also zero then β is zero, and since $\tan(\alpha+\beta)=\omega CR$, the phase angle α also takes the value of zero. The stabilizing force $GZ\epsilon \sin\alpha$ thus reduces to zero, and the decentering force $GZ\epsilon \cos\alpha$ reduces to the value $GR\epsilon$. The centering force now becomes

$$F_A=(Y-GR)\epsilon, \tag{49}$$

and it is evident that GR should be less than Y in order to ensure static stability. If GR should be greater than Y, the shaft will be pushed to one side of the bearing. It is evident that the value of the leak resistance must be carefully chosen; it must be large enough to ensure dynamic stability; if it is made too large, however, the shaft will not float.

If we write

$$\frac{GR}{Y}=B, \tag{50}$$

then the static stability condition will be satisfied if B is less than one. The static centering force may now be written

$$F_A=Y\epsilon(1-B). \tag{51}$$

The value of the leak resistance is given by

$$R=\frac{P'}{I_R}=\frac{BY\epsilon}{G\epsilon}. \tag{52}$$

Substituting for G from (41) we get

$$R=\frac{BY}{N\pi A_2 r_j v \rho_1 \cos\frac{\pi}{N}\sec\beta}. \tag{53}$$

In the present bearing, B was chosen to be 0.75, and consequently, the static load carrying capacity is $0.25\,Y\epsilon$. The area of the shaft A_2 which faces each cavity is estimated to be as shown in figure 20. The value of β is given by (29). As a first approximation it may be assumed that $\beta=0$ and sec $\beta=1$. The flow velocity v is assumed to be sonic at the throat formed by the annulus $2\pi r_j\delta$; i.e., the discharge coefficient is assumed to be unity. The diameter of the leak orifices may be calculated with the aid of this equation. The discharge coefficient for a circular orifice is approximately 0.6.

Since the shaft is supported on two bearings, each of which behaves like a spring, it has two principal modes and frequencies of whirl. The calculation of the modes and frequencies of such a resonant system is described in standard textbooks on mechanical vibrations. However, for the convenience of the reader, the procedure in this specific application is outlined below.

The shaft of the miniature turbine and its supports are shown schematically in figure 19, where the following symbols and the corresponding values are used.

m=Mass of shaft—lb mass
r_g=Radius of gyration of shaft about the center of gravity—in.
Y_1=Stiffness of gas film in outer bearing—lb/in.
Y_2=Stiffness of gas film in inner bearing—lb/in.
L_1=Distance of outer bearing from center of gravity—in.
L_2=Distance of inner bearing from center of gravity—in.

It is assumed that the two radial spring constants are equal, i.e.,

$$Y_1=Y_2=Y-GZ\cos\alpha. \tag{54}$$

In this equation, a value for α which should provide the optimum damping is required. This value is given by the equation

$$\alpha=\frac{90°-\beta}{2} \tag{55}$$

where

$$\tan\beta=\frac{I_H}{I_j} \tag{56}$$

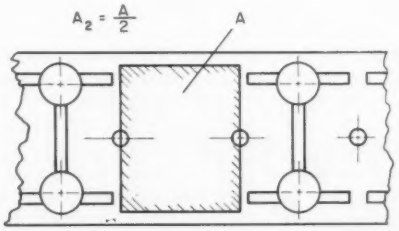

FIGURE 20. *Effective area facing cavity.*

as shown in figure 11. But I_H cannot be evaluated until the value of ω is known, and this depends on the value of $\cos \alpha$.

This difficulty may be circumvented if it is assumed as a first approximation that the angle β is zero and the angle α is 45°. With these values of α and β, Z becomes equal to $R/\sqrt{2}$ and (54) becomes

$$Y_1=Y_2=Y-\frac{1}{2}GR. \tag{57}$$

In the present calculation the value of R is arbitrarily chosen so that

$$GR=\frac{3}{4}Y. \tag{58}$$

The two frequencies of oscillation are given by the equations

$$\omega_1^2=\frac{1}{2}(a+c)+\sqrt{\frac{1}{4}(a-c)^2+\left(\frac{b}{r}\right)^2} \tag{59}$$

and

$$\omega_2^2=\frac{1}{2}(a+c)-\sqrt{\frac{1}{4}(a-c)^2+\left(\frac{b}{r}\right)^2} \tag{60}$$

where

$$a=\frac{Y_1+Y_2}{m},$$

$$b=\frac{L_2Y_2-L_1Y_1}{m},$$

$$c=\frac{L_1^2Y_1+L_2^2Y_2}{mr_g^2}.$$

Equations (59) and (60) are approximate and do not include the gyroscopic effects associated with rotation of the shaft. However, such effects can be ignored for the case considered here.

The distances of the nodes from the center of gravity are given by the equations

$$L_3=\frac{b}{\omega_1^2-a}, \tag{61}$$

$$L_4=\frac{b}{\omega_2^2-a}. \tag{62}$$

The positions of the two nodes are illustrated in figure 19. From the positions of the nodes it is seen that the predominant amplitudes of whirl in the inner and outer bearings occur at the lower and higher frequencies of whirl.

These values of ω_1 and ω_2 may now be employed in (31) and (54) in order to find more precise values of Y_1 and Y_2. From the revised values of Y_1 and Y_2, a more refined calculation of the values of ω_1 and ω_2 may be made. However, in view of the many uncertainties in the computation, the first approximation is usually sufficiently accurate for practical purposes.

The value of the phase angle β may now be calculated with the aid of (29). The optimum value of the phase angle α is given by (55).

The values of the stabilizing cavities may now be calculated. We have

$$\tan(\alpha+\beta)=\omega CR=\frac{\omega V\rho R}{P} \tag{63}$$

or

$$V_1=\frac{\tan(\alpha+\beta)P}{\omega_1\rho R} \tag{64}$$

and

$$V_2=\frac{\tan(\alpha+\beta)P}{\omega_2\rho R} \tag{65}$$

where ω_1 and ω_2 are the whirl angular velocities of the outer and inner bearings, V_1 and V_2 are the corresponding volumes of the stabilizing cavities, and ρ is the density of the gas at P units of pressure.

Referring to figures 12 and 11, it is seen that the vectors of pressure and current are given by the equations

$$\mathbf{P}'=\mathbf{I}'\mathbf{Z} \tag{66}$$

and

$$I'=I_j \sec \beta. \tag{67}$$

The value of Z is given by the equation

$$Z=\frac{R}{\{1+\tan^2(\alpha+\beta)\}^{1/2}}. \tag{68}$$

The value of the force F', figure 14, due to a single cavity is given by the equation

$$F'=A_2P' \tag{69}$$

where A_2 is the effective area of the shaft (fig. 20) which forms part of the walls of the cavity. The value of the force GZ_ϵ (fig. 18) is given by the equation

$$GZ_\epsilon=\frac{N}{2}F'. \tag{70}$$

Thus the value of GZ_ϵ is given by

$$GZ_\epsilon=\frac{NA_2RI_j \sec \beta}{2\{1+\tan^2(\alpha+\beta)\}^{1/2}}. \tag{71}$$

The corresponding tangential and radial components of force are $GZ_\epsilon \sin \alpha$ and $GZ_\epsilon \cos \alpha$.

The condition for dynamic stability is given by (48); i.e.,

$$GZ_\epsilon \sin \alpha > k'T_\epsilon+E_H\epsilon. \tag{72}$$

Provided this condition is satisfied, the direction of the resultant of all the forces acting on the shaft lies behind the line of centers as shown in figure 18. Thus the orbit of the center of the shaft should be a spiral of decreasing amplitude as shown in figure 3.

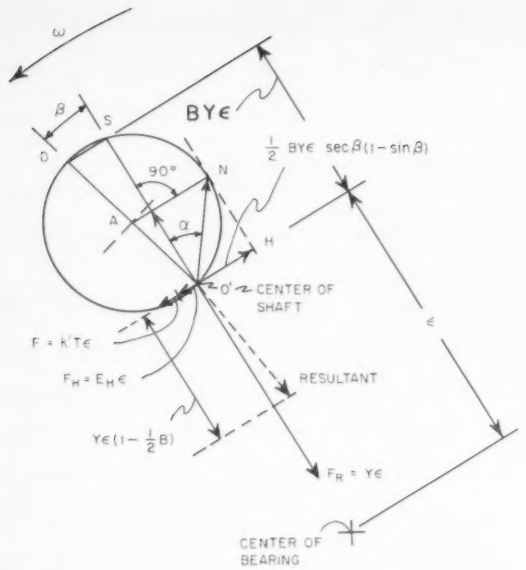

FIGURE 21. *Vector diagram of forces illustrating design procedure.*

Consequently, the bearing should be stable. This was proved experimentally in the bearings of the miniature turbine which is described by Birmingham, Sixsmith, Wilson [1962]

The design procedure and the relationship between the various forces may be illustrated with the aid of the geometrical construction shown in figure 21. The angle β is preferably chosen to be less than 20°, assuming zero whirl velocity, and the diameter of the injector holes is calculated according to (29) to satisfy this condition.

In figure 21 we have:

$$O'S=BY\epsilon \tag{73}$$

$$O'D=BY\epsilon \sec \beta \tag{74}$$

$$AN=1/2BY\epsilon \sec \beta \tag{75}$$

$$O'H=AN-O'A \sin \beta$$

$$=1/2BY\epsilon \sec \beta(1-\sin \beta). \tag{76}$$

Thus the stabilizing force $O'H$ may be expressed directly in terms of the centering force $Y\epsilon$. The condition for dynamic stability may now be expressed as

$$1/2BY\epsilon \sec \beta(1-\sin \beta)>k' T\epsilon+E_H\epsilon. \tag{77}$$

In a trial design the number of pads and the radial clearance are adjusted until the above stability condition is satisfied. Then the diameter of the leak orifices and the volume of the stabilizing cavities may be calculated as follows.

The values of Y_1 and Y_2 according to (57) are given more simply by the equation

$$Y_1=Y_2=Y\left(1-\frac{1}{2}B\right), \tag{78}$$

and then the values of the whirl angular velocities may be calculated with the aid of (59) and (60). The diameter of the leak orifices may be calculated according to (53). Then the values of the stabilizing cavities may be calculated according to (64) and (65). This completes the design.

In the theory outlined above, it is assumed that the leakage along the shaft from the stabilizing cavities is negligible. Such leakage introduces a phase shift which tends to promote instability. Conversely, a leakage along the shaft and into the stabilizing cavities tends to promote stability. Consequently, it is desirable that the pressure at the ends of the bearing should be equal to or greater than the static pressure in the stabilizing cavities.

7. Conclusion

It is possible and quite practical to provide stable, externally pressurized gas-lubricated bearings for high-speed shaft operation. The stabilizing cavities employed in this design are a definite asset to a bearing system of this type and have been shown by actual tests to suppress shaft whirl inherent in externally pressurized bearings.

The bearing described here is adaptable to small shafts (one inch diameter and smaller) which are lightly loaded and require speeds well beyond the allowable operating range of rolling contact bearings. For miniature applications, the size of the bearing and shaft system is limited only by practical fabrication techniques.

This type of bearing is particularly advantageous for miniature turbine expanders used in cryogenic refrigerator systems, where the process gas can be used as the bearing gas medium. In this arrangement, the problem of contaminating the process gas from the bearing lubricant is eliminated. It also eliminates a mechanical seal between the bearings and the process expansion system.

A prototype turbine expander, incorporating externally pressurized gas-lubricated bearings, was fabricated and tested with helium gas as the operating medium. The bearings were designed using the criterion described in this manuscript. The tests showed that the bearings were reliable and performed quite satisfactorily. No detectable shaft whirl was encountered up to the design speed of the turbine shaft.

8. Summary of Nomenclature

A_1=Area of pad—in.^{2}
A_2=Effective area of shaft surface facing cavity—in.^{2}
B=Constant defined in eq (50)

C=Capacity of cavity
D=Diameter of pad—in.
E_H=Tangential "spring" modulus—lb/in.
F=Horizontal force on blading—lb
F_A=Static centering force—lb
F_X=Force due to gas pressure on shaft—lb
F_H=Tangential force—lb
F_R=Radial restoring force—lb
F_0=Steady force—lb
F'=Alternating vector of force—lb
F_S=Vector sum of forces due to N cavities—lb
G=Constant defined in eq (41)
h=Mean tip clearance between ϕ and $\phi+d\phi$—in.
h_1, h_2=Clearances between shaft and bearing. See figure 9—in.
I_c=Alternating component of current flowing in cavity—lb/s
I_L=Current through leak—lb/s
I=Flow of gas into cavity—lb/s
I_0=Steady component of flow into cavity—lb/s
I_j=Alternating component of flow into cavity—lb/s
I_a=Alternating flow due to shaft rotation (eq 25)
I_W=Alternating flow due to shaft whirl
I_H=Alternating flow due to the combined effects of shaft rotation and whirl
I'=Alternating flow into cavity
k=Constant defined in eq (17)
k_1=Correction for overhang of rotor
k'=Constant defined in eq (46)
L=Length of bearing—in.
L_e=Effective length of stabilizing cavity—in.
L_1, L_2, L_3, L_4, L_5=See figure 19
m=Mass of shaft in plane of bearing—lb
N=Number of pads in bearing
$n=\frac{\epsilon}{\delta}$=Eccentricity ratio
O=Center of bearing
O'=Center of shaft (see fig. 1)
O''=Instant center of orbit of shaft (see fig. 2)
P=Pressure in cavity—psi
P_0=Steady component of pressure in cavity—psi
P'=Alternating component of pressure in cavity
R=Resistance of leak orifice—sec/in.^{2}
r=Radius of shaft—in.
r_1=Turbine rotor tip radius—in.
r_2=Turbine rotor root radius—in.
r_m=Turbine rotor mean radius—in.
r_g=Radius of gyration of shaft about its center of gravity—in.
T=Total torque acting on turbine rotor—in.-lb
t=time—sec
V=Volume of stabilizing cavity (see eq (19))—in.^{3}
V_1=Volume of stabilizing cavities in outer bearing—in.^{3}
V_2=Volume of stabilizing cavities in inner bearing—in.^{3}
v=Velocity of gas at edge of injector hole—fps
v_1=Axial component of velocity of gas through rotor tip clearance—fps
v_2=Axial component of velocity of gas through the annulus between r_1 and r_2—fps
Y=Radial spring modulus—lb/in.
Y_1="Spring" modulus of gas film in outer bearing—lb/in.
Y_2="Spring" modulus of gas film in inner bearing—lb/in.
Z=Impedance of resistance capacitance network

Greek

α=Phase angle between complex pressure vector and eccentricity ϵ
β=Phase angle between resultant current I' and eccentricity ϵ
γ=Angle between ϵ and a diameter through the center of a pair of diametrically opposed pads
δ=Radial clearance—in.
ϵ=Shaft eccentricity—in.
θ=See figure 2
μ=Viscosity of gas—lb-sec/in.^{2}
ρ=Density of gas in cavity—lb/ft^3
ρ_1=Density of gas at edge of injector hole—lb/ft^3
ρ_2=Density of gas in clearance space between shaft and bearing—lb/ft^3
ϕ=See figure 8
ω=Angular velocity of whirl—radians/s
ω_1=Angular velocity of whirl in outer bearing—radians/s
ω_2=Angular velocity of whirl in inner bearing—radians/s
ω_s=Angular speed of shaft—radians/s

9. References

F. T. Barwell, (1956). Lubrication of bearings, p. 168. Butterworths Scientific Publications, London, England.

B. W. Birmingham, H. Sixsmith, and W. A. Wilson, (1962). The application of gas-lubricated bearings to a miniature helium expansion turbine, Advan. Cryog. Eng., Vol. **7,** p. 30, K. D. Timmerhaus (ed.), Plenum Press, Inc. New York, N.Y.

G. F. Boeker, B. Sternlicht, (1956). Investigation of Translatory Whirl in Vertical Machines, Trans. ASME, **78,** 1.

G. W. K. Ford, D. M. Harris, and D. Pantall, (1957), Principles and applications of hydrodynamic-type gas bearings, Instit. Mech. Eng., **171,** 2.

H. Sixsmith, (April 28, 1959a). Bearings for rotating shafts which are lubricated by gas, U.S. Patent No. 2,884,282, British Patent No. 797,528.

H. Sixsmith, (1959b). The theory and design of a gas-lubricated bearing of high stability, Proceedings of First International Symposium on Gas-Lubricated Bearings, ACR-49, Office of Naval Research, Washington, D.C.

H. Sixsmith, W. A. Wilson, and B. W. Birmingham, (1961). Load-carrying capacity of gas-lubricated bearings with inherent orifice compensation using nitrogen and helium gas, NBS Tech. Note 115.

Paper 68C2-156

JOURNAL OF RESEARCH of the National Bureau of Standards—C. Engineering and Instrumentation
Vol. 68C, No. 2, April–June 1964

Infrared Spectra of Asphalts: Some Aspects of the Changes Caused by Photooxidation

Paul G. Campbell and James R. Wright

(November 29, 1963)

The infrared spectra of coating-grade asphalts to which model organic compounds were added were compared with spectra of the original asphalts and with photooxidized asphalts. By this method, it was shown that the principal oxygen-containing products formed in the asphalt during air- or photooxidation were aldehydes, ketones, and acids. The presence of esters could not be confirmed.

The effects of air-blowing conditions and elevated temperature storage on several asphalts were examined by infrared spectroscopy. Elevated temperature (~260 °C) storage of air-oxidized apshalts, under nitrogen, decreased absorbance in the carbonyl band at 1700 cm^{-1} and reduced durability to accelerated weathering.

Photooxidation reactions that occurred at the surface of thick (625 μ) asphalt films, as detected by infrared spectroscopy, were the same as those which took place in the thin (25 μ) films. Also, the photooxidation rates were comparable. Only negligible amounts of photooxidation occurred at a depth of 10 μ beneath the surface.

1. Introduction

The initial application of infrared spectroscopy to the analysis of aphaltene-type materials was made a decade ago by Hadzi [1] [1] who studied qualitatively the infrared spectra of the light-petroleum-solvent-insoluble, benzene-soluble fraction of various materials. Friedel and Queiser [2] made an infrared spectrum of an apshalt film in 1956 and used it to illustrate the similarities to the spectra of coal asphaltenes. Also, in 1956, Knotnerus [3] applied infrared analysis to determine the oxygen-containing functional groups formed during the air blowing of asphaltic bitumens.

Stewart [4] described the infrared spectra of asphalt fractions separated by chromatographic techniques in 1957. In this research, asphalts were separated into four fractions and an infrared spectrum was made of each fraction. Samples of the original asphalts were then exposed for 30 months outdoors, subsequently fractionated, and an infrared spectrum was made from each fraction of the exposed asphalt. Some of the structural changes produced by weathering were elucidated by this method. Stewart worked with solvents, a heated cell, potassium iodide pellets, and mineral oil mulls in obtaining the spectra of various asphalts and asphalt fractions.

In a study of the absorbance of asphaltic materials, Schweyer [5], in 1958, made infrared spectra of asphalt films 0.1 mm thick. For wavelengths below 8 μ, it was necessary to use carbon tetrachloride solutions of the asphalts. Schweyer attempted to explain certain differences in the properties of asphaltic materials on the basis of the ultraviolet and infrared spectra. Romberg et al. [6], used infrared spectroscopy in the analysis of asphalt components from gel, sol-gel, and sol asphalts in 1959. From the results thus obtained, the percentages of various carbon linkages in each fraction were calculated and compared with other properties such as C/H ratio, elemental analyses, and molecular weight.

Beitchman [7], in 1959, described a method for the preparation, irradiation, and infrared analysis of thin films of air-blown asphalts of about 25 μ thickness. Beitchman observed that increases in absorbance at 3435 cm^{-1} (2.91 μ), 1700 cm^{-1} (5.88 μ), and 1030 cm^{-1} (9.71 μ), [OH, C=O, C—O groups, respectively], were produced by exposure of unsupported films of asphalt to the radiant energy of a carbon arc. Yen [8], in 1962, published the results of an extensive investigation into the structure of petroleum asphaltenes by infrared analysis.

The research described by Beitchman [7] was the first successful effort to produce infrared spectra of asphalt films without resorting to solvents, mulls, pellets, or salt-crystal supports. The unsupported film was particularly adaptable to research on asphalt photodegradation. The films could be scanned, irradiated, and rescanned without modification to the asphalt other than that caused by photodegradation. Wright, Campbell, and coworkers modified the unsupported film technique [9–11] and used it extensively to determine photooxidation rates of asphalts [10], the effect of temperature and relative humidity on asphalt oxidation [11], and the relationship between carbon-arc intensity and asphalt oxidation [12]. Changes in absorbance at 1700 cm^{-1}, the carbonyl index, were employed to measure photooxidation.

The present paper is an extension of this research with the general objective of interpreting more fully some of the changes observed in the infrared spectra of asphalts due to photooxidation. Specific areas

[1] Figures in brackets indicate the literature references at the end of this paper.

investigated include the nature of the carbonyl compounds with absorbance at 1700 cm^{-1}, spectral changes produced by air oxidation and by elevated temperature storage of asphalts, oxidation rates of thick films, and the depth of the photooxidation reaction in asphalt.

2. Infrared Spectra of Asphalts Containing Model Organic Compounds

Infrared spectroscopy gives evidence of the presence in a material of characteristic groups such as hydroxyl or carbonyl groups. If the material is a pure compound, such information is often definitive. If, on the other hand, the material is a mixture, the interpretation is more complicated as the location of any functional groups, relative to any compound in the mixture, is not normally known.

The complexity of asphalts limits the interpretation of their infrared spectra. Similarly, the changes which occur in the infrared spectrum of an asphalt upon photooxidation are subject to limited interpretation. For example, with respect to absorbance in the carbonyl band at 1700 cm^{-1}, relative changes in the spectra of asphalt films can be measured with considerable accuracy [10]; the source of the carbonyl group, whether it be aldehyde, ketone, acid anhydride, ester, etc., can not be established easily [13].

It is possible, however, to gain some insight as to the identity of these compounds by an indirect approach which consists of adding model organic compounds to an asphalt, scanning a film of the mixture, and observing the changes produced in the infrared spectrum. New absorbance peaks or shoulders are produced if the compound type differs from those in the asphalt. Existing absorbance peaks are reinforced if the model-compound additive corresponds to compounds of the same types already present in the asphalt. The model-compound-additive method was employed in this research to elucidate the types of compounds formed during photooxidation of asphalt with special emphasis on the changes which occur in the absorbance at 1700 cm^{-1}.

2.1. Experimental Procedure

a. Methods

The method for the preparation, irradiation, and infrared analysis of unsupported asphalt films has been described elsewhere [10]. The model organic compounds were incorporated into the asphalt in the following manner: a known amount of a selected asphalt was heated on a hot plate under a blanket of nitrogen until melting occurred. The organic compound was added (1 to 2% by weight) and the resultant mixture stirred until relatively homogeneous. The mixture was then covered and cooled to room temperature. The whole operation required 7 min.

Films (25 μ thick) of the additive-treated asphalts were prepared as described in [10]. Infrared scans were made of these films. For direct comparison, the spectrum of the additive-containing asphalt was made on the chart paper which contained the spectrum of the corresponding untreated asphalt from a film of similar thickness. Perkin-Elmer infrared spectrophotometers (Models 221 and 137) were used in making the infrared scans.

b. Materials

Two air-blown roofing asphalts were used in the present study: One asphalt (No. 16) was of Midcontinent United States origin and had shown a durability to accelerated weathering (ASTM D529–59T) of 93 days using the 51–9C cycle (9 min of cold water spray in each hour). The other asphalt (No. 9) was a California Coastal asphalt fluxed with reclaimed lubricating oil; its durability was 32 days. Properties of these asphalts have been described elsewhere [9].

2.2. Infrared Spectra of Air-Blown Asphalts

a. Asphalts With No Compounds Added

The infrared spectra of a typical air-blown asphalt before and after photooxidation are shown in figure 1. Significant changes in absorbance may be observed at 3436 cm^{-1}, 1700 cm^{-1}, and 1600 cm^{-1}. According to Stewart [4], respective absorbances at these wave numbers are due to: OH stretching, C=O, aromatic and conjugated alkene and OH bonding. Also, absorbance changes at other wave numbers have been reported by Beitchman [7] and Stewart [4].

Of the absorbances mentioned above, relative changes due to photooxidation are best measured at 1700 cm^{-1} since this, the carbonyl band, is relatively free from interference by absorbances of other groups [14] and carbonyl absorbances can be determined with greater accuracy than other groups such as OH and C—O. This band was used extensively by the authors in previous investigations on the photodegradation of asphalts [9–12], but the identification of the types of organic molecules responsible for the absorbance at 1700 cm^{-1} was not made.

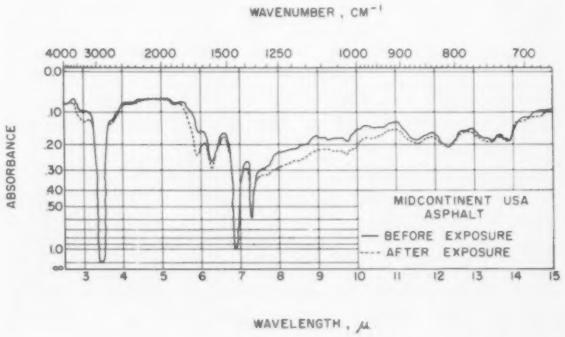

FIGURE 1. *Infrared spectra of a midcontinent U.S.A. asphalt before and after carbon-arc irradiation.*

b. Asphalts With Organic Compounds Added

The increased carbonyl absorbance observed in asphalt upon photooxidation may be due to any carbonyl-containing organic compounds. To investigate this phenomenon by the method described in section 2a, the asphalts were mixed with esters, aldehydes, ketones, acids, and anhydrides, respectively. A total of 14 different compounds was used. These compounds are listed in table 1 together with their chemical structure, characteristic absorbances, and the absorbances imparted to asphalts containing each compound.

The effects of various organic compounds on the infrared spectra of asphalt No. 16 [2] (with and without organic compounds added) are shown in figures 2 to 7. The changes produced by phthalic anhydride are shown in figure 2. Two carbonyl absorbance bands, characteristic of anhydrides are present at about 1845 and 1775 cm^{-1}. Bellamy [15] reports values of 1845 and 1775 cm^{-1} for phthalic anhydride. In addition to the carbonyl absorbance, there is evidence of the C—O—C stretching vibration at 1250 cm^{-1}. According to Colthup [16], vibration in the range of 1310–1210 cm^{-1} is characteristic of cyclic anhydrides.

TABLE 1. *Model organic compounds added to asphalts No. 9 and No. 16 and their contribution to the infrared spectra*

Compound	Structure	Characteristic absorbance(s)[1]	Absorbance(s) in asphalt [2]
		cm^{-1}	*cm*$^{-1}$
n-Butyl phthalate.	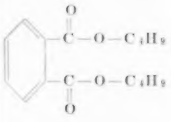	1730–1717 1310–1250 1150–1100	1730–1720 1275 (broad) 1115 (broad)
n-Butyl sebacate.	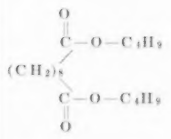	1750–1735 1172	1740 1185–1175
Ethyl cinnamate.	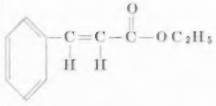	*1717 1300–1100	1720 (shoulder) 1310 (broad) 1165 (broad)
Tristearin.	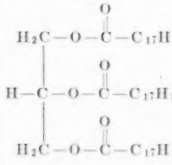	1751–1748 1250 1163 1110	1750 1250 (broad) 1160 1110 (broad)
Benzoic acid.	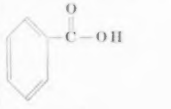	*1685 *1290 *714	1690 (shoulder) 1305 1035
Stearic acid.	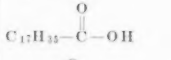	2700–2500 *1708 1350–1180	2600 (broad) 1705 1250 (broad)
Benzaldehyde.	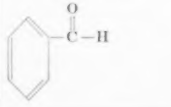	*1704 1300–1260	1705
Citral.	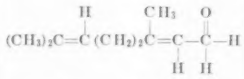	1705–1685 1440–1325 975–825	1705 1320 970
Trans-cinnamaldehyde.	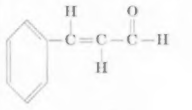	1705–1685 1230–1160	1700 1200 (broad)
n-Heptaldehyde.	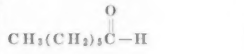	1740–1720 1440–1325	1710
Acetophenone.	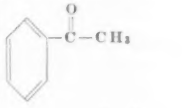	*1686	1690
Mesityl oxide.	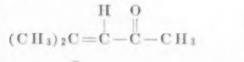	*1690 1325–1215	1700 1275 (broad)
Maleic anhydride.	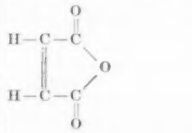	*1848 *1790 1310–1210	1840 1790 1215 (broad)
Phthalic anhydride.	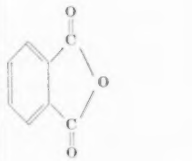	*1845 *1775 1310–1210	1845 1775 1250

[1] Source: L. J. Bellamy, *The infrared spectra of complex molecules*, 2d ed. (John Wiley and Sons, New York, N.Y., 1958). Asterisk (*) indicates value is specific for the compound. Unmarked entries refer to the class of compounds.
[2] Reference is made to the regions of increased absorbance in the asphalt-additive mixture over that found in the original asphalt.

[2] Asphalt 16 was selected for this study because it has a high initial absorbance in the carbonyl band and would reflect only large contributions due to additives.

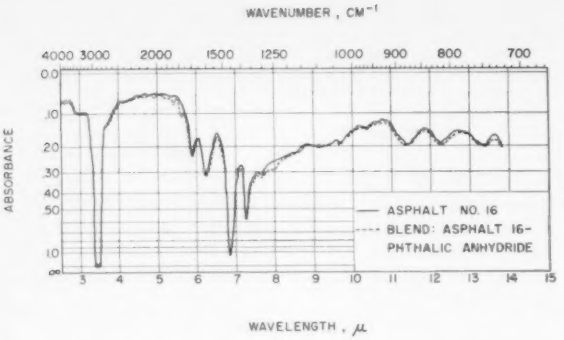

FIGURE 2. *Changes in the infrared spectrum of asphalt No. 16 caused by the addition of phthalic anhydride.*

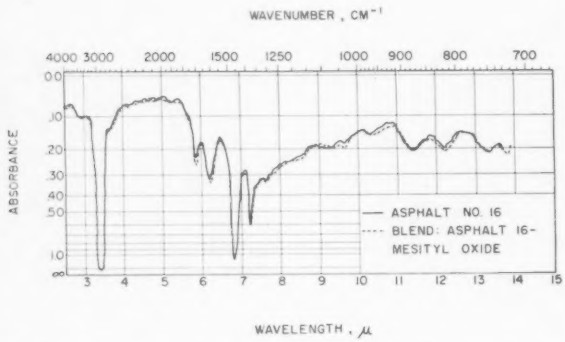

FIGURE 3. *Changes in the infrared spectrum of asphalt No. 16 caused by the addition of mesityl oxide.*

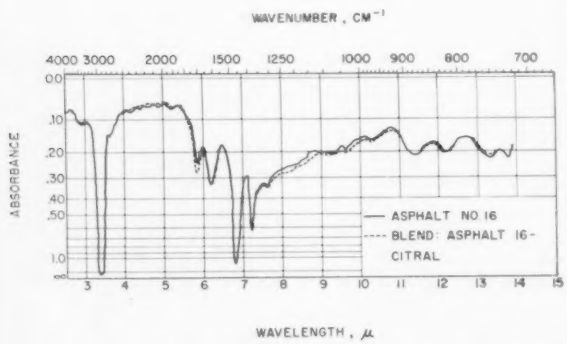

FIGURE 4. *Changes in the infrared spectrum of asphalt No. 16 caused by the addition of citral.*

The addition of mesityl oxide, an α-β-unsaturated ketone, to asphalt 16 produced increased absorbance at 1700 cm^{-1} and directly reinforced the normal absorbance of the asphalt at this wave number (fig. 3). Thompson and Torkington [17] show the frequency of the stretching vibration of the carbonyl group in mesityl oxide to be about 1690 cm^{-1}. Similarly, citral, an α-β-unsaturated aldehyde, increased carbonyl absorbance at 1705 cm^{-1} (fig. 4). α-β-Unsaturated aldehydes normally absorb in the range of 1705–1685 cm^{-1} [18].

The addition of a fatty acid, stearic acid, to asphalt 16 resulted in spectral changes typical of this class of compounds [19]. Slightly increased absorbance was observed in the 2700–2500 cm^{-1} range (bonded OH stretching vibration), at 1705 cm^{-1} (C=O vibration), and in the broad region around 1250 cm^{-1} (fig. 5). The increased absorbance in the 1705 cm^{-1} region enhances that of the original asphalt.

The addition of esters to asphalt 16 produced an effect not previously observed with any of the other classes of carbonyl compounds in air-blown asphalts or in photooxidized asphalts. Two absorbance peaks were formed due to C=O vibration. This effect is shown graphically in figures 6 and 7 with *n*-butyl sebacate and tristearin, a triglyceride, respectively.

Characteristics C=O absorbance for alkyl esters is in the range of 1750–1735 cm^{-1} with the *n*-butyrates at the lower end of the range [17]. This absorbance range is notably higher than the carbonyl frequency for alkyl ketones and aldehydes due to the influence of the adjoining oxygen [14]. The C=O absorbance for *n*-butyl sebacate in asphalt 16 is 1740 cm^{-1} while the absorbance of the asphalt alone in this region is at 1700 cm^{-1}. Similarly, the respective absorbances for C=O in tristearin and asphalt 16 are 1750 cm^{-1} and 1700 cm^{-1}. The triglycerides absorb in the range 1751–1748 cm^{-1} [21].

The C—O stretching vibrations due to esters (1300–1100 cm^{-1}) are found in the asphalt spectra with both *n*-butyl sebacate and tristearin. With the sebacate, an absorbance is found at 1185–1175 cm^{-1}. Sebacates absorb at 1172 cm^{-1} [20]. Characteristic C—O stretching modes for triglycerides are 1250, 1163, and 1110 cm^{-1} [21]. With tristearin, broad absorbance occurred at 1250, 1160, and 1110 cm^{-1}. Photooxidized asphalts also exhibit increased absorbance in the 1300–1100 cm^{-1} region (see fig. 1). However, with photooxidized asphalts, none of the characteristic bands for C—O vibrations in esters can be distinguished.

2.3. Discussion

By adding model organic compounds to an asphalt and observing the changes produced in the infrared spectra, it was shown that ketones, aldehydes, and acids reinforced the absorbance assigned to the C=O frequency at 1700 cm^{-1}, while acid anhydrides and esters did not contribute in this wave number region. The anhydrides exhibited two carbonyl absorbance bands at 1845 and 1775 cm^{-1}. The esters developed an absorbance in the 1750–1735 cm^{-1} region forming a doublet with the carbonyl absorbance in the asphalt. Thus, it appears that the increased absorbance found in oxidized asphalts is due largely to ketones, aldehydes, and acids with no contribution from anhydrides and little or no contribution from esters. This generalization is applicable to asphalts

oxidized in air, in oxygen, and in oxidants other than oxygen [22] as well as specimens subjected to photo-oxidation.

The insignificant contribution of esters as a source of oxygen in oxidized asphalts is worthy of further comment. In 1955, Goppel and Knotnerus [23] published a paper on the fundamentals of bitumen blowing in which more than 60 percent of the oxygen in the blown bitumen was attributed to ester groups.[3] Furthermore, since esters link two different molecules, it was postulated that esters contributed to the formation of higher molecular weight materials. Proof of ester formation, based on saponification values and spectroscopic evidence, was described in a separate paper by Knotnerus [3]. These two papers have been referenced frequently in the subsequent literature dealing with asphalt oxidation under a variety of experimental conditions [24-27].

Since the present work does not support the contention that esters are the predominant oxygen-containing molecules in oxidized asphalt, the discrepancy may be explained as follows: The spectroscopic evidence offered by Knotnerus [3] is based upon the nearly complete disappearance of a strong carbonyl absorption band at 1724 cm^{-1} and the formation of a new band at 1587 cm^{-1} (carboxylic acid salts) when blown bitumens are saponified with excess alkali. (The remaining absorbance at 1724 cm^{-1} was believed due to aldehydes and ketones.) The possibility of high molecular weight acids was ruled out because the hydrogen bridges were not observed between the solvent employed in the spectroscopic method and the potential acids. This evidence, coupled with saponification values, was offered as proof that esters were the predominant molecular type. It is the authors' contention that the presence of "acid-solvent hydrogen bridges" would be extremely difficult to detect by infrared spectroscopy in a solution containing the whole asphalt. And furthermore, that the absence of such bridges under these conditions is rather weak evidence for selecting esters rather than acids as the predominant oxygen-containing molecule.

Saponification values also may be misleading because compounds other than esters may produce positive result. Siggia [28], in discussing the limitations of the saponification equivalent method, pointed out that the presence of reactive compounds would give erroneous results to the method used in ester determination. According to Shriner et al., [29], hot concentrated alkali affects functional groups other than esters. For example, aldehydes with α-hydrogen atoms undergo aldol condensation, aldehydes with no α-hydrogen atoms undergo Cannizzaro's reaction, and β-diketones undergo cleavage under the influence of hot alkali.

To supply further evidence of this fact, saponification equivalents were measured on *n*-heptaldehyde and acetophonone for 4 and 24 hr alkali treatment. The values for the aldehyde were 525 and 253, and for the ketone were 10,020 and 1,469, respectively.

[3] Similar effects were postulated for aged bitumens.

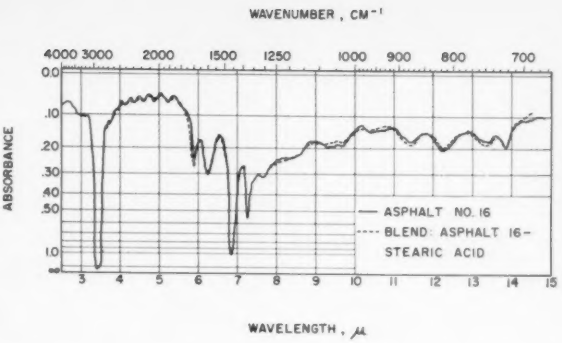

FIGURE 5. *Changes in the infrared spectrum of asphalt No. 16 caused by the addition of stearic acid.*

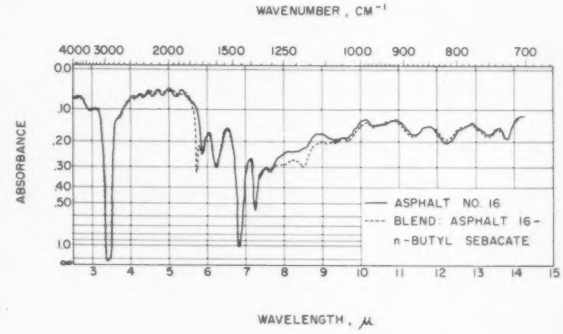

FIGURE 6. *Changes in the infrared spectrum of asphalt No. 16 caused by the addition of n-butyl sebacate.*

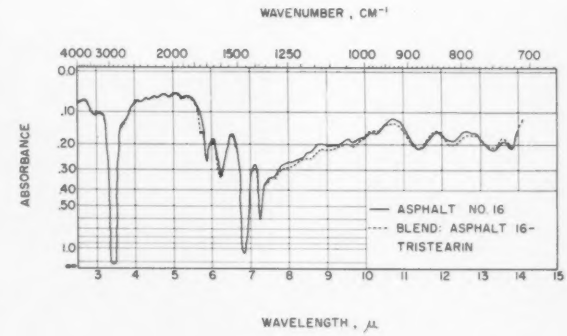

FIGURE 7. *Changes in the infrared spectrum of asphalt No. 16 caused by the addition of tristearin.*

The present work does not, of course, rule out ester formation entirely. It is well known that α-β-unsaturated esters exhibit carbonyl absorbance in the region of 1720 cm^{-1}. The addition of ethyl cinnamate (C=O frequency of 1717 cm^{-1}) to asphalts 16 and 9 broadened the carbonyl absorbance but gave no doublet as was the case with normal saturated esters. Also, in photooxidation of asphalts, poorly defined shoulders are sometimes observed on the main carbonyl absorbance region; these might be attributed to ester formation since asphalts contain both acids and alcohols. It should be noted that esters containing one or more β-hydrogen atoms in the alkyl group may decompose photochemically by an intramolecular rearrangement into an olefin and the corresponding acid [30]. In general, it is concluded that the oxygen in oxidized asphalts is principally in the form of aldehydes, ketones, or acids (the present results do not distinguish among these classes) with a relatively minor part as esters.

3. Spectral Changes Caused By Air-Oxidation and Elevated-Temperature Storage

The changes in the infrared spectra of the asphalts described in section 2 were produced by the addition of model organic compounds to the asphalts. Most hard asphalts, however, are manufactured by air oxidation at temperatures in the order of 260 °C (500 °F). Therefore, it was of interest to elucidate the spectral changes produced in asphalt under these conditions as well as those produced by storage of the asphalt at the elevated temperatures used in the air-oxidation process.

Three asphalt fluxes, of Midcontinent United States, Venezuelan, and Southeast United States origin, were used. The designations of these fluxes, some physical properties, the conditions of air oxidation, and the softening points (S.P.) (ASTM D36–26) of the oxidized asphalts are given in table 2. (For more details on these materials, see Greenfeld [31].)

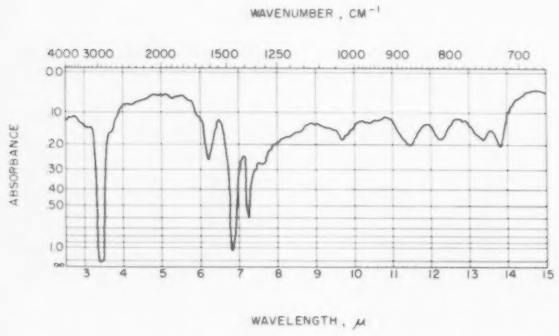

FIGURE 8. *Infrared spectrum of Kansas L–22 asphalt flux, softening point, 39° C.*

(Film supported on NaCl Plates.)

The infrared spectrum of the Kansas L–22 asphalt flux, before air oxidation, is shown in figure 8.[4] The area around 1700 cm^{-1} shows practically no absorbance indicating little or no oxygen in the C=O form. Upon air oxidation to a softening point of 104 °C (219 °F), considerable absorbance was observed in the 1700 cm^{-1} region indicating the formation of C=O oxygen (see fig. 9).

Absorbance around 1700 cm^{-1} may be attributed to C=O in the form of aldehyde; ketone, and/or acid. The change in absorbance at 1300 cm^{-1} may well represent alkyl ketones and aromatic aldehydes.

Another change appeared in the region [5] of 760–720 cm^{-1}. Well-defined absorbances occurred at 750 cm^{-1} and 725 cm^{-1} in the asphalt flux. In the air-oxidized asphalt, these absorbances were less intense and poorly defined.

The infrared spectrum (not shown) of the air-oxidized but softer asphalt (S.P.=80 °C) was similar to that of the more highly oxidized asphalt (S.P.=104 °C). The main difference was one of absorbance intensity in the 1700 cm^{-1} region; the softer product showed less absorbance and, consequently, less carbonyl formation.

Storage of the In-grade [6] Kansas L–22 asphalt (S.P.=104 °C) at 243 °C (470 °F) for 19 hrs under a nitrogen atmosphere caused a decrease in S.P. to 95 °C. Correspondingly, the absorbance intensity in the 1700 cm^{-1} region decreased, but no shift in the absorbance region was observed. Apparently some thermal degradation of the oxygen-containing molecules took place. The storage temperature of 243 °C was severe enough to cause decarboxylation of organic acids.

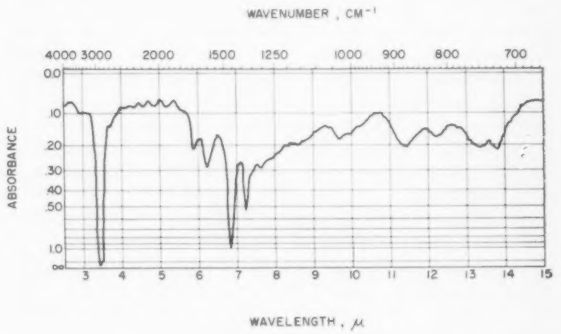

FIGURE 9. *Infrared spectrum of coating-grade asphalt (softening point, 104° C.)*

(Made from Kansas L-22 flux.)

[4] The softening point of the L-22 flux was 38 °C (101 °F); too low for an unsupported film. For this reason, the asphalt film was prepared between sodium chloride plates.

[5] Bellamy [32] interprets strong absorbances in this region as due to aromatic substitution. Yen and Erdman [8] assign absorbances for asphaltenes in the 865–760 cm^{-1} range as due to aromatic out-of-plane bending frequencies.

[6] The designation "In-grade" refers to an asphalt which meets the industry's specifications with respect to softening point and penetration.

The relationship between asphalts modified by air-oxidation or elevated-temperature storage and their photooxidation rates was determined. The physical properties of the asphalt fluxes before and after asphalt oxidation are shown in table 2. The

TABLE 2. *Physical properties of asphalt fluxes before and after air oxidation*

Designation	Before air oxidation		After air oxidation			Air-oxidation conditions[1]		
	Softening point	Penetration at 25 °C	Below grade	In-grade	After storage	Temperature	Time	Air rate
		1/10 mm	Softening point					
	°C		°C	°C	°C	°C	Min	ml/min
Kansas L–22	38	249	80	104	[2] 95	243	73	9500
Tia Juana 612	40	152	99	104	[3] 97	246	64	4750
Talco 16–RF–2	40	190	98	102	[4] 94	243	81	4750

[1] Conditions given are those used to produce asphalt designated "In grade" [31].
[2] Stored for 19 hr at 243 °C, under nitrogen.
[3] Stored for 21 hr at 246 °C, under nitrogen.
[4] Stored for 21.5 hr at 243 °C, under nitrogen.

experimental method was that employed by Wright and Campbell [10] in which 25 μ films of each asphalt were exposed to the radiant energy of the carbon arc. Oxidation was measured as a function of exposure by the changes occurring in C=O absorbance at 1700 cm^{-1}. The asphalts exposed and the resultant carbonyl indices are shown in table 3.

Oxidation-rate curves are plotted for Kansas L–22 asphalts in figure 10. The asphalt that was least susceptible to photooxidation was the In-grade asphalt (S.P.=104 °C). Film failure occurred after 16-hr exposure. The Below-grade asphalt (S.P.=80 °C) exhibited a slightly higher photooxidation rate, but film failure did not occur until after 18.5 hr. The least durable asphalt, with a much higher photooxidation rate and a film life of only 12 hr, was the asphalt subjected

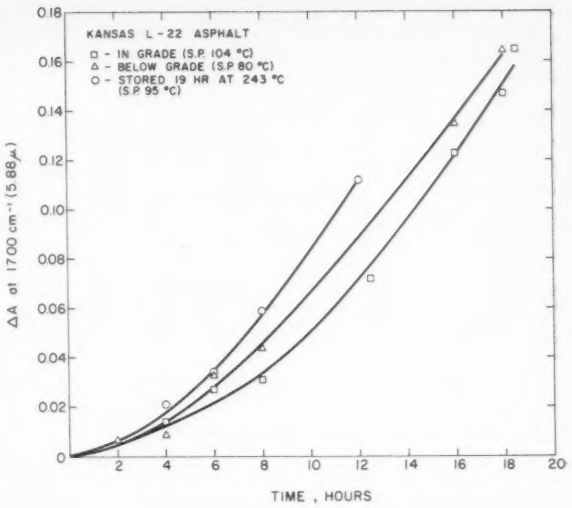

FIGURE 10. *Effect of carbon-arc exposure (49 °C., 40 percent R.H.) on the change in infrared absorbance of various Kansas L–22 asphalts at 1700 cm^{-1}.*

to elevated temperature storage. It appears that degradation reactions initiated thermally might well have continued under conditions for photodegradation.

4. Spectral Changes in the Surface of Thick Asphalt Films Upon Photooxidation

4.1. Spectral Changes

The spectral changes in the asphalt described in sections 2 and 3 were determined with thin films of 25 μ (1 mil) thickness. However, the usual methods for the exposure of asphalts to solar or carbon-arc

TABLE 3. *Changes produced in carbonyl indices of various asphalts by irradiation* [1]

Asphalt	Carbonyl index (ΔA at 1700 cm^{-1})								
	Kansas L–22			Tia Juana 612			Talco 16–RF–2		
Softening point, °C	80	104	95	99	104	97	98	102	94
Exposure time, hr:									
2	0.007			0.014	0.018	0.015	0.013	0.014	0.019
4	.009	0.014	0.021	.030	.027	.034	.028	.034	.022
6	.033	.027	.034	.050	.040	.056	.040	.054	.051
8	.044	.031	.059	.071	.069	.080	[5] .067	[4 5] .076	.072
10				.114	.115	.135	.098	.110	.126
12		[2] .072	.112	.159	.156		.133	.143	.147
13				[4] .162					
14							.165	.157	.180
15									.192
16	.135	.123					.171	.186	.184
17							.179	.186	[6] .209
18	[3] .165								

[1] Irradiated in Atlas SMC-R Weather Ometer at 49°C and 40 percent R.H. for time periods indicated.
[2] Irradiated for 12.5 hr.
[3] Irradiated for 18.5 hr.
[4] One sample only.
[5] Irradiated for 7.75 hr.
[6] Irradiated for 17.25 hr.

radiant energy employ asphalt films of 625 μ (25 mils) thickness [33]. In order to compare by infrared methods the changes observed in the thin films with those which occurred on and near the surface of the thick films upon photooxidation, slices of 25 μ thickness were removed from the surface of irradiated thick films and their infrared spectra determined.

A Southeast U.S.A. asphalt, No. 6, was used in this study. An asphalt specimen was prepared by pouring the molten asphalt into a small aluminum weighing dish to a depth of about 625 μ. A 3.8-cm diam microtome specimen holder was then embedded into the soft asphalt. Upon cooling, the asphalt was cut to the diameter of the specimen holder and the surface was shaved smooth with a microtome (Spencer, Model 860).

The asphalt samples were exposed to the radiant energy of a carbon arc at 49 °C and 40 percent R.H for the desired time period. The samples were mounted in the same respective positions in the accelerated weathering machine as were previous samples of thin films. After exposure, a 25 μ slice was removed from the surface, weighed to check thickness, and then pressed between sheets of unlacquered cellophane in a heated press to prepare a specimen suitable for infrared analysis.

The infrared spectrum of a 25 μ film of asphalt 6, prepared from the irradiated surface of a 625 μ film is shown with the spectrum of an unexposed thin film asphalt 6 in figure 11. The changes in the infrared spectrum of the asphalt obtained from the surface of the thick film are the same as those produced in the thin films, namely those at 3435 cm^{-1} (OH), 1700 cm^{-1} (C=O), and 1030 cm^{-1} (C—O). The carbonyl absorbance at 1700 cm^{-1} and the absence of absorbance at 1740 cm^{-1} indicates that the oxygen is in the form of acids, aldehydes, and ketones. The slight increase in absorbance at 2750 cm^{-1} suggests the presence of carboxylic acids and that around 1300 cm^{-1} the presence of alkyl ketones and aromatic aldehydes.

Figure 12 shows the changes which occurred in the infrared spectrum of a thin film of asphalt 6 under the same exposure conditions as those used with the thick films. Significant changes in absorbance occurred at 3435 cm^{-1}, and 1700 cm^{-1}, and increases in general absorbance at 1030 cm^{-1}, as was the case with the thick films. Even the absorbance intensities in these regions were about the same. These results indicate that the photooxidation reactions occurring in the thin films, as determined by infrared spectroscopy, are essentially the same as those which take place at the surface of thicker asphalt films under the exposure conditions used in the present work.

4.2. Photooxidation Rates

A comparison was made of the photooxidation rates of thin films of asphalt 6 and that which occurred on the surface of thick films of the same asphalt. To do this, a series of 625 μ films were

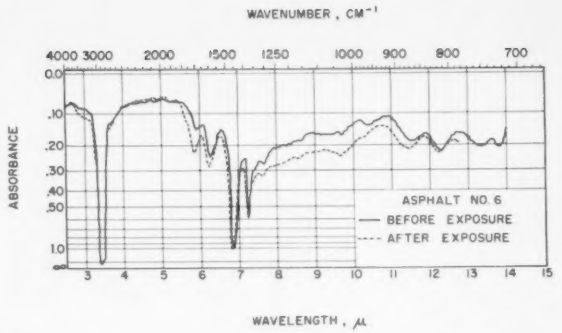

FIGURE 11. *Comparison of the infrared spectra of unexposed asphalt No. 6 (25 μ-thin film) with that of a film made from the surface (25μ-microtome slice) of the exposed asphalt (625μ thick film).*

(Exposure was for 7.5 hr to carbon-arc radiation at 49 °C and 40 percent R.H)

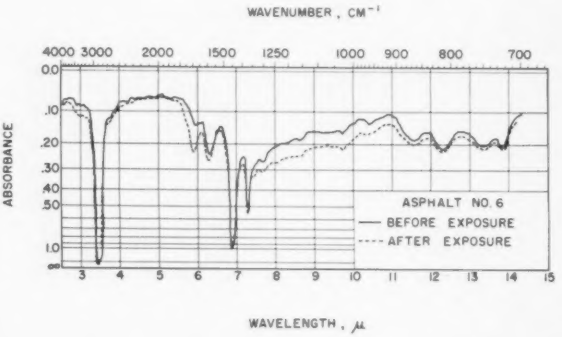

FIGURE 12. *Infrared spectra of asphalt No. 6 (25 μ thin film) before and after 7.5 hr. exposure to carbon-arc radiation at 49 °C and 40 percent R.H.*

prepared on microtome holders and exposed for varying durations to carbon-arc radiant energy at 49 °C and 40 percent R.H. After selected exposure periods, 25 μ slices were removed from each film and specimens prepared for infrared analysis as described in 4.1.[7]

A survey of the exposure data (table 4) shows that no significant difference exists in the photooxidation rates of the two films based on carbonyl index for at least the first 10-hr exposure. For greater durations, the surface became hardened, brittle, and uneven. As a result, films of uniform thickness could not be sliced from the asphalt specimen. This was manifested by the large variance of ΔA values obtained beyond the 10-hr exposure period. For this reason, photooxidation rates of 25 μ and 625 μ films could not be compared for an exposure period of more than 12 hr.

[7] In order to calculate the carbonyl index (ΔA at 1700 cm^{-1}) [10], the initial carbonyl absorbance of these films was estimated from a graph (previously prepared on thin films of asphalt 6) of film thickness versus initial carbonyl absorbance.

TABLE 4. *Changes produced in carbonyl indices of 25 μ films and in 625 μ films of asphalt No. 6 by irradiation*[1]

Exposure time	Carbonyl index	
	25 μ film	surface of 625 μ film[2]
hr		
2	0.011	0.015
4	.024	.022
6	.045	.048
8	.064	[3].059
10	.101	.096
12	.116	[4].125

[1] Irradiated in Atlas SMC–R Weather-Ometer at 49 °C and 40 percent R.H. for time periods indicated.
[2] Based on a 25 μ microtome slice from surface of 625 μ asphalt film.
[3] Irradiated for 7.5 hr.
[4] Average of three values, 0.148, 0.085, and 0.132.

4.3. Depth of Photooxidation in Asphalt

In a separate experiment employing the microtome, asphalt specimens were exposed to carbon-arc radiation for 10 hr at 49 °C and 40 percent R.H. A 10 μ slice was removed from the surface and then a second slice of 25 μ thickness removed. The initial carbonyl absorbance (1700 cm^{-1}) of this second film, i.e., 10 to 35 μ below the exposed surface, was not significantly different from films of unexposed asphalt 6 prepared in the usual manner [10]. The implication presented is that photooxidation of asphalt is apparently negligible at depths of >10 μ from the surface. This is in agreement with the conclusions of Dickinson et al., [34].

The authors express their appreciation to S. H. Greenfeld, Research Associate, Asphalt Roofing Industry Bureau, who kindly furnished the asphalt samples and physical property data on the asphalt fluxes.

5. References

[1] D. Hadzi, Fuel **32,** 112 (1953).
[2] R. A. Friedel and J. A. Queiser, Anal. Chem. **28,** 22 (1956).
[3] J. Knotnerus, J. Inst. Petrol. **42,** 355 (1956).
[4] J. E. Stewart, J. Res. NBS **58,** 265 (1957) RP2759.
[5] H. E. Schweyer, Anal. Chem. **30,** 205 (1958)
[6] J. W. Romberg, S. D. Nesmith, and R. N. Traxler, J. Chem. Eng. Data **4,** 159 (1959).
[7] B. D. Beitchman, J. Res. NBS **63A** (Phys. and Chem.) No. 2, 189 (1959).
[8] T. F. Yen and J. G. Erdman, Div. Petroleum Chem. (ACS) Preprint **7,** 5, March 1962.
[9] S. H. Greenfeld and J. R. Wright, Materials Research and Standards **2,** 738 (1962).
[10] J. R. Wright and P. G. Campbell, J. Appl. Chem. (London) **12,** 256 (1962).
[11] P. G. Campbell, J. R. Wright, and P. B. Bowman, Materials Research and Standards **2,** 988 (1962).
[12] J. R. Wright, P. G. Campbell, and T. L. Fridinger, ASTM Preprint No. 88A, 1963.
[13] S. Siggia, Abstracts of Papers, 139th Meeting (ACS), St. Louis, Mo., 24B (Mar. 1961).
[14] L. J. Bellamy, The infrared spectra of complex molecules, 2d ed., p. 152 (John Wiley & Sons, Inc., New York, N.Y., 1958).
[15] Ibid., p. 128.
[16] N. B. Colthup, J. Opt. Soc. Am. **40,** 397 (1950).
[17] H. W. Thompson and P. Torkington, J. Chem. Soc., 640 (1945).
[18] E. R. Blout, M. Fields, and R. Karplus, J. Am. Chem. Soc. **70,** 194 (1948).
[19] M. St. C. Flett, J. Chem. Soc., 962 (1951).
[20] Bellamy, op. cit., p. 191.
[21] O. D. Shreve, M. R. Heether, H. B. Knight, and D. Swern, Anal. Chem. **22,** 1948 (1960).
[22] J. R. Wright and P. G. Campbell, Ind. Eng. Chem., Prod. Res. Develop. (in press).
[23] J. M. Goppel and J. Knotnerus, Proc. Fourth World Petrol. Congr., sec. III/G, 399 (1955).
[24] S. H. Greenfeld, J. Res. NBS **64C** (Engr. and Instr.) No. 4, 287 (1960).
[25] R. S. Winniford and M. Bersohn, Div. Fuel Chem. (ACS) preprint, Sept. 1962.
[26] R. N. Traxler, Asphalt, Its Composition, Properties and Uses, p. 25 (Reinhold Publishing Corporation, New York, N.Y., 1961).
[27] E. J. Barth, Asphalt, Science and Technology, pp. 148–9, 391–2 (Gordon and Breach, Science Publishers, New York, N.Y., 1962).
[28] S. Siggia, Quantitative Organic Analysis via Functional Groups, 2d ed., pp. 46–7 (John Wiley & Sons, Inc., New York, N.Y., 1954).
[29] R. L. Shriner, R. C. Fuson, and D. Y. Curtin, The Systematic Identification of Organic Compounds, 4th ed., p. 152 (John Wiley & Sons, Inc., New York, N.Y., 1956).
[30] P. Ausloos and R. E. Rebbert, J. Phys. Chem. **67,** 163 (1963).
[31] S. H. Greenfeld, Ind. Eng. Chem., Prod. Res. Develop. (in press).
[32] Bellamy, op. cit., p. 8.
[33] A.S.T.M. Tentative Recommended Practice for Accelerated Weathering of Bituminous Materials (D529–59T), 1961 Book of A.S.T.M. Standards, Part 4, 1233.
[34] E. J. Dickinson, J. H. Nicholas, and S. Boas-Traube, J. Appl. Chem. (London) **8,** 673 (1958).

(Paper 68C2–157)

JOURNAL OF RESEARCH of the National Bureau of Standards—C. Engineering and Instrumentation
Vol. 68C, No. 2, April–June 1964

Publications of the National Bureau of Standards*

Selected Abstracts

Dielectric behavior of the film formed on mica cleaved in moist air, S. Ruthberg and L. Frenkel, *J. Res. NBS* **68A** (*Phys. and Chem.*), *No. 2, 173–183 (Mar.–Apr. 1964), 70 cents.*
Water absorbed on a freshly peeled mica crystal causes the loss tangent, D, to increase by 1 to 2 orders of magnitude. The nature of the film is investigated as a function of relative humidity by the measurement of D for the frequency range 100 to 50,000 c/s with a capacitor geometry comprising concentric, parallel electrodes of different diameter on opposite sides of the dielectric sheet. This geometry is then analyzed as consisting of the two regions of that within the plates where E is normal to the dielectric plane and that at the edge where tangential E exists. The first is considered in terms of an equivalent circuit for a two layered dielectric. The second is considered in terms of transmission line concepts. It is predicted and verified that the adsorbed film causes the first components to vary as $1/t$ and the second as $\sqrt{t}$ where t is the thickness of the crystal. Numerical solutions are used to derive the behavior of Δ, R, and C of the adsorbed film itself. D for the normal direction is $\sim$ 0.4 and follows a frequency dependency like fresh snow. Resistivities normal to and parallel to cleavage are considerably different while C is much less than expected for a surface film. It is suggested that the surface film is not continuous but instead is localized in patches.

On the measurement of dielectric losses and surface conductivity of dielectrics in parallel plane test capacitors, L. Frenkel, *J. Res. NBS* **68A** (*Phys. and Chem.*), *No. 2, 185–188 (Mar.–Apr. 1964), 70 cents.*
Thin slabs of dielectric materials are often tested for their dielectric properties in plane parallel plate condensers. When surface conductivity is present, as for instance in freshly split mica, losses not connected with the bulk of the material arise. The present paper deals with the general theory of such measurements. The system is reduced to an assembly of lumped elements superimposed on distributed transmission lines. The treatment includes the presence of possible airgaps underneath the plates of the test condenser. It is shown that such losses depend on the reciprocal square root of the frequency. Losses due to this effect cannot be eliminated by guard ring measurement and much of the published data on the losses in mica must be reexamined in the light of the present work. Similar considerations may apply in the case of other materials.

Second spectrum of tungsten (W II), D. D. Laun, *J. Res. NBS* **68A** (*Phys. and Chem.*), *No. 2, 207–252 (Mar.–Apr. 1964), 70 cents.*
A preliminary report on the second spectrum of tungsten, published in 1938, presented 27 even energy levels and 50 odd energy levels that were derived from 500 W II lines ranging in wavelength from 1961.43 Å to 4348.13Å. The present paper submits data on 62 even levels, 132 odd levels, and 2,150 classified lines of W II, ranging in wavelength from 1756.6 Å to 6219.77 Å. The ground state of the W^+ ion is represented by the $^6D_{\frac{1}{2}}$ level of a sextet D term arising from the $5d^6 6s^1$ electron configuration, but the level intervals and magnetic splitting factors indicate considerable departure from LS-coupling, suggesting that jj-coupling or intermediate coupling may be more appropriate for the W II spectrum.

Optimal matchings, and degree-constrained subgraphs, A. J. Goldman, *J. Res. NBS* **68B** (*Math. and Math. Phys.*), *No. 1, 27–29 (Jan.–Mar. 1964), 75 cents.*
The characterization of maximum-cardinality matchings in linear graphs, by the nonexistence of augmenting paths, has been extended by several authors to a similar characterization of maximum degree-constrained subgraphs. This paper contains a proof of the extended version by direct reduction to the case of matchings. Possible algorithmic implications of the reduction are suggested.

Gaussian wave functions for polyatomic molecules: integral formulas, M. Krauss, *J. Res. NBS* **68B** (*Math. and Math. Phys.*), *No. 1, 35–41 (Jan.–Mar. 1964), 75 cents.*
Explicit formulas are given for the molecular coulomb integrals that arise for all Gaussian basis functions. These results should expedite computational efforts with these basis functions.

Some basic microwave phase shift equations, R. W. Beatty, *Radio Sci. J. Res. NBS USNC–URSI* **68D**, *No. 4, 345–354 (Apr. 1964), $1.00.*
The phase differences between terminal variables (voltage, current, or traveling wave types) at the output with respect to similar ones at the input of a 2-port are expressed in terms of the scattering coefficients of the 2-port and of the reflection coefficients of the system into which it is inserted.
A variety of phase shifts may be defined for a given 2-port, depending upon which of the terminal variables are considered, whether or not generator and load reflection coefficients are assumed to vanish, and in which direction the 2-port has been inserted into the system.
It is shown that a reasonable choice for one of the two "characteristic" phase shifts of a 2-port is ψ_{21}, the argument of S_{21}, one of the scattering coefficients. It follows that the other "characteristic" phase shift is ψ_{12}. The corresponding change in characteristic phase shift for variable phase shifters is the change in either ψ_{12} or ψ_{21} (whichever is appropriate) from the initial to the final setting.
Ideal phase shifters are discussed, and expressions for the change in output level of variable phase shifters are given. The importance of using a nonreflecting system in phase shift measurements is emphasized.

A simplified theory of diffraction at an interface separating two dielectrics, J. Kane and S. N. Karp, *Radio Sci. J. Res. NBS/USNC–URSI* **68D**, *No. 3, 303–310 (Mar. 1964), $1.00.*
Many electromagnetic problems involving more than one dielectric medium are not susceptible of an exact solution, when the appropriate boundary conditions are considered. The purpose of the present paper is to formulate a new boundary condition, which is capable of leading to mathematically tractable problems, with limited sacrifices in accuracy.

On the long term phase stability of the 19.8 kc/s signal transmitted from Hawaii, and received at Boulder, Colo., A. H. Brady, *Radio Sci. J. Res. NBS/USNC–URSI* **68D**, *No. 3, 283–289 (Mar. 1964), $1.00.*
The use of VLF signals for intercontinental frequency comparison has become very popular in recent years, and it has been shown by other workers that a precision of about 2 parts in 10^{11} can be achieved with measurements over a 24 hr period. Phase records made at Boulder, Colo. of the NPM, Hawaii, 18.6 kc/s transmission have been studied for several periods of nearly two weeks duration in 1962. Deviations from an assumed linear frequency difference between the transmitter and receiver oscillators show an attainable precision of 2.5 parts in 10^{11} in a 24 hr observation, extending to 3.1 parts in 10^{12} in a 192 hr observation. Without further data on the remaining differences between the oscillators, there is no evidence that the propagation conditions over the path are limiting this precision. It is pointed out that the 50° (peak to peak) semiannual variation in the day to night change in phase, if attributed entirely to one level of reflection, would have an effect on precision of frequency comparison of about 1 part in 10^{12}.

Precise phase and amplitude measurements on VLF signals propagated through the Artic zone, F. H. Reder, C. J. Abom, and G. M. R. Winkler, *Radio Sci. J. Res. NBS/USNC–*

URSI **68D**, *No. 3, 275–281 (Mar. 1964), $1.00.*
The scope and purpose of an Arctic VLF propagation study are outlined, and results are presented for the period from February to June 1963. Typical diurnal phase and amplitude patterns of NPM and NPG transmissions received at Stockholm are given for each month. The diurnal NPG amplitude change at Stockholm reached a maximum of 38 db during March. Monthly averages of NPM-Stockholm and NPG-Stockholm diurnal phase changes are compared with those for other transmission paths. Twenty-four hour averages of frequency differences of VLF transmissions were measured at various reception sites and intercompared. Residual errors ranged from 10^{-11} to 3×10^{-12}, with standard deviations between 8.5 and 3.3 $\times$ 10^{-11}. Arctic paths were found to be worse by only a factor of about 2. Preliminary analysis of geomagnetic disturbance data and observed VLF phase anomalies indicates reasonable correlation for the NPG-Stockholm path. Finally, phase measurements on NBA taken simultaneously at Kiruna and Stockholm are compared. An SCNA event recorded by a Kiruna riometer clearly coincided with an NBA phase anomaly observed at Kiruna while the Stockholm NBA phase record showed no anomaly.

A light-modulated scattering technique for diffraction field measurements, A. M. Vural and D. K. Cheng, *Radio Sci. J. Res. NBS/USNC–URSI* **68D**, *No. 4, 355–362 (Apr. 1964), $1.00.*
This paper describes a scattering method for measuring microwave diffraction fields using light modulation. A small photoelectric cell is suspended in the field as a scatterer, upon which light pulses shine at an audio rate. Only the signal scattered back by the scatterer is modulated. A coherent detector is used which has an output voltage proportional to the square of the tangential component of the field under measurement. Since this method dispenses with all electrical connections to the scatterer, circuit complications and sources of error due to connection disturbance and scatterer movement are eliminated. Hitherto unavailable extensive data for the near-zone diffraction fields of finite cones are presented.

Propagation of electromagnetic waves through a continuously varying stratified anisotropic medium, G. H. Price, *Radio Sci. J. Res. NBS/USNC–URSI* **68D**, *No. 4, 407–418 (Apr. 1964), $1.00.*
Expressions are developed for the transmission and reflection coefficients for propagation of a plane wave through a layered medium, taking account of the effects of the static magnetic field. A matrix formulation is used which allows proceeding to the limit of a continuously varying medium, and series expansions of the fields for this case are developed. The results are expected to have application to interpretation of VLF data obtained within and above the lower ionosphere.

Methods for the dynamic calibration of pressure transducers, J. L. Schweppe, L. C. Eichberger, D. F. Muster, E. L. Michaels, and G. F. Paskusz, *NBS Mono. 67 (Dec. 12, 1963), 60 cents.*
This Monograph is designed to assist the practicing engineer faced with the problem of making dynamic measurements and calibrations of the rapidly changing pressures in missiles and space vehicle technology.
In order to calibrate and use dynamic pressure transducers, the practicing engineer needs to be familiar with (1) the characteristic differential equations and their solutions, (2) the methods of analyzing pairs of input and output functions to determine the transfer function and the frequency response curve, (3) the methods of generating precise input functions, and (4) the specific methods for using precise experimental measurements to determine the dynamic characteristics of a particular pressure transducer.

Compilation of the melting points of the metal oxides, S. J. Schneider, *NBS Mono. 68 (Oct. 10, 1963), 25 cents.*
A compilation has been made of the melting points of 70 metal oxides published prior to January 1963. Both the original melting point and the equivalent value based on the International Practical Temperature Scale of 1948 are presented. Included in the survey is information on pertinent experimental details such as the method of temperature measurement, purity, furnace type, and environmental conditions.

Weights and measures standards of the United States, a brief history, L. V. Judson, *NBS Misc. Publ. 247 (Oct. 1963), 35 cents. (Supersedes Sci. Pap. 17 and Misc. Publ. 64.)*
A historical account is given of the standards of weights and measures of the United States from the time of the American Revolution through the year 1962. Current and historical standards of length and mass now in the possession of the National Bureau of Standards are listed and described.

Calibration and test services of the National Bureau of Standards, *NBS Misc. Publ. 250 (Nov. 22, 1963), 70 cents.*
This publication is a listing of the numerous calibration and testing services provided to science and industry by the National Bureau of Standards. The Bureau promotes accuracy and uniformity of measurement through its program of measurement services, including the calibration and testing of standards and standard instruments. An up-to-date listing of the Bureau's calibration and test fee schedules was printed in recent issues of the Federal Register, with a large proportion of the fees being changed at that time. This publication contains all of this material, but in larger, more legible type, and fully indexed. Besides listing all NBS calibration services and their cost, the publication includes a statement of the Bureau's statutory functions, testing policy, and routine for securing the Bureau's calibration and test services—from original request to the reporting and use of test results.

Bibliography on ignition and spark-ignition systems, G. F. Blackburn, *NBS Misc. Publ. 251 (Nov. 22, 1963) 15 cents. (Supersedes NBS Circ. 580).*
Approximately 730 references to books, papers, and reports are listed on ignition of combustible gaseous mixtures and ignition apparatus. The ignition of gases includes ignition by electric sparks and arcs and by hot surfaces. The references on ignition apparatus are for the most part on ignition systems and components on internal-combustion engines, with spark plugs listed separately from other components.

Survey of the literature on safety of residential chimneys and fireplaces, H. Shoub, *NBS Misc. Publ. 252 (Dec. 17, 1963), 15 cents.*
A search was made of recent technical literature on chimneys and fireplaces to determine what information was available on questions concerning their safety from fire hazard. The survey covered types of construction and materials proposed or currently in use with several types of fuel. The reports included investigations of heat transmission through chimney and fireplace walls, the effects of thermal shock on flue materials, and the required spacing of combustibles from the heated walls. The bibliography presented contains brief reviews of some of the works.

Recommended unit prefixes; Defined values and conversion factors; General physical constants, *NBS Misc. Publ. 253 (Oct. 1963), 5 cents (wallet-size plastic card).*
Wallet-size pocket card listing selected general physical constants recommended by the National Academy of Science-National Research Council and adopted by the National Bureau of Standards. Units are given in both the centimeter-gram-second System and the International System (MKSA). Reverse side lists unit prefixes recommended by International Committee on Weights and Measures and adopted by the National Bureau of Standards. Also lists defined values and conversion factors for several commonly used measurement units.

Photometry of projectors at the National Bureau of Standards, L. Chernoff, *NBS Tech. Note 198 (Dec. 17, 1963), 25 cents.*
A projector consists of a light source and optical system which produces a beam of light. In the photometry of projectors, the intensity of the projector as a function of angle of viewing is measured. For many years the National Bureau of Standards has conducted photometric tests on various types of projectors, and a variety of techniques and equipment has correspondingly been developed.

Photometric testing is carried out on a photometric range of which there are two at NBS: a short range on which the test distance may be varied up to a maximum of 30 meters and a longer range with a fixed test distance of 279 meters. Photometric measurements are made by comparison with a standard lamp of known luminous intensity in a specified direction. These comparisons are made with photosensors which are color-corrected by filters so that the spectral response is similar to the CIE luminous efficiency function. While precision requirements are not severe, considerable care is required to keep the experimental errors within the desired limits.

Carbon resistors for cryogenic liquid level measurement, R. C. Muhlenhaupt and P. Smelser, *NBS Tech. Note 200 (Oct. 9, 1963), 25 cents.*
Data are shown in graphical form. One set of plots presents resistance ratio R_O/R_L as a function of "warming up" time at various levels of constant power dissipation. A second set of plots presents resistance ratio R_L/R_O as a function of nominal resistance at various levels of constant power dissipation.
The use of the data and the design of a practical liquid level indicator are discussed in the appendix.

A technique for extrapolating the 1 kc values of secondary capacitance standards to higher frequencies, R. N. Jones, *NBS Tech. Note 201 (Nov. 5, 1963), 15 cents.*
A simple technique is described for extrapolating the 1 kc values of certain two-terminal capacitors to higher frequencies without incurring serious losses in accuracy. The method is intended for use with air capacitors having binding post or banana plug type connectors. Because of inherent errors, such connectors are not appropriate for measurement where the highest accuracy is required. For this reason, it is recommended that calibration of this type be performed by secondary laboratories and not be submitted to the National Bureau of Standards.

BOUMAC, A macro-programming system for scientific computation, J. H. Devenney and J. J. Sopka, *NBS Tech. Note 203 (Dec. 18, 1963), 30 cents.*
The BOUMAC computing system will allow a scientist having no programming knowledge to perform the more commonly used macro computations such as matrix operations, solution of linear equations, numerical integrations, curve fitting, statistical analyses, etc., using a high-speed electronic computer. The scientist needs only to know the various mathematical operations which are required to obtain the information he wants from the data and to learn to use a simple code with which to specify these mathematical operations.

The normal phase variations of the 18 kc/s signals from NBA observed at Frankfurt, Germany, A. H. Brady, A. C. Murphy, and D. D. Crombie, *NBS Tech. Note 206–1 (Dec. 8, 1963), 25 cents.*
Observations of the normal phase variations of the 18 kc/s signals radiated from the Canal Zone and received in Frankfurt, Germany are given in the form of monthly averages and standard deviations at 5 minute intervals. The relation between mean diurnal phase variations and the diurnal variation in path illumination is shown. The mean diurnal height change is 21 km which is reduced to 20 km during summer and winter and increased to 22 km during the equinoxes. Short term normal phase differences are also briefly discussed.

Solar heating, radiative cooling, and thermal movement—their effects on built-up roofing, W. C. Cullen, *NBS Tech. Note 231 (Dec. 16, 1963), 25 cents.*
Twenty different built-up roof construction specimens, covered with five surfacing materials, were subjected to natural solar heating and nighttime cooling. The temperatures and temperature changes observed during winter and summer exposures are discussed. The data indicate that the temperature attained in a roof membrane is influenced by the absorptance and emissibity of the surface as well as the thermal and physical properties of the substrate to which the roofing is applied. The data show that roofings placed over insulation may be heated to a temperature of 80° F. above ambient due to solar heating and may be subcooled as much as 20° F. below the ambient due to radiative cooling. The thermal movements which occur in the components of a roof system due to temperature change are discussed in relation to built-up roof performance and failures. Thermal expansion data are presented for some composite bituminous membranes. The data show that these membranes undergo greater thermal movements than most other components of a roof system and the rate of expansion is not linear but decreases as the temperature is increased.

Steel spirals for reinforced concrete columns, *SPR53–63 (Oct. 1, 1963), 10 cents.*
Establishes as a standard of practice in production, distribution, and use the sizes of steel spirals used for concrete column reinforcement in the building industry. The standard establishes three standard sizes of steel bars and wire used for spirals, and includes a table listing the recommended pitches in multiples of ½ inch for spirals with core diameters from 11 to 39 inches inclusive for varying percentages of spiral reinforcement. Definitions of several terms applicable to steel spirals are also included.

Vises (machinists' and other bench-mounted vises), *SPR229–63, 10 cents. (Supersedes R229–48).*
Establishes a standard of simplified practice for the various kinds, types, and sizes of bench-mounted vises. The products listed are currently in general use and demand, and are considered to afford an adequate selection for ordinary purposes. Accordingly, they are recommended as standard stock items.

Grading of a diamond powder in sub-sieve sizes, *CS261–63, 10 cents. (Supersedes in part CS123–49).*
Provides a nationally recognized standard for the sizing of diamond powder in sub-sieve (micron) sizes and a uniform method of determining conformance with the size designated. It serves as a common basis for understanding between purchasers and sellers as to the quality and particle size desired or supplied, and thereby should promote fair competition.

Absolute calibration of the National Bureau of Standards photoneutron source: III. Absorption in a heavy water solution of manganous sulfate, R. H. Noyce, E. R. Mosburg, Jr., S. B. Garfinkel, and R. S. Caswell, *J. Nucl. Eng.* **17,** *No. 7, 313–319 (1963).*
The neutron emission rate for the National Bureau of Standards radium-beryllium (γ, n) standard source (NBS-I) has been redetermined by a relative comparison to an antimony-beryllium source which had been calibrated absolutely in a heavy water manganous sulphate solution through an indirect method involving $4\pi\beta=\gamma$ coincidence counting of the induced Mn^{56} activity. Correction was made for absorption of neutrons by other elements present in the bath. The emission rate of NBS-I was found to be $1{\cdot}25_2 \times 10^6$ n/sec as of June, 1961 with an uncertainty of 1 per cent. This measurement, when suitably averaged with previous determinations (DeJuren, Padgett and Curtiss, 1955; DeJuren and Chin, 1955) yields the best value $1{\cdot}25_7 \times 10^6$ n/sec with an uncertainty of 1 per cent.

Determination of differential x-ray photon flux and total beam energy, H. W. Koch and J. S. Pruit, *Ed. L. C. Yugan and C. Wu, Nucl. Phys.* **5,** *ch. 2. 8. 2, 508–553 (1963).*
The electron impact spectra of helium and ethylene are measured at 50 volts primary energy and in the straight ahead direction. Under these conditions the spectra are analagous to the ultraviolet absorption spectra. It is concluded that previously reported deviations are due to the high angle collection geometry rather than the low voltage.

Metallurgical microanalysis with the electron probe, J. R. Cuthill, L. L. Wyman, and H. Yakowitz, *J. Metals AIME* **15,** *No. 10, 763–768 (Oct. 1963).*
The electron probe microanalyzer that was designed and built at the National Bureau of Standards is described, the functional design considerations involved are discussed, and the long-felt need for such an instrument in the metallurgical field is reviewed.

The electron probe microanalyzer makes possible for the first time the quantitative chemical analysis of microconstituents *in situ* in an alloy, and provides a convenient method for determining the concentration gradients across an alloy structure.
The NBS electron probe microanalyzer employs a normal incidence, high-resolution optical system concentric with the axis of the electron beam. It is equipped with two scanning X-ray spectrometers with a capability of analyzing for all of the elements from Mg to U, if they can be suitably contained in a vacuum.
The application of the NBS electron probe to two investigations, representative of those carried out thus far, is discussed. Additional features and modifications to the NBS electron probe, to be incorporated in the near future, are described.

Heating rate as a test of adiabatic calorimeters and the heat capacity of α alumina, E. D. West, *Trans. Faraday Soc.* **59**, *No. 489, pt. 9, 220–2203 (Sept. 1963).*
The constancy of heat capacities measured in an adiabatic calorimeter at different heating rates does not demonstrate the absence of heat leak errors due to departures of the surface temperature from the "isothermal" condition. On the contrary, the total heat exchange between the calorimeter and its shield is virtually independent of the heating rate. The tests tend to obscure a real source of error due to the variation in the total heat exchange between experiments with the empty and the full calorimeter.

A new standard of spectral irradiance, R. Stair, W. E. Schneider, and J. K. Jackson, *Appl. Opt.* **2**, *No. 11, 1151–1154 (Nov. 1963).*
The National Bureau of Standards has made available a new standard of spectral irradiance in the form of a 200-watt quartziodine lamp with a coiled-coil tungsten filament operating at about 3000° K and calibrated over the spectral range of 0.25 to 2.6 microns. The calibration of this standard is based upon the radiance of a blackbody as defined by the Planck law of radiation since it was done by comparisons with the NBS standards of spectral radiance, of luminous intensity, and of total irradiance, each of which was established through the use of blackbodies. This standard is used without auxiliary optics. Because of its small physical size and high operating temperature, relatively high spectral irradiances may be obtained through its use.

Intercomparisons of the standard thermal-neutron flux density of the National Bureau of Standards, W. M. Murphey and J. Chin, (*Proc. Symp. Neutron Detection, Dosimetry and Standardization, International Atomic Energy Agency, Atomic Energy Research Establishment, Harwell, England, Dec. 10–14, 1962*), *Book, Neutron Dosimetry* **II**, *513–521 (International Atomic Agency, Vienna, 1963).*
The standard thermal neutron flux maintained at the National Bureau of Standards since 1951 consists of two radium-beryllium (α,n) sources in a geometry of lead, paraffin and carbon. The flux has been absolutely measured twice by NBS; once in terms of the absorption cross section of boron, and once in terms of the absorption cross section of gold (1,2). A neutron flux with a cadmium ratio of about 7 (for 40 mg/cm² gold foils and 0.040 inch cadmium covers) and a conventional thermal neutron flux density of 4231 (Apr. 62) neutrons per cm² per second was obtained. It has also been absolutely measured twice through the intercomparison program; once by NPL, UK and once by PTB, Federal Republic of Germany.
The agreement between most laboratories at present is about 1.5%. This is in addition to the uncertainty in the absolute measurement which is about 1.5% or more for each laboratory. Intercomparisons of NBS with CEA, France; Oak Ridge National Laboratory, USA; Electrotechnical Laboratory, Japan; National Physical Laboratory, UK; and Physikslisch-Technische Bundesanstalt, Federal Republic of Germany will be shown.

Interpretation of *p*H measurements in alcohol-water solvents, R. G. Bates, M. Paabo and R. A. Robinson, *J. Phys. Chem.* **67**, *1833–1838 (1963).*
The operational *p*H numbers for solutions in alcohol-water solvents obtained from the e.m.f. of the cell with hydrogen (or glass) electrode, salt bridge, and calomel reference electrode, standardized with aqueous buffer standards, are subject to no simple interpretation. Because of the indeterminate potential at the junction solution X (alcohol-H_2O) |KCl bridge (aq.), they do not lie on a conventional scale of hydrogen ion activity referred either to the aqueous standard state (pa_H) or to the standard state in the alcoholic medium (pa_H*). Values of $\bar{E}_j + \log {}_{m_\gamma Cl}$ (where $\bar{E}_j$ is the liquid-junction potential expressed in *p*H units and ${}_{m_\gamma Cl}$ is the primary medium effect of chloride ion) were found to be as constant for different buffer solutions in alcoholic solvents of fixed composition as for the strictly aqueous medium. Inasmuch as ${}_{m_\gamma Cl}$ at a given temperature is dependent only on solvent composition, the liquid-junction potential must therefore also be nearly constant for a given solvent mdeium. Correction terms $\bar{E}_j - \log {}_{m_\gamma H} = \delta$ have been calculated, and it is shown that $p\mathrm{H} - \delta$ closely approximates pa_H* under optimum conditions of measurement. An operational scale of *p*H* (which is related to pa_H* in the same way that *p*H is related to pa_H) is described. Values of pa_H* were obtained for 12 solutions in methanol-water solvents (0 to 68.1 wt. % MeOH) and for 3 solutions in ethanol-water solvents (0 to 100% EtOH).

The error rate in a multiple-frequency shift system and the output signal/noise ratio in a frequency modulation and a pulse-code-modulation/frequency-shift system, H. Akima, *Intern. Conf. Satellite Communication, London, Nov. 22–28, 1963, pp. 305–309 (Programme and Conference Digest, London, England, 1963).*
Based on the assumption of a fading-free signal and an additive white Gaussian noise, the element and symbol error rate in an MFS (multiple-frequency-shift) system and the output SNR (signal-to-noise ratio) in an FM (frequency-modulation) and a PCM-FS (pulse-code-modulation-frequency-shift) system are evaluated for wide ranges of system parameters. It is shown that the required intrinsic SNR for a given symbol error rate in an MFS system can be reduced by increasing the number of frequencies in the keying. The possibility of improving the threshold of an FM system beyond that of a conventional one by frequency modulating the carrier with sampled values and demodulation the modulated wave with a band-dividing demodulator is shown. A brief discussion on the threshold effects in the frequency-lock and phase-lock FM demodulators suggest that the threshold of these feedback demodulators cannot be improved beyond that of a band-dividing one. It is shown that the threshold in a PCM-FS system can be reduced by increasing the base in the coding. The comparison of a PCM-FS system with a band-dividing FM system shows the inferiority of the former to the latter, insofar as the minimum-power criterion of system comparison is concerned.

A study of stress relaxation with finite strain, B. Bernstein, E. A. Kearsley, and L. J. Zapas, *Trans. Soc. Rheology* **VII**, *391–410 (1963).*
Two simple types of constitutive equations appropriate to materials exhibiting elasticity are presented, one of a basic solid nature and one of a basic fluid nature. The predictions of the equations for a stress relaxation experiment are worked out and compared to the data from some experiments on various elastomers. The fluid theory is shown to be most appropriate in a certain sense.

Experimental evaluation of a thallium beam frequency standard, R. E. Beehler and D. J. Glaze, *Proc. 17th Annual Frequency Control Symp. (1963).*
A thallium atomic beam frequency standard has been in operation at the National Bureau of Standards since September 1962. An evaluation of the system has been conducted in an effort to determine whether the use of thallium will result in a substantially improved atomic frequency standard. The thallium system is a modified version of NBS I, the original Cs beam.
The preliminary measurements show that, as expected, the existing uncertainties associated with the uniform Magnetic C field produce a corresponding uncertainty in the frequency measurements of only a few parts in 10^{+13}. Measurement precision has been determined from the reproducibility and statistical analysis of comparison data between the thallium standard and the USFS, NBS II. However, day-to-day

variations in the earlier comparisons are significantly larger than one would expect from the statistics. Possible sources of this difficulty along with improvements and the most recent data available are discussed.
The best measured values for the frequency of the thallium resonance in terms of cesium are given and compared with that published by Dr. Bonanomi's group at Neuchatel, Switzerland.

Some factors affecting the creep behavior of an age-hardenable alloy, W. D. Jenkins and W. A Willard, *Trans. Quart. ASM* **56,** *No. 3, 427–441 (Sept. 1963).*
The effect of hardening, due to alloying and to precipitation preceding and during testing, on the creep behavior and the effect of creep on the hardening characteristics of a 94 percent nickel—4.25 percent aluminum alloy (Duranickel) at 700, 900, and 1200° F are discussed. Alloying nickel with 4.25 percent aluminum increased the creep strength of the annealed metal by as much as 7-fold. This factor was further increased by aging prior to testing. However, the strength ratio (σ Duranickel/σ nickel) decreased as the temperature was decreased or the creep rate increased. Although no single equation could describe the stress-creep rate or fracture time relations, the shape of these curves was dependent on both temperature and initial condition of the alloy. Furthermore, the second stage creep rates were inconsistent indices of the fracture times. The ductility of the alloy was signficantly affected by prior aging, test temperature and creep rate. Photomicrographs, illustrating types of fractures, intersecting, wavy and straight slip bands, twinning, recrystallized grains, and the density and distribution of (Ni_3Al) precipitates, are presented to assist in the analysis of the modes of deformation occurring under differing test conditions.

Measurement of weak magnetic fields by optical pumping methods, P. L. Bender, *Bull. Ampere* **9**e, *pt. II, 261–628 (1960)*
Three new types of magnetometer, the dc alkali vapor magnetometer, the self-oscillating alkali vapor magnetometer, and the helium magnetometer, all based on optical pumping, are compared. Practical limitations and performance in various environmental circumstances are considered.

Use of transistors in Van de Graaff source leak controls, A. C. B. Richardson and L. Costrell, *Nuclear Instr. Methods Letter to Editor* **24,** *No. 1, 129–130 (July 1963).*
The feasibility of using transistors in the high voltage terminals of pressurized accelerators has been demonstrated in a circuit developed for adjustment of the heater current of palladium leaks for the ion source for Van de Graaff accelerators. Improved resolution and stability, together with trouble free operation have been achieved.

Recent developments in neutron source standardization, R. S. Caswell, R. H. Noyce, S. B. Garfinkel, and E. R. Mosburg, Jr., *(Proc. Symp. Neutron Detection, Dosimetry and Standardization, International Atomic Energy Agency, Atomic Energy Research Establishment, Harwell, England, Dec. 10–14, 1963), Book, Neutron Dosimetry* **II,** *547–555 (International Atomic Energy Agency, Vienna, 1963).*
A new absolute measurement of the neutron emission rate of the U.S. national standard neutron source, a Ra-Fe(γ,n) source has been using a manganous sulfate bath primarily of heavy water, which is less dependent on values of neutron absorption cross sections than previous bath methods. To avoid production of neutrons in the heavy water from D(γ,n) reactions, an Sb-Be(γ,n) source was absolutely calibrated in the heavy water bath, and in turn the standard source was calibrated by a relative comparison to the Sb-Be(γ,n) source in a light water bath. The result of this measurement was a neutron emission rate of $1.24_4 \times 10^6$ neutrons/sec, which when combined with previous measurements gives a best value of $1.25_2 \times 10^6$ neutrons/sec. The estimated uncertainty is 1 per cent.
Measurements of the growth of neutron emission rate in Pu-Be(α, n) sources have shown these sources to have varying rates of growth of neutron emission up to about 2 percent/year. For use as standards, information on isotopic composition or on neutron emission rate growth is required. Am^{241}-Be(α,n) sources offer promise of providing a standard source with characteristics similar to the Pu-Be sources, but without the growth uncertainties.

Some physical properties of organic denture base materials. J. B. Woelfel, G. C. Paffenbarger, and W. T. Sweeney, *J. Am. Dental Assoc.* **67,** *489–504 (Oct. 1963).*
Pertinent physical properties were measured of 12 different types of organic denture base materials used in the fabrication of technic and clinical dentures which had been under observation for from three to four years. The cold-curing acrylic resins, the weakest and the most flexible did not fracture or distort in use. The polystyrene resin, the strongest and least flexible fractured in two out of five upper dentures. It is surmised that these fatigue-like fractures were caused by a high residual stress imparted during molding. The repaired resins had 40–71% of their original strength. The Izod impact strength ranged from 0.17 (heat-curing acrylic resins) to 1.65 ft.-lb. per inch of notch (glass fiber filled acrylic resins). Indentation tests showed the polystyrene to be the hardest. The coefficients of linear thermal expansion of "wet" specimens run at 20–37° C. ranged from 42.7×10^{-6}/°C for glass-fiber-filled acrylic resins to 98.3×10^{-6}/°C for a heat-curing acrylic resin copolymer of the powder-liquid type. Both laboratory and clinical tests are needed in the evaluation of denture base resins.

Dependence of power output of a gas laser on the length and rate of excitation of the discharge, J. A. White, *Appl. Phys. Letters* **3,** *No. 7, 107–109 (Oct. 1, 1963).*
The gain and emittance of a gas laser are calculated from first principles for the case that the atoms in the gas interact appreciably with only a single Doppler-shifted component of the radiation. Good agreement is obtained with the experimentally observed output of a laser operating simultaneously in several modes. Although the theory does not take into account interference effects when the same atoms are perturbed appreciably by different modes of oscillation or different Doppler components of the same mode, it is otherwise applicable for arbitrarily high field intensities.

The adsorption of methane and nitrogen on silica gel, synthetic zeolite and charcoal, A. J. Kidnay and M. J. Hiza, *J. Phys. Chem.* **67,** *1725–1727 (1963).*
The data obtained in this study provide a characterization of the temperature dependence of methane adsorption near the boiling point of liquid nitrogen and a comparison of the adsorption isotherms of methane and nitrogen on three commercial adsorbents. Isosteres of nitrogen on silica gel and methane on silica gel, charcoal and a synthetic zeolite from 70° to 82°K are presented; in addition isotherms for methane and nitrogen on all three adsorgents at 76°K are presented. The isosteres were used to calculate some thermodynamic properties of these systems.

Galvanostalametry, a new technique based on the negative pressure of liquids, for investigating electrochemical phenomena at an electrode, J. Sligh and A. Brenner, *J. Electrochem. Soc.* **110,** *No. 11, 1136–1142 (Nov. 1963).*
A procedure based on the negative pressure of water has been used as a sensitive indicator for the study of electrochemical phenomena. The apparatus consists of a vertical glass tube, closed at the upper end, which is evacuated and filled with an electrolyte. The latter remains suspended in the column in a metastable state of tension. The column of electrolyte was dropped by producing a minute amount of electrolysis between 2 electrodes sealed in the top of the column. The time or current required *to drop the column* (*abbr. t.d.c.*) was used for making the following experiments and/or observations:

A. The decomposition potential of water was determined by observing the lowest applied voltage required t.d.c.
B. The time required t.d.c. (on passage of a constant current) was proportional to the concentration of iodide ion in the electrolyte.
C. The current required t.d.c. was proportional to the area of the indicator electrode, regardless of the irregularity of its shape.
D. The formation of the gas required t.d.c. occurred in less than 15 microseconds after closing the circuit.

Electrical resistance-strain characteristics of thin evaporated metal films, R. L. Parker and A. Krinsky, *J. Appl. Phys.* **34,** *No. 9, 2700–2708 (Sept. 1963).*
The electrical resistance-strain coefficients of thin evaporated films of aluminum, gold, cobalt, nickel, palladium, platinum, antimony, and tellurium have been measured. The coefficients (strain-sensitivity coefficient or "gauge-factor" γ) depend on the specific resistance R_s of the films. For relatively thick films (small R_s), γ tends to approach the bulk value γ_b; for relatively thin films (large R_s), γ may be many times greater than γ_b; for films of intermediate thickness γ has a minimum value. The resistance change was found to be proportional to strain for all the above films except those of Ni and Sb. Some possible mechanisms for the observed behavior are discussed; it is suggested that free-path effects are predominant in films of intermediate thickness, and that the tunneling conduction mechanism plays an important role in producing the high strain sensitivity of very thin (high R_s) films of separated particles.

A 100 megapulse per second binary counter with impedance steering, S. B. Geller and P. A. Mantek, *IEEE Trans. Electronic Computers* **EC–12,** *No. 5, 568 (Oct. 1963).*
This Letter describes a 100 megapulse-per-second triggerable flip-flop or binary counter circuit. It employs transistor-tunnel diode circuitry and has a unique trigger steering mechanism that depends upon the impedance states in the circuit.

Line shapes, saturation behavior, and temperature studies in the nuclear resonance of nickel, R. L. Streever and L. H. Bennett, *Phys. Rev.* **131,** *No. 5, 2000–2009 (Sept. 1, 1963).*
The nuclear magnetic resonance of Ni^{61} has been studied in pure nickel powders. Both natural nickel (1.25% abundant in Ni^{61}) and enriched nickel (99.9% abundant in Ni^{61}) were used. The signal observed with a circuit sensitive to the absorption of power is a combination of absorption and dispersion modes. The amount of mode mixing is found to depend on the applied rf field, ambient temperature, annealing temperature, and external magnetic-field intensity. The mode mixing of the resonance is related to electronic losses in the sample. The saturation behavior of the individual absorption and dispersion modes is that of an inhomogeneously broadened line. From the saturation behavior an estimate of the enhancement of the applied rf level for nuclei in domain walls of about 7×10^3 is made. An additional broadening mechanism is observed in the enriched nickel, particularly at 77°K. Application of Redfield's theory of saturation at high rf levels leads to the conclusion that the additional broadening can be attributed to strong indirect exchange between nuclei. Frequency measurements from room temperature at 4.2°K made with a marginal oscillator in both the enriched and unenriched nickel are presented. A temperature-dependent frequency shift is found between the enriched and unenriched nickel which appears to be a maximum at about 200°K where the enriched nickel frequency is about 30 kc/sec higher. From room temperature to 536°K, frequency measurements made with super-regenerative circuits are reported. A comparison of the temperature dependence of the resonance frequency with the saturation magnetization is made.

Impedance of Leclanché cells and batteries, R. J. Brodd and H. J. DeWane, *J. Electrochem. Soc.* **110,** *No. 11, 1091–1097 (Nov. 1963).*
The impedance, open circuit voltage, short circuit current, performance on standard tests, and the pulse resistance were determined for a number of different size Leclanché cells produced by various manufacturers. The interpretation of the impedance in the light of modern perturbation theory indicated the existence of one process at the negative zinc electrode and two processes at the positive manganese dioxide electrode for all Leclanché cells assuming ideal behavior for each electrode process. The magnitude of the contributions to the total impedance and the relaxation time for each of the electrode processes in the cell were determined. The effect of varying manganese dioxide to carbon black weight ratios on the impedance of laboratory-prepared cells was determined. Also, the impedance of fresh cells and batteries was determined at several stages during discharges on various standard tests, and, in some cases, after shelf stands of up to two years. The extrapolated value of the impedance at infinite frequency, $R\infty$, was used to estimate the residual capacity of cells after shelf stands of one and two years. $R\infty$ was found to be identical with the internal resistance of the cell determined by pulse techniques.

Absolute scale of oscillator strengths, C. W. Allen and C. H. Corliss, *Monthly Notices Roy. Astron. Soc.* **126,** *No. 1, 37–40 (1963).*
Absolute f-values assembled at the University of London Observatory (U.L.O.) using the f-sum rule, and at the National Bureau of Standards (N.B.S.) using experimental values are compared. The systematic logarithmic difference is U.L.O. − N.B.S. = -0.19 ± -0.04 dex. From the discussion it is concluded that either method may be used for obtaining extensive absolute f-values with an accuracy of about ±0.2 dex.

Relation of partial (110) pole figures to thickness and microstructure of electrodeposited copper, F. Ogburn and C. J. Newton, *J. Electrochem. Soc.* **110,** *No. 11, 1148–1150 (Nov. 1963).*
The distributions of (110) poles near the surfaces of two copper electrodeposits are given. The concentration of (110) poles is maximum for $\psi=0°$ and minimum for $\psi=30°$ where ψ is the angle between the (110) pole and the normal to the specimen surface. The specimen that was 1700μ thick showed a much greater concentration near $\psi=0°$ than the thinner deposit of 14μ. A cross-section micrograph of the thicker deposit shows many twinned planes near perpendicular to the deposit surface.

Regulation of ionization gauge emission current to better than 0.05%, K. W. Yee and R. J. Carpenter, *Rev. Sci. Instr.* **34,** *No. 10, 1101–1103 (Oct. 1963).*
A control system is described for regulating the temperature limited emission current from the filament of an ionization gauge tube. A d-c transistor circuit is used with a lamp and a photosensitive resistor to provide electrical isolation between the control and the controlled circuits. Emission currents from 10 mA to 0.05 mA can be maintained with a stability of better than 0.05% with the system.

Errors in "drop" calorimetry due to sample container transitions, D. C. Ginnings, *J. Phys. Chem.* **67,** *1917–1918 (1963).*
An examination was made of three sets of published enthalpy data obtained by using the "drop" method and container materials having transitions. It is concluded that in all three cases, small but significant errors resulted from the use of the container materials with transitions.

Energy dependence of proportional-counter fast-neutron dosimeters, R. S. Caswell, W. B. Beverly, and V. Speigel, Jr., (*Proc. Symp. Neutron Detection, Dosimetry and Standardization, Atomic Energy, Atomic Energy Research Establishment, Harwell, England, Dec. 10–14, 1962*), *Book, Neutron Dosimetry* **II,** *227–237 (July 1963).*
Proportional counter dosimeters with polyethylene walls and ethylene gas filling are widely used for neutron dose measurements in the presence of gamma rays, the radiations being differentiated by pulse-height discrimination. Only pulses larger than a given bias are accepted and pulse-height integrated to determine the neutron dose. In the present work, the energy response of a fast neutron dosimeter with a known bias was measured using known fluxes of monoenergetic neutrons between 0.1 and 4 Mev. The pulse-height distributions were also observed. An approximate calculation has been made which predicts reasonably well the energy dependence of this type of dosimeter. More detailed calculations should be able to predict quite accurately the response of this type of detector.

Projection X-ray microscopy of roofing materials, S. B. Newman and S. H. Greenfeld, *Mater. Res. Std.* **3,** *No. 11, 893–898 (Nov. 1963).*
Point projection microradiography has been used to elucidate the relationship of components in structures containing asphalt. Soft X-rays, in the 8 A range, produced good contrast

in a number of specimens of roofing systems. Low magnifications were adequate for indicating defects and advantages of the materials for the intended applications. The method provides a unique tool for obtaining such information.

A redetermination of some optical properties of calcium fluoride, I. H. Malitson, *Appl. Opt.* **2,** *No. 11, 1103–1107 (Nov. 1963).*

This paper gives refractive-index values at 24°C for a synthetic and a natural prism of calcium flouride. Measurements were made by the minimum-deviation method at 46 calibrated wavelenghts from 0.23 μ in the ultraviolet to 9.7 μ in the infrared. The indices of the synthetic prism were fitted to a three-term Sellmeier dispersion formula of the form: $n^2-1=\Sigma Aj\lambda^2/(\lambda^2-\lambda_j^2)$. Dispersive quantities were computed which estimate the expected relative dispersion, chromatic aberration, and resolution of CaF_2 as a function of wavelength. Valeus of dn/dt are also given. The results of this work are compared with previously reported data.

Calorimetric method for measuring polyester degradation due to weathering, V. E. Gray and J. R. Wright, *J. Appl. Polymer Sci.* **7,** *2161–2174 (1963).*

Chemical changes occurring in thermoset polyesters during exposure to solar and carbon-arc radiant energy were determined quantitatively by a color reaction with a diamine, N,N-dimethyl-*p*-phenylenediamine, in a methanol-benzene solution. The amount of diamine reacting with a specimen and the color change of the treated specimen, as measured by differential reflectance, varied directly with exposure time. Three commercial polyesters (fiberglass reinforced) exposed under identical conditions had widely different degradation rates as measured by the amount of N, N-dimethyl-*p*-phenylenediamine used per specimen. The relative stability of the three materials was independent of irradiation source. The color of the treated specimen was dependent on exposure source.

Optical T-bench method for measurement of optical path difference, F. E. Washer and W. R. Darling, *SPIE J.* **1,** *211–217 (Sept. 1963)*

A visual optical T-bench method for measurement of optical path difference n_λ in units of wavelength is described. The method employs an optical T-bench equipped with nodal slide, a movable double-slit system, and an angle measuring telescope. Determinations of longitudinal spherical aberration in millimeters and optical path difference in units of wavelength are based upon measurements of angular deviations in small selected regions of the collimated beam emergent from the lens under test. The theory of the method is presented together with a description of the apparatus used and the technique of measurements. Results of measurement on a single lens are included.

Programmed maneuver-spectrum fatigue tests of aircraft beam specimens, L. Mordfin and N. Halsey, *ASTM STP Symp. Fatigue Tests of Aircraft Structures, No. 338, 251–272 (Sept. 1963).*

Constant- and variable-amplitude fatigue tests were conducted on 7075–T6 aluminum alloy built-up beam specimens in bending to study certain aspects of spectrum fatigue. Existing cumulative fatigue damage theories were found inadequate for the dual purpose of predicting spectrum fatigue life and evaluating the effects of individual load levels in a spectrum. However, the observed spectrum fatigue properties were consistent with the measured effects of preloading, overloading, and underloading.

Preloading was beneficial when the preload was considerably greater than the subsequent fatigue loads, and when the preload was applied in the same direction as the fatigue loads. When the preload and the fatigue loads had opposite signs, a reduction in fatigue life resulted. These effects were magnified by the periodic application of overloads.

The periodic application of repeated low loads was ineffectual when applied in the same direction as the fatigue loads. When the spectrum included low loads of negative sign, serious reductions in life resulted.

The most valuable finding, perhaps, was that the fatigue behavior of the beam specimens was similar to that of certain full-scale aircraft structures. It was also found that the fatigue properties of the beam specimens were rather insensitive to variations in testing technique and material.

A pneumatic testing machine and an automatic programmer that were developed for this investigation are described.

Differential dielectric apparatus for determining water added to solvents, W. C. Wolfe, *Anal. Chem.* **35,** *1884–1887 (Nov. 1963).*

A simple and rapid technique is described for determining small changes in water concentration in *p*-dioxane or bis (2-ethoxyethyl) ether (diethylene glycol diethyl ether). The moisture content of solids can be determined by extraction, followed by this procedure. Dual matched dielectric measuring cells are filled with liquids to be compared and capacitance differences are measured with a commercial Q-meter. The cells are calibrated with the solvent to be used and solutions containing known concentrations of water in the same solvent. Values for change in dielectric constant with change in water concentration (weight percent), $d\epsilon/dC$, are calculated from experimental data and from literature values. The temperature coefficient of $d\epsilon/dC$ is sufficiently small so that precise temperature control is unnecessary. Calculations of dipole moment from the data support previous observations that water behaves in a non-associated manner in dilute solutions in *p*-dioxane.

Other NBS Publications

Journal of Research 68A (Phys. and Chem.), No. 2 (Mar.–Apr. 1964), 70 cents.

Tritium-labeled compounds X. Isotope effects in the oxidation of aldoses-*l*-*t* with bromine. H. S. Isbell and L. T. Sniegoski.

Thermal degradation of fractionated high and low molecular weight polyisobutylene. D. McIntyre, J. H. O'Mara, and S. Straus.

Ionization constants of the six dichloroanilines and the six dichlorophenols in aqueous solution at 25 °C. R. A. Robinson.

Stereoregularity in ionic polymerization of acenaphthylene. V. M. Story and G. Canty.

Dielectric behavior of the film formed on mica cleaved in moist air. S. Ruthberg and L. Frenkel. (See above abstracts.)

On the measurement of dielectric losses and surface conductivity of dielectrics in parallel plane test capacitors. L. Frenkel. (See above abstracts.)

Polymorphism of bismuth sesquioxide. I. Pure Bi_2O_3. E. M. Levin and R. S. Roth.

Polymorphism of bismuth sesquioxide. II. Effect of oxide additions on the polymorphism of Bi_2O_3. E. M. Levin and R. S. Roth.

Second spectrum of tungsten (W II). Donald D. Laun. (See above abstracts.)

Journal of Research 67B (Math. and Math. Phys.), No. 1 (Jan.–Mar. 1964), 75 cents.

A note on a generalized elliptic integral. G. H. Weiss.

An asymptotic expansion for the multivariate normal distribution and Mill's ratio. H. Ruben.

Calculation of certain multiple generating functions. G. H. Weiss.

Some infinite sums involving zeros of $J_o(x)$. L. F. Epstein.

Optimal matchings and degree-constrained subgraphs. A. J. Goldman. (See above abstracts.)

Effects of a distribution on gap acceptance functions on pedestrian queues. G. H. Weiss.

Gaussian wave functions for polyatomic molecules: integral formulas. M. Krauss. (See above abstracts.)

Radio Sci. J. Res. NBS/USNC–URSI 68D, No. 3 (Mar. 1964), $1.00.

An interpretation of rapid changes in the phase of horizontally polarized VLF waves recorded at night over a short path in the southwestern United States. E. E. Gossard and M. R. Paulson.

Precise phase and amplitude measurements on VLF signals propagated through the Arctic zone. F. H. Reder, C. J. Abom, and G. M. R. Winkler. (See above abstracts.)

On the long term phase stability of the 19.8 kc/s signal transmitted from Hawaii, and received at Boulder, Colorado. A. H. Brady. (See above abstracts.)

Oblique propagation of groundwaves across a coastline. Part III. J. R. Wait.

Impedance of a monopole antenna with a radial-wire ground system on an imperfectly conducting half space. Part III. S. W. Maley and R. J. King.

A simplified theory of diffraction at an interface separating two dielectrics. J. Kane and S. N. Karp. (See above abstracts.)

Variational solution for the admittance of long cylindrical antenna. R. A. Hurd.

Admittance of annular slot antennas radiating into a plasma layer. J. Galejs.

Propagation of plasma waves in a "spoke-wheel" magnetic field. R. L. Liboff.

An experimental investigation of signal strength in the area around a transmitter's antipode. R. M. Pipp and J. B. Webster.

Relationship between simultaneous geomagnetic and ionospheric oscillations. H. Rishbeth and O. K. Garriott.

Radio Sci. J. Res. NBS/USNC–URSI 68D, No. 4 (Apr. 1964), $1.00.

Some basic microwave phase shift equations. R. W. Beatty. (See above abstracts.)

A light-modulated scattering technique for diffraction field measurements. A. M. Vural and D. K. Cheng. (See above abstracts.)

Radiation from an aperture in a coated plane. C. M. Knop and G. I. Cohn.

Impedance of a cylindrical dipole having a sinusoidal current distribution in a homogeneous anisotropic ionosphere. W. S. Ament, J. C. Katzin, M. Katzin, and B. Y.-C Koo.

Propagation of electromagnetic waves through a continuously varying stratified anisotropic medium. G. H. Price. (See above abstracts.)

Lunar semi-diurnal tides in h'F and their influence on transequatorial radio propagation. J. A. Thomas.

Some statistical parameters related to the Nakagami-Rice probability distribution. W. R. Burns.

The U.S. National Committee Report for Commission 6 of URSI. Subcommission 6.3, Electromagnetics.

Radioactivity, Recommendations of the International Commission on Radiological Units and Measurements, NBS Handb. 86 (Nov. 29, 1963) 40 cents. (This publication supersedes parts of H78. Handbooks 84 through 89 extend and largely replace H78.)

Mean electron density variations of the quiet ionosphere No. 12, February 1960, J. W. Wright, L. R. Wescott and D. J. Brown, NBS Tech. Note 40–12 (Dec. 6, 1963), 35 cents.

A comparison of two melting-pressure equations constrained to the triple point using data for eleven gases and three metals, R. D. Goodwin and L. A. Weber, NBS Tech. Note 183 (Oct. 6, 1963), 25 cents.

Lunar occultations of two discrete radio sources in 1963–1964, J. A. Eddy, NBS Tech. Note 184 (Oct. 11, 1963), 20 cents.

Thermodynamic property values for gaseous and liquid carbon monoxide from 70 to 300°K with pressures to 300 atmospheres, J. G. Hust and R. B. Stewart, NBS Tech. Note 202 (Nov. 30, 1963), 60 cents.

Calculations of the field near the apex of a wedge surface, J. R. Wait and C. M. Jackson, NBS Tech. Note 204 (Nov. 21, 1963), 45 cents.

Expanded vinyl fabrics for apparel use, CS258–63 (Sept. 19, 1963), 10 cents.

Large longitudinal retarded elastic deformation of rubberlike network polymers. II. Application of a general formulation of nonlinear response, H. Leaderman, F. L. McCrackin, and O. Nakada, Trans. Soc. Rheology **VII,** 111–123 (1963).

Short-duration visible afterglow in helium, A. L. Schmeltekopf, Jr., and H. P. Broida, J. Chem. Phys. **39,** 1261–1268 (Sept. 1963)

Infrared transmission of the atmosphere to solar radiation, D. M. Gates and W. J. Harrop, Appl. Opt. **2,** 887–898 (Sept. 1963).

Synoptic variations and vertical profiles of large-scale ionospheric irregularities, R. G. Merrill, R. S. Lawrence, and N. J. Roper, J. Geophys. Res. **68,** No. 19, 5453–5459 (Oct. 1, 1963).

Excitation of the red and green coronal lines, C. Pecker and R. N. Thomas, Ann. Astrophys. **25,** No. 2, 100–108 (1962).

Some topics in quantum statistics. The Wigner function and transport theory, H. Mori, I. Oppenheim, and J. Ross, Book, Studies in Statistical Mechanics, ed. DeBoer and Uhlenbeck, I, pt. C, 218–298 (North Holland Publ. Co., Amsterdam, The Netherlands, 1962).

Normal congruence subgroups of the $t \times t$ modular group, M. Newman, Bull. Am. Math. Soc. Res. Announcement 69, No. 5, 719–720 (Sept. 1963).

Thermodynamic study of the thorium phosphide with a mass spectrometer, J. Efimenko and K. A. Gingerich, Proc. Symp. Thermodynamics of Nuclear Materials, Vienna, May 21–25, 1962, pp. 477–486 (International Atomic Energy Agency, Vienna, Austria, Sept. 1962).

Radiation impedance of a source near reflectors, R. V. Waterhouse, J. Acoust. Soc. Am. **35,** No. 8, 1144–1151 (Aug. 1963).

Low energy levels of neutral cerium (Ce I), W. C. Martin, J. Opt. Soc. Am. **53,** No. 9, 1047–1050 (Sept. 1963).

The energy environment in which we live, D. M. Gates, Am. Scientist **51,** No. 3, 327–348 (Sept. 1963).

Evidence for field-aligned ionization irregularities between 400 to 100 km above the earth's surface, T. E. VanZandt, W. Calvert, R. W. Knecht and G. B. Goe, Third Intern. Space Sci. Symp. Proc., Washington, D.C., May 2–8, 1962, pp. 271–273 (John Wiley & Sons Inc., New York, N.Y., 1962).

Studies in the geomagnetic micropulsation frequency range, W. H. Campbell, IEEE Intern. Conv. Record **11,** pt. 9, 25–28 (Mar. 25–28, 1963).

Determination of the electronic energy levels of molecules by low energy electron impact spectroscopy, J. A. Simpson and S. R. Mielczarek, J. Chem. Phys. Letter 39, 1606 (1963).

Gas-phase radiolysis of *n*-butane, R. P. Borkowski and P. J. Ausloos, J. Chem. Phys, **39,** No. 3, 818–824 (Aug. 1, 1963).

Temperature control of the structure and variations of the quiet ionosphere, J. W. Wright, Proc. Intern. Conf. Ionosphere, July 1962, pp. 19–25 (Institute of Physics and the Physical Society, London, England, 1963).

A note on contingency tables involving zero frequencies and the 2I test, H. H. Ku, Technometrics 5, No. 3, 398–400 (Aug. 1963).

Wilmer Souder, pioneer in dental research, G. C. Paffenbarger, N. Y. J. Dentistry **33,** No. 5, 191–192 (May 1963).

Equatorial electron density profiles to 5000 KM, Using the incoherent scatter technique, K. L. Bowles, Third Intern. Space Sci. Symp. Proc. Wash. D.C., May 2–8, 1962, pp. 253–264 (John Wiley & Sons, Inc., New York, N.Y., 1963).

Physical measurements and experiment design, W. J. Youden, Scuola Azione No. 10, 181–200 (Scuola de Studi Sugli Idrocarburi, San Donato Milanese, Italy, 1961–1962).

Strain release in complete dentures, J. B. Woelfel, G. C. Paffenbarger, and W. T. Sweeney, J. Am. Dental Assoc. **67,** No. 2, 321 (Aug. 1963).

Questions of general background and methodology relating to aerodynamic phenomena in stellar atmosphere, J. C. Pecker and R. N. Thomas, Il Nuovo Cimento Suppl. **22,** No. X, pt. I, 1–43 (1961).

Observation on reference electrodes for fused-salt systems, M. A. Reid and J. A. Lloyd, Rev. Sci. Instr. **34,** No. 8, 940–941 (Aug. 1963).

Primary processes in the photolysis of ethyl nitrate, R. E. Rebbert, J. Phys. Chem. **67,** No. 9, 1923–1925 (Sept. 1963).

High-field liquid H_2-cooled aluminum-wound magnet, J. R. Purcell and E. G. Payne, Rev. Sci. Instr, **34,** 893–897 (Aug. 1963).

Complicating factors in the gas phase photolysis of azomethane, R. E. Rebbert and P. J. Ausloos, J. Phys. Chem. **67,** No. 9, 1925–1928 (Sept. 1963).

The formulation of F. D. I. specifications, G. C. Paffenbarger, Intern. Dental J. **13,** No. 1, 133–134 (Mar. 1963).

The *F*-region seasonal anomaly, J. W. Wright, J. Geophys. Res. **68,** No. 14, 4379–4381 (July 15, 1963).

Three-body bound state in He^4, J. M. Blatt, J. N. Lyness, and S. Y. Larsen, Phys. Rev. **131,** No. 5, 2131–2132 (Sept. 1, 1963).

Effect of hydrostatic pressures on the crystallization kinetics of natural rubber, G. M. Martin and L. Mandelkern, J. Appl. Phys. **34,** No. 8, 2312–2317 (Aug. 1963).

The redefinition of the second and the velocity of light, G. E. Hudson and W. Atkinson, Phys. Today **16,** No. 5, 30–32, 34, 36 (May 1963).

The shifts and widths of some stark broadened oxygen lines in an arc plasma, W. L. Wiese and P. W. Murphy, Phys. Rev. **131,** 2108–2115 (Sept. 1, 1963).

Momentum autocorrelation functions and energy transport in harmonic crystals containing isotopic defects, R. J. Rubin, Phys. Rev. **131,** 964 (1963).

The ionization constants of *o*-nitrophenol and 4-nitro-*m*-cresol from 5 to 60°, R. A. Robinson and A. Peiperl, J. Phys, Chem, **67,** 1723 (1963).

The following papers were published in Proc. Mountain States Navy Research and Development Clinic, Raton, N. M., Sept. 28–29, 1961, (Raton, Communications and Electronics Foundation, 1963).

Recent progress in cryogenic engineering, R. B. Scott, pp. D1–D4.

Remarks presented at panel discussion on modulation, J. L. Auterman, pp. A131–A132.

Predicting the performance of tropospheric communication links singly and in tandem, A. P. Barsis, K. A. Norton, and P. L. Rice, pp. A71–A104.

Required signal-to-noise ratios, carrier power, and bandwidth to achieve a given performance for multichannel radio communication systems, E. R. Florman and J. J. Tary, pp. A135–A140.

VLF propagation, W. L. Taylor and A. G. Jean, pp. A45–A66.

Millimeter wave research at the National Bureau of Standards, R. W. Zimmerer, pp. A109–A112.

Some low temperature properties of materials, R. H. Kropschot, pp. D5–D6.

Aspects of radio meteorology, J. D. Horn, pp. C51–C56.

Problems and prospects in electrical properties of materials, J. L. Dalke, pp. D7–D14.

Noise in VLF to HF bands and prediction of communication reliability, W. Q. Crichlow, pp. A67–A70.

Signal-to-noise characteristics of some typical systems and their comparisons, H. Akima, pp. A125–A130.

Cyclotron resonances in slightly ionized gases, F. Fehsenfeld, J. Chem. Phys. **39,** No. 7, 1653–1661 (Oct. 1, 1963).

Shifts and widths of some stark-broadened oxygen lines in an arc plasma, W. L. Wiese and P. W. Murphy, Phys. Rev. **131,** No. 5, 2108–2115 (Sept. 1963).

Studying the lunar tidal variations in the *D* region of the ionosphere by means of very-low-frequency phase observations, A. H. Brady and D. D. Crombie, J. Geophys. Res. **68,** No. 19, 5437–5442 (Oct. 1, 1963).

Natural electromagnetic field fluctuations in the 3.0 to 0.02 cps range, W. H. Campbell, Proc. IEEE **51,** 1337–1342 (Oct. 1963).

Current development in an electronically scanned antenna H. V. Cottony, Proc. Symp. Elecctromagnetic Theory and Antennas, Copenhagen, June 25–30, 1962, pp.1289–1294 (Pergamon Press, Oxford, London, 1963).

Airglow research, F. E. Roach, Trans. Am. Geophys. Union **44,** No. 2, 431–432 (June 1963).

Velocity-depth relationship in microelectrophoresis cell for asphaltenes in nitromethane, J. R. Wright and R. R. Minesinger, J. Colloid Sci. **18,** 802–804 (Oct. 1963).

Some results of a new method for obtaining ionospheric N(h) profiles and their bearing on the structure of the lower *F* region, A. K. Paul and J. W. Wright, J. Geophys. Res **68,** No. 19, 5413–5420 (Oct. 1, 1963).

Mathematics and experimental science, W. J. Youden, Sci. Teacher **30,** No. 5, 23–26 (Sept. 1963).

Hyperfine structure and isotope shifts in the 2537-A line of mercury by a new interferometric method, W. G. Schweitzer Jr., J. Opt. Soc. Am. **53,** No. 9, 1055–1072 (Sept. 1963).

Stable 6300 A auroral arcs in mid-latitudes, F. E. Roach and J. R. Roach, Planet. Space Sci. **11,** 523–545 (1963).

A theory of incoherent scattering of radio waves by a plasma. III. Scattering in a partially ionized gas, J. P. Dougherty and D. T. Farley, Jr., J. Geophys. Res, **68,** 5473–5486 (Oct. 1, 1963).

Normal congruence subgroups of the $t \times t$ modular group M. Newman, Bull. Am. Math. Soc. **69,** No. 5, 719–720, (Sept. 1963).

Growth and evaporation kinetics and surface diffusion of K and Hg crystal whiskers, R. L. Parker, R. L. Anderson, and S. C. Hardy, Applied Phys. Letters **3,** No. 6, 93–95 (Sept. 15, 1963).

Very-low-frequency phase observations of solar flare ionization in the *D* region of the ionosphere, C. J. Chilton, F. K. Steele, and R. B. Norton, J. Geophys. Res. **68,** No. 19, 5421–5435 (Oct. 1, 1963).

Generalized variational prinelples for electromagnetic vibrations; application to the theory of waveguide junctions, D. M. Kerns, Proc. Symp. Electromagnetic Theory and Antennas, Copenhagen, June 25–30, 1962, pp. 253–259 (Pergamon Press, Oxford, London, 1963).

The following papers were published in Advances in Cryogenic Engineering, volume **8** (1963):

Some idealized solutions for choking, two-phase flow of hydrogen, nitrogen, and oxygen, R. V. Smith, Paper J–10, pp. 563–573.

P–ρ–T values for neon from 27° to 300° K for pressures to 200 atm using corresponding states theory, R. D. McCarty, R. B. Stewart, and K. D. Timmerhaus, Paper C–3, pp. 135–145.

An apparatus to determine the solid-vapor equilibria of binary cryogenic systems, M. J. Hiza and R. N. Herring, Paper C–5, pp. 158–161.

A comparison of the low-temperature adsorption of nitrogen and methane from hydrogen gas on three different adsorbents, M. J. Hiza and A. J. Kidnay, Paper C–7, pp. 174–182.

A refrigeration system incorporating a low-capacity, high-speed, gas-bearing-supported expansion turbine, D. B. Mann, H. Sixsmith, W. A. Wilson, and B. W. Birmingham, Paper D–5, pp. 221–227.

Experimental determination of the bulk density of boiling liquid oxygen, R. W. Arnett, D. R. Millhiser, and W. H. Probert, Paper E–4, pp. 256–262.

Thermal conductivity of solid H_2O and D_2O at low temperatures, J. W. Dean and K. D. Timmerhaus, Paper E–5, pp. 263–267.

Linear thermal expansion of elastomers in the range 300° to 76° K, R. F. Robbins, Y. Ohori, and D. H. Weitzel, Paper E–8, pp. 287–299 (1963).

Solid formation in flowing cryogenic fluids, D. B. Chelton, B. W. Birmingham, and J. W. Dean, Paper E–11, pp. 311–314.

Temperature measurements in cryogenic engineering, R. J. Corruccini, Paper F–1, pp. 315–333.

Pressure measurements in cryogenic systems, P. Smelser, Paper F–7, pp. 378–386.

Perlite for cryogenic insulation, R. H. Kropschot and R. W. Burgess, Paper G–7, pp. 425–436.

Force and seal evaluation of elastomeric O-rings, P. R. Ludtke and D. H. Weitzel, Paper H–6, pp. 467–477.

Experimental investigation of liquid-hydrogen cooling by helium gas injection, A. F. Schmidt, Paper J–5, pp. 521–528.

Liquid requirements for the cool-down of cryogenic equipment, R. B. Jacobs, Paper J–6, pp. 529–535.

Cool-down and warm-up of large powder-insulated dewars, F. Kreith, J. W. Dean, and L. Brooks, Paper J–7, pp. 536–543.

Auroral-zone observations of infrasonic pressure waves related to ionospheric disturbances and geomagnetic activity, W. H. Campbell and J. M. Young, J. Geophys. Res. **68,** No. 21, 5909–5916 (Nov. 1, 1963).

Radio star scintillations and spread-*F* echoes, H. J. A. Chivers, J. Atmospheric and Terrest. Phys. **25,** 468–473 (Aug. 1963).

A low-pressure arc source for the emission spectrum of the FeO molecule, R. K. Dhumwad and A. M. Bass, Appl. Opt. **2,** No. 12, 1335 (Dec. 1963).

Dissociative ionization of H^2; a study of angular distributions and energy distributions of resultant fast protons, G. H. Dunn and L. J. Kieffer, Phys. Rev. **132,** No. 5, 2109–2117 (Dec. 1, 1963).

Some derivatives of 2,2′-(phenylimino)diethanol, A. Cohen and R. S. Tipson, J. Med. Chem. **6,** 822–824 (1963).

Effect of hydrogen-hydrogen exchange collisions, P. L. Bender, Phys. Rev. **132,** No. 5, 2154–2158 (Dec. 1, 1963).

First-order phase transition in a gas of long thin rods, R. Zwanzig, J. Chem. Phys. **39,** No. 7, 1714–1721 (Oct. 1, 1963).

The Pythagorean theorem in certain symmetry classes of tensors, M. Marcus and H. Minc, Trans. Am. Math. Soc. **104,** No. 3, 510–515 (Sept. 1962).

Gamma irradiation of polytetrafluoroethylene in chlorine, R. E. Florin and L. A. Wall, SPE Trans. **3,** No. 4, 290–299 (Oct. 1963).

The validity of crystal field theory as applied to rare earth ions: An analysis of the spectrum of praseodymium trichloride, J. C. Eisenstein, Low Symposium on Paramagnetic Resonance I, 253–260 (Academic Press, Inc., New York, N.Y., 1963).

Kinetics of desorption. III. Rb^+, K^+, and Na^+ on rhenium, M. D. Scheer and J. Fine, J. Chem. Phys. **39,** No. 7, 1752–1755 (Oct. 1, 1963).

The reactions of methyl radicals in the solid-, liquid-, and gas-phase photolysis of dimethylmercury, R. E. Rebbert and P. Ausloos, J. Am. Chem. Soc. **85,** No. 20, 3086–3089 (Oct. 20, 1963).

Error bounds for first approximations in turning-point problems, F. W. J. Olver, J. Soc. Indust. Appl. Math. **11,** No. 3, 748–772 (Sept. 1963).

Radiation-induced polymerization at high pressure of *n*-tetradecafluoroheptene-1; 1,1,2-trifluorovinyl phenyl ether; 1,2,3,4,5-pentafluorophenyl 1,1,2-trifluorovinyl ether, D. W. Brown and L. A. Wall, SPE Trans. **3,** No. 4, 300–308 (Oct. 1963).

On the growth of helical dislocations, R. deWit, Trans. Met. Soc. AIME **227,** 1443–1452 (Dec. 1963).

A study of anthracene fluorescence excited by the ruby giant pulse laser, J. L. Hall, D. A. Jennings, and R. M. McClintock, Phys. Rev. Letters **11,** No. 8, 364–366 (Oct. 15, 1963).

**Publications for which a price is indicated are available by purchase from the Superintendent of Documents, Government Printing Office, Washington, D.C., 20402 (foreign postage, one-fourth additional). Reprints from outside journals and the NBS Journal of Research may often be obtained directly from the authors.*

U.S. GOVERNMENT PRINTING OFFICE:1964

UNIVERSITY MICROFILMS INC
EDITORIAL DEPARTMENT
313 NORTH FIRST ST
ANN ARBOR MICH
S.IR-C JUNE

UNITED STATES
GOVERNMENT PRINTING OFFICE
DIVISION OF PUBLIC DOCUMENTS
WASHINGTON, D.C. 20402

OFFICIAL BUSINESS

PENALTY FOR PRIVATE USE TO AVOID PAYMENT OF POSTAGE, $300 (GPO)

JOURNAL OF RESEARCH of the National Bureau of Standards Vol. 68C, No. 2 April–June 1964
C. Engineering and Instrumentation

Contents

	Page
Fringe pattern of an oscillating Fabry-Perot interferometer. K. D. Mielenz.	73
Interferometer for testing extended surfaces such as surface plates and precision ways. J. B. Saunders and John V. McDermott.	83
Ferrimagnetic resonance in polycrystalline ferrite and garnet disks at L-band frequencies. W. E. Case, R. D. Harrington, and L. B. Schmidt.	85
Changes in the influence of atmospheric humidity during fatigue of an aluminum alloy. John A. Bennett.	91
The theory of a stable high-speed externally pressurized gas-lubricated bearing. H. Sixsmith and W. A. Wilson.	101
Infrared spectra of asphalts: some aspects of the changes caused by photooxidation. Paul G. Campbell and James R. Wright.	115
Publications of the National Bureau of Standards.	125

Library of Congress Catalog Card Number: 62–3900

For sale by the Superintendent of Documents, U.S. Government Printing Office, Washington, D.C., 20402. Price 75 cents (single copy). Subscription price: $2.25 a year; 50 cents additional for foreign mailing.
UNITED STATES GOVERNMENT PRINTING OFFICE, WASHINGTON : 1964